DEVELOPMENT OF CLAY-DERIVED HYBRID SOLIDSTATE ELECTROLYTE FOR POTENTIAL USE IN SODIUM-ION BATTERIES

NUR SOFINA BINTI MOHAMAD JOHARI

INSTITUTE FOR ADVANCED STUDIES
UIVERSITI MALAYA
KUALA LUMPUR
2022

DEVELOPMENT OF CLAY-DERIVED HYBRID SOLID-STATE ELECTROLYTE FOR POTENTIAL USE IN SODIUM-ION BATTERIES

NUR SOFINA BINTI MOHAMAD JOHARI

THESIS SUBMITTED IN FULFILMENT OF THE REQUIREMENTS FOR THE DEGREE OF DOCTOR OF PHILOSOPHY

INSTITUTE FOR ADVANCED STUDIES
UNIVERSITI MALAYA
KUALA LUMPUR

2022

UNIVERSITI MALAYA

ORIGINAL LITERARY WORK DECLARATION

Name of Candidate: **NUR SOFINA BINTI MOHAMAD JOHARI**

Matric No: 17198904

Name of Degree: Doctor of Philosophy

Title of ~~Project Paper/Research Report/Dissertation~~/Thesis ("this Work")

DEVELOPMENT OF CLAY-DERIVED HYBRID SOLID-STATE ELECTROLYTE FOR POTENTIAL USE IN SODIUM-ION BATTERIES

Field of Study: Physics (Material Physics)

I do solemnly and sincerely declare that:

(1) I am the sole author/writer of this Work;
(2) This Work is original;
(3) Any use of any work in which copyright exists was done by way of fair dealing and for permitted purposes and any excerpt or extract from, or reference to or reproduction of any copyright work has been disclosed expressly and sufficiently and the title of the Work and its authorship have been acknowledged in this Work;
(4) I do not have any actual knowledge nor do I ought reasonably to know that the making of this work constitutes an infringement of any copyright work;
(5) I hereby assign all and every rights in the copyright to this Work to the University of Malaya ("UM"), who henceforth shall be owner of the copyright in this Work and that any reproduction or use in any form or by any means whatsoever is prohibited without the written consent of UM having been first had and obtained;
(6) I am fully aware that if in the course of making this Work I have infringed any copyright whether intentionally or otherwise, I may be subject to legal action or any other action as may be determined by UM.

Candidate's Signature Date: 16/10/2022

Subscribed and solemnly declared before,

Witness's Signature Date: 16/10/2022

Name:

Designation:

DEVELOPMENT OF CLAY-DERIVED HYBRID SOLID-STATE ELECTROLYTE FOR POTENTIAL USE IN SODIUM-ION BATTERIES

ABSTRACT

All-solid-state sodium-ion battery (SIB) is a very attractive technology in achieving a safe and environmentally responsible energy storage device for large scale applications such as grid storage. However, to date, solid-state electrolytes (SSE) have not met the stringent demands that are required to realize the aspiration. Herein, a hybrid SSE (HybSSE) made of halloysite clay-derived Na_2ZnSiO_4 (Clay-NZS) ceramic and Py_{14}TFSI-NaTFSI ionic liquid (IL) solution has been developed to overcome some of the limitations of pure ceramic electrolytes. Their structural and electrochemical characteristics have been investigated by several testing methods in normal laboratory setup as well as in high-throughput setup. Optimization of sol-gel synthesis allows the Clay-NZS ceramic to become an SSE with ionic conductivity of 5.28×10^{-8} S cm^{-1} at room temperature (RT), where Na_2ZnSiO_4 synthesised from standard Si source is only able to ionically conduct at extremely high temperature i.e., 9.44×10^{-8} S cm^{-1} at 300°C. The IL solution mixture has been optimized at 10 wt% NaTFSI salt dissolved in Py_{14}TFSI where after infusing the IL solution into the ceramic pores of Clay-NZS through slow soaking, Clay-NZS HybSSE has managed to achieve an ionic conductivity of up to 0.16×10^{-3} S cm^{-1} at RT, which is much higher than the ionic conductivity of the IL solution as a standalone electrolyte itself. Moreover, the optimized IL solution mixture also enabled Clay-NZS HybSSE to achieve an ionic transference number of 0.991 and Na+ ion transference number of 0.506. This shows that the electronic contribution in this material is negligible and Na^+ ion is the main ionic species in the conductivity of this HybSSE ion. A total of 22 different dopants (A) were introduced into Clay-NZS at 8 different doping levels (x), using $Na_2Zn_{1-x}Si_{1-x}A_{2x}O4$ stoichiometry. It is found that there is no trend that determines

whether an element will improve or deteriorate this HybSSE. The highest ionic conductivity is achieved by $Na_2Zn_{0.9}Si_{0.9}In_{0.2}O_4$ HybSSE, with ionic conductivity values of 0.453×10^{-3} S cm^{-1} at RT and 2.27×10^{-3} S cm^{-1} at 48°C. The improved ionic conductivities of the compound now make this HybSSE a viable candidate for quasi-solid SIBs. Moreover, further screening of the electronic conductivity has shown that dendrite growth throughout all tested HybSSEs is not expected to be a concern. On the other hand, the electrochemical stability window (ESW) of undoped Clay-NZS HybSSE is determined to be 1.28 – 3.45 V. Meanwhile, $Na_2Zn_{0.9}Si_{0.9}In_{0.2}O_4$ HybSSE showed stability at a bigger window of 4.11 V down to 0.8 V *vs* Na. Widest ESW is shown by $Na_2Zn_{0.9}Si_{0.9}Fe_{0.2}O_4$ HybSSE at a window of 2.14 – 4.79 V. All variations of Clay-NZS HybSSE studied were found to be unstable towards Na metal, due to the ceramic material. Therefore, Na metal is not feasible as an anode for this HybSSE without the use of a suitable buffer. In a nutshell, the results exhibit a significant improvement in this category of electrolyte and should serve as a guide in future research & development required to enable the use of this electrolyte in a full cell of SIB.

Keywords: hybrid solid electrolyte, sodium ion battery, oxide-based ceramic, sol-gel synthesis, high-throughput

PEMBANGUNAN ELEKTROLIT PEPEJAL HIBRID YANG DITERBITKAN DARIPADA TANAH LIAT BAGI KEGUNAAN YANG BERPOTENSI DI DALAM BATERI NATRIUM-ION

ABSTRAK

Bateri natrium-ion (SIB) pepejal merupakan sebuah teknologi yang sangat menarik dalam mencapai penyimpanan tenaga yang selamat dan mesra alam bagi kegunaan berskala besar seperti penstoran janakuasa elektrik. Walau bagaimanapun, sehingga kini, elektrolit pepejal (SSE) masih tidak dapat memenuhi kriteria yang diperlukan bagi merealisasikan harapan ini. Di sini, SSE hibrid (HybSSE) yang diperbuat daripada seramik Na_2ZnSiO_4 yang berasaskan tanah liat halloysite (Clay-NZS) dan larutan cecair ionik Py_{14}TFSI-NaTFSI (IL) telah dibangunkan bagi mengatasi beberapa batasan elektrolit seramik tulen. Ciri-ciri struktur dan elektrokimia bahan ini telah dikaji melalui beberapa kaedah yang dilakukan dalam makmal biasa serta dalam makmal *high-throughput*. Pengoptimuman sintesis secara sol-gel membolehkan seramik Clay-NZS menjadi sebuah SSE dengan kekonduksian ionik sebanyak 5.28×10^{-8} S cm^{-1} pada suhu bilik (RT), di mana Na_2ZnSiO_4 yang disintesis daripada reagen permulaan Si piawai hanya mampu mengalirkan ion pada suhu yang sangat tinggi, iaitu 9.44×10^{-8} S cm^{-1} pada suhu 300°C. Larutan IL telah dioptimumkan pada kepekatan 10 wt% garam NaTFSI yang dilarutkan dalam Py_{14}TFSI, yang mana setelah larutan IL tersebut dimasukkan ke dalam pori seramik Clay-NZS melalui kaedah *slow soaking*, HybSSE yang dihasilkan telah berjaya mencapai kekonduksian ionik sehingga 0.16×10^{-3} S cm^{-1} pada RT, di mana ianya jauh lebih tinggi daripada kekonduksian ionik oleh larutan IL itu sendiri. Larutan IL yang telah dioptimumkan ini telah berjaya menjadikan Clay-NZS HybSSE mencapai angka pemindahan ion sebanyak 0.991, manakala angka pemindahan ion Na^+ sebanyak 0.506. Hal ini menunjukkan bahawa pengaliran elektron dalam bahan ini sangat kecil dan ion

Na^+ merupakan spesies ion utama dalam pengaliran ion HybSSE ini. Sebanyak 22 jenis pendopan (A) telah diperkenalkan pada seramik Clay-NZS pada 8 tahap pendopanan (x) yang berbeza, menggunakan stoikiometri $Na_2Zn_{1-x}Si_{1-x}A_{2x}O_4$. Didapati bahawa tiada trend yang menentukan sama ada sesebuah elemen itu akan menambah baik atau merosotkan HybSSE ini. Kekonduksian ionik tertinggi telah dicapai oleh $Na_2Zn_{0.9}Si_{0.9}In_{0.2}O_4$ HybSSE dengan nilai kekonduksian 0.453×10^{-3} S cm^{-1} pada RT dan 2.27×10^{-3} S cm^{-1} pada suhu 48°C. Kekonduksian ionik yang lebih baik kini telah meletakkan HybSSE ini sebagai calon yang baik bagi SIB separa pepejal. Sementelahan itu, pemeriksaan lanjut kekonduksian elektronik telah menunjukkan bahawa pertumbuhan dendrit ke atas semua HybSSE yang diuji tidak dijangka menjadi kebimbangan. Selain daripada itu, julat kestabilan kimia (ESW) bagi Clay-NZS HybSSE tanpa dopan ialah 1.28 – 3.45 V. Manakala $Na_2Zn_{0.9}Si_{0.9}In_{0.2}O_4$ HybSSE menunjukkan kestabilan pada julat yang lebih besar iaitu 4.11 V ke 0.8 V *vs* Na. ESW terbesar ditunjukkan oleh $Na_2Zn_{0.9}Si_{0.9}Fe_{0.2}O_4$ HybSSE pada julat 2.14 – 4.79 V. Kesemua variasi Clay-NZS HybSSE yang dikaji didapati tidak stabil terhadap logam natrium, berpunca daripada bahan seramik yang digunakan. Oleh itu, logam natrium tidak sesuai dijadikan sebagai anod bersama HybSSE ini tanpa menggunakan penimbal yang sesuai. Tuntasnya, hasil kajian ini menunjukkan penambahbaikan yang sangat memberangsangkan bagi kategori elektrolit ini dan wajar dijadikan panduan bagi kajian akan datang bagi membolehkan penggunaan elektrolit ini dalam sebuah SIB yang lengkap.

Kata kunci: elektrolit pepejal hibrid, bateri natrium-ion, seramik oksida, sintesis sol-gel, pemprosesan tinggi

ACKNOWLEDGEMENTS

Praise be to Allah, the Most Gracious and Most Merciful, for allowing me to embark on this journey at University of Malaya (UM) back in 2019 and showering me with blessings upon blessings until I finally reached this proud moment of my life. As a new mother back then, I took a break from work to spend more time with my family whilst tapping into the vastness of His knowledge by furthering my studies. From then on, He has never failed to provide for my family yet ensuring success in every aspect of my study. My PhD went by so smoothly and excellently, even despite Covid-19, to the point that this whole experience of is nothing short of a miracle. He gave me the greatest learnings in these 3 years, surrounded me with people who continuously improved me for the better, and granted me the luxury of witnessing my eldest child grow in front of my eyes while still able to live life comfortably.

Secondly, I thank my supervisors, Dr. Syed Bahari Ramadzan Syed Adnan and Associate Professor Dr. Noraini Ahmad, for taking me in as their student and became my guiding light from the very beginning. They have showed patience in helping me navigate through the different milestones of my study and reminded me to constantly focus on my goals. From converting my master's to PhD, to sharing with me opportunities to join conferences and competitions, to giving me the liberty to define my PhD work scope despite how ambitious some of them were. Alhamdulillah, with their trust and supervision, I am able to achieve what I have achieved thus far. Special mention to Assistant Professor Dr. Eric McCalla of McGill University, Canada, who accepted me with open arms when I approached him to do a research attachment at his lab under the Canada-ASEAN Scholarships and Educational Exchanges for Development (SEED) program. Eric held my hand from day one and taught me so much about being a good researcher and led by example in being a wonderful Principal Investigator. The amount of knowledge I gathered at the McCalla lab is invaluable, although it was only for 6

months. No amount of thanks is ever enough to show my deepest appreciation and gratitude to these 3 individuals who were pivotal in my PhD journey.

Next, I would like to thank my fellow colleagues in the various laboratories I have been part of, which are the Electrochemical Materials & Devices Lab of UM's Centre for Foundation Studies, the Colloid Chemistry and Nanotechnology Lab of UM's Department of Chemistry, and the McCalla Lab of McGill's Chemistry Department. The continuous exchange of knowledge and information between us were what kept me going throughout my studies, especially when I hit stumbling blocks in my research. Not to forget important individuals from the Centre of Ionics UM, the Solar Energy Research Institute UKM, as well as the Faculty of Applied Sciences UiTM who provided assistance to me in filling in the gaps in my research and data, without which my PhD would be incomplete. My heartfelt appreciation also goes out to all lecturers and staff in the Institute for Advanced Studies (IAS) UM, Faculty of Science UM, Chemistry Department McGill University, as well as the management of UM and McGill for their diligent dedication and support. I am also thoroughly thankful of all the fundings that made my research possible, namely the Fundamental Research Grant Scheme (FP077-2018A) by the Ministry of Higher Education Malaysia, the RU grant – Faculty Programme (RF027B-2018) by University of Malaya, the SEED program by Global Affairs Canada, and also the Discovery Grant by the Natural Sciences and Engineering Research Council of Canada (NSERC). Funding is key in research and development, where it is at the heart of significant advances in science.

Last but never the least, my warmest gratitude and appreciation goes to my family who has been my anchoring pillar in obtaining this doctorate. Much love to my husband, Asyraf Amin, who gave me his fullest support and blessing in every step of the way and patiently persevered through our family's economic instability while I strive to achieve my ambition. May Allah reward you with nothing less than the highest Jannah. To my

sons, Arslan Asyraf, who was the reason that this PhD ever happened, and Armand Asyraf, who was my biggest motivation to finish this PhD timely. To my parents, who gave me a strong foothold by filling in the gaps of my daily grind, without which I can never function properly. To my in-laws, my siblings, my dearest aunt, who showered my small growing family with utmost tenderness and care, making this pursuit more manageable and pleasant.

To all the others who shared personal encounters with me, although unmentioned specifically, thanks for allowing me to have a part in your life, as how you are part of mine.

TABLE OF CONTENTS

LIST OF FIGURES

LIST OF TABLES

LIST OF SYMBOLS AND ABBREVIATIONS

AC	:	alternating current
ASSB	:	all-solid-state battery
C	:	capacitance
χ^2	:	goodness of fit
Clay-NZS	:	halloysite clay-derived Na2ZnSiO4
Combi cell	:	combinatorial cell
CPE	:	constant phase element
CV	:	cyclic voltammetry
DC	:	direct current
ΔE_A	:	activation energy
ΔE_C	:	energy for mobile ion creation
ΔE_H	:	energy for ionic hopping
DI	:	deionised
Δm_1	:	loss of mass
DMC	:	dimethyl carbonate
DSC	:	differential scanning calorimetry
ε	:	permittivity
ε'	:	real permittivity
ε"	:	imaginary permittivity
EDX	:	energy dispersive X-ray analysis
EIS	:	electrochemical impedance spectroscopy
ESW	:	electrochemical stability window
FESEM	:	field-emission scanning electron microscopy
FTIR	:	Fourier transform infrared spectroscopy
GPE	:	gel polymer electrolyte
HNT	:	halloysite nanotube
HybSSE	:	hybrid solid-state electrolyte
IL	:	ionic liquid
ISE	:	inorganic solid electrolyte
Li	:	lithium
LIB	:	lithium-ion batteries
LISICON	:	lithium superionic conductor

LSV	:	linear sweep voltametry
Na	:	sodium
NASICON	:	sodium superionic conductor
NaTFSI	:	sodium bis(trifluoromethylsulfonyl)imide
NTCR	:	negative temperature coefficient of resistance
NZS	:	sodium zinc silicate, Na_2ZnSiO_4
NZSP	:	$Na_3Zr_2Si_2(PO_4)_3$
PEO	:	poly(ethylene oxide)
PVDF	:	poly(vinylidene fluoride)
Py14TFSI	:	1-butyl-1-methylpyrrolidinium bis(trifluoromethylsulfonyl)imide
R	:	resistance
ρ	:	density
R&D	:	research and development
R_g	:	intragrain resistance
R_{gb}	:	grain boundary resistance
RT	:	room temperature
σ	:	ionic conductivity
σ_{AC}	:	frequency-dependent conductivity
σ_{DC}	:	frequency-independent conductivity
SDS	:	safety data sheet
SEI	:	solid electrolyte interphase
σ_g	:	ionic conductivity due to grain
σ_{gb}	:	ionic conductivity due to grain boundaries
Si	:	silicon
SIB	:	sodium-ion batteries
SiNP	:	silica nanoparticles
SPE	:	solid polymer electrolyte
SSE	:	solid-state electrolyte
σ_{tot}	:	total ionic conductivity
Synthetic-NZS	:	Na_2ZnSiO_4 synthesised using standard analytical reagent
T	:	temperature
t_+	:	cationic transference number
TEOS	:	tetraethyl orthosilicate

TGA	:	thermogravimetric analysis
t_{ion}	:	ionic transference number
UDR	:	universal dynamic response
V	:	volume
ω_H	:	hopping frequency
XRD	:	X-ray diffraction
XRF	:	X-ray flueorescence
Z	:	impedance
Z'	:	real impedance
Z''	:	imaginary impedance

LIST OF APPENDICES

CHAPTER 1: INTRODUCTION

1.1 Research Background

Lithium-ion batteries (LIB) is believed to be the triumph of the millennium. It is the accelerator of modern-day technology, the catalyst to our contemporary lifestyle, and one of the earliest enablers of green technology (John B Goodenough & Park, 2013; Nitta et al., 2015). It first came about in the 1970's during the global oil crisis, when the world finally decided to find alternatives to fossil fuels in order to generate power. Due to the intermittent nature of renewable energies, there was an urgent need to store the energy harvested from renewable sources (Dunn et al., 2011), making the demand for batteries to soar. Unfortunately, soon enough they figured that relying on LIBs is not sustainable. Lithium (Li) exists naturally in a salt form that needs to be mined from the Earth's crust and extracted before they can be converted into the form suitable for use in LIB (Meshram et al., 2014; Xiang et al., 2016). Increasing demand for LIB means exhausting the Li resources worldwide, which may bring up the price of the commodity uncontrollably. Since the natural Li salt is only available at certain geographical locations (Grosjean et al., 2012; Kavanagh et al., 2018), mostly countries with geopolitical conflicts, future market volatility of this commodity is also a source of concern.

As global climate crisis heightens, the push for reliable grid storage continues to intensify in the hopes that renewable energy sources can one day be supplied sustainably throughout the world with little to no reliance on fossil fuel (Guerra et al., 2021; Hussain et al., 2020; Olabi et al., 2021; Pal et al., 2020). Sodium-ion batteries (SIBs) are deemed to carry the sustainable spirit, since sodium (Na) is more readily available in seawater when compared to Li, and therefore has the potential to also be cost-effective and accessible to more beneficiaries (Hirsh et al., 2020; Palomares et al., 2012; Sawicki &

Shaw, 2015; Vaalma et al., 2018; L. Wang et al., 2021; Xu et al., 2021; Yabuuchi et al., 2014). Na bears resemblance with Li in its chemical characteristics because they belong to the same group on the periodic table. Their single valence electron allows for the easy release of electron during discharging, which is the basis of why LIB is a high-energy density battery. Even so, despite Na being simply one row down from Li in the periodic table, the works for SIB development proves to be challenging because of their apparent disparate chemical properties. Even for SIB to achieve a performance that is comparable to LIBs is demonstrated to be of no easy feat, with the commercialization of SIB only happening very recently (Onstad, 2021; *Sodium-Ion Battery Market Size, Scope, Forecast to 2029*, 2021), after decades of research. A new approach to SIB is required to increase the battery's performance since its behaviour is not perfectly analogous to LIB.

On the other hand, the demand for all-solid-state batteries (ASSB) continues to rise, driven by the need for improved safety, lifetime, and eco-friendliness of modern batteries. Having witnessed the evolution of batteries since the 1970s, liquid electrolytes are found to be the source of these major setbacks in conventional batteries (Y. Wang et al., 2021; Yang et al., 2021). Even so, solid-state electrolyte (SSE) comes with its own set of advantages and disadvantages. Achieving targets for ASSB thus also proved to be extremely challenging, requiring immense number of R&D hours. This is largely due to the different variables that need to be considered with the diverse types of solid electrolytes. The SSE comes in various forms, such as solid polymer electrolyte (SPE), inorganic solid electrolyte (ISE), and composite electrolyte. SPE is made up of polymer dissolved with cationic salt, ISE can either be ceramic or glass, while composite electrolyte is when the SPE and ISE are mixed to become one system.

Ceramic SSE is a type of ISE that is made up of a polycrystalline that allows for high mobility of ions in its lattice (Hayes, 1978; Siraj, 2012) and has negligible electronic conductivity. Hence, ceramic SSEs are sometimes called a superionic conductor or a fast-

ion conductor in the literature. It is also favoured as an SSE candidate due to its high thermal stability, inert to chemical shock, and wide electrochemical window (Chadwick, 2005; Hayes, 1978; Kudo & Kawamura, 2005). The variation in ceramic SSE is mainly due to the different lattice structures and defects in the lattice systems, allowing for different ionic hopping mechanism. Unfortunately, ceramic SSEs, especially those that are Na-based, suffer from low ionic conductivity and too high of an operable temperature. Ions in a lattice require a minimum activation energy (ΔE_A) for them to be mobilised and hop through ionic sites in the direction of the applied electric field (Ca Dam et al., 1926; Dieterich, 1981; Padma Kumar & Yashonath, 2006; Tuller, 2017). Such ΔE_A is usually overcome with external source of thermal energy that facilitates the ionic conduction.

With Na being more massive than Li, higher thermal activation is needed to mobilise the Na^+ ions, which is typically translated to higher operable temperature. Furthermore, Na^+ ions are also generally slower than Li^+ ion when mobilised through an electric field, leading to lower ionic conductivity. Research is ongoing to enhance the conductivity of Na^+ ion in ceramic SSE, as well as lowering down its operable temperature. The ionic conductivity of a polycrystalline is determined first, by its resistance to move within the grain (R_g) and next, by its resistance to hop through grain boundaries (R_{gb}). It is widely understood that R_{gb} contributes the most in the overall resistance of a polycrystalline compound. R_{gb} can be reduced by eliminating grain boundaries (Ling et al., 2016; Pfeiffer et al., 1999) through grain growth or by the creation of nanoionics (Jalalian-Khakshour et al., 2020; J. Maier, 2005; Joachim Maier, 2009), which involves making the grains as small as possible. It was found that nanostructured ionic materials have an easier ionic diffusion pathway along grain boundaries, allowing for a significantly smaller R_{gb} (Despotuli et al., 2005).

Other approaches used to reduce the resistance in ceramic SSE include cationic doping or elemental substitution (Adnan & Mohamed, 2014; Ortiz-landeros et al., 2012; Schlem et al., 2019a). Doping and substitutions are widely implemented based off the understanding that ionic conduction in crystals happen due to the hopping of cations between the vacant sites or within the interstitials of the lattice framework (Adnan et al., 2016; Kuganathan et al., 2019; T. H. Wan et al., 2018; B. Zhang et al., 2018). Thus, adding on a new element into a ceramic imposes defects into the system, which can generate desirable effects such as creating more cationic vacant sites, increasing the concentration of mobile ions, or widening the bottleneck for faster transport of mobile ions. All of this is expected to reduce the system's R_g, hence increasing the ionic conductivity of the ceramic SSE.

To date, substitutions into ceramic materials have been insufficient to obtain all the necessary properties for SSEs in SIBs. These properties include malleability, stability at both the cathode and anode, and low electronic conductivity to prevent dendrite formation within the electrolyte (Eshetu et al., 2020; Jonderian & McCalla, 2021; Liang et al., 2019; Lou et al., 2021; L. Shen et al., 2021; W. Zhou et al., 2017). Hybrid solid-state electrolyte (HybSSE) are emerging as a promising way to overcome some of the limitations of all-solid ceramic electrolytes yet eliminating the concerns of a liquid electrolyte (de la Torre-Gamarra et al., 2018; Feng et al., 2021; J.-K. Kim et al., 2015; H. Yu et al., 2021). These systems are also sometimes referred to as quasi-solid-state electrolytes (W. Chen et al., 2018; Gomez, 2021; J. Li et al., 2021) or composite electrolytes (Che et al., 2017; Dirican et al., 2019; Fergus, 2010; J.-K. Kim et al., 2015; Y. Wang et al., 2019).

This PhD project attempted to produce and develop an electrolytic material suitable for SIB, matching all the desirable traits of state-of-the-art systems described above. Herein we report the development of the material from ground up and showcase its performance as a candidate for SIB in its entirety.

1.2 Problem Statement

The study of most types of ceramic oxides as an SSE have not garnered much interest of late due to their lack of exciting improvement, especially in the development of SIB. Sodium zinc silicate, Na_2ZnSiO_4 (NZS), is selected for this project because orthosilicates posed themselves as a good ionic conductor a few decades ago as a LISICON-type material but progress has tapered off since (Adnan & Mohamed, 2014; Hu et al., 1977; Treacher et al., 2016). NZS is therefore representative of such understudied compounds in the literature. The latest ionic conductivity study of this compound found in the literature is done by Grins (1982), exhibiting conductivity value of 1.7×10^{-4} S cm^{-1} at 600 K (~326°C) for NZS, after being synthesised through solid-state reaction method and heat-treated twice at a temperature of 1050°C for 24 h each. While it is common for ceramic oxides to be conductive at temperatures upwards of 300°C, Grins' conductivity value is too low for such high temperature setting, especially when compared to other modern materials. This project expands the study on NZS by conducting a thorough empirical study on its structural and electrochemical characteristics, utilising modern methods, as well as attempt to lower down its operable temperature.

Traditionally, ceramic inorganic polycrystalline are synthesized using the conventional solid-state reaction method, much like the case with Grins (1982). However, this method is generally expensive, requiring extremely high temperature and long sintering hours. This synthesis method is laborious and therefore difficult to reproduce in a standard manufacturing process nowadays. This project will alternatively use a modern synthesis method namely sol-gel synthesis, that is known to be capable of yielding a higher homogeneity and a higher purity of sample at a much lower temperature, making it cost-efficient. This method is also known to be able to produce smaller particulates, which encourages better packing of grains and therefore expected to improve ionic

conductivity. This project scrutinises all the steps involved in the method in order to obtain an optimised synthesis route for a highly conducting NZS.

Halloysite clay is used as one of the starting reagents in the synthesis of NZS to replace the standard synthetic Si starting reagent, by way of selective acid-leaching. As of late, there are no empirical studies done on how the natural halloysite clay modifies the structure and ionic conductivity of an SSE but its nanotubular structure has been exploited in many other applications (Kriaa et al., 2014; Lin et al., 2017; Rawtani et al., 2012). It is expected that the same nanotubular structure will result in the creation of silica nanoparticles, which can further encourage the formation of nanocrystalline NZS. Nano-crystallinity is expected to improve the density of a halloysite clay-derived NZS ceramic pellet and therefore enhance its ionic conductivity. Moreover, because of the different minerals contained in clay, it is also expected that the silica extraction from halloysite might still contain traces of impurities which may also promote better ionic conductivity in the clay-derived NZS.

The project attempts to further expand the potential of NZS to be a more competitive electrolyte for SIB by making it a HybSSE. This is achieved by way infusing the NZS ceramic pellet with an ionic liquid (IL). Literature shows that the IL typically used in SIB research involve either the imidazolium or pyrrolidinium cations, paired with a high-charge delocalized anions such as bis(trifluoromethanesulfonyl)imide (TFSI) (Plashnitsa et al., 2010; Rüther et al., 2020; Wu et al., 2016). This project shall use a commonly used IL in the field to be comparable with the literature, namely 1-butyl-1-methylpyrrolidinium bis(trifluoromethylsulfonyl)imide ($Py_{14}TFSI$), mixed with its corresponding Na salt (NaTFSI), to obtain a Na-ion conducting IL solution. On the other hand, there is currently no predefined way of incorporating IL in a ceramic compound, with multiple literatures showcasing various methods resulting in various outcomes (Barpanda et al., 2011; de la Torre-Gamarra et al., 2018; H. W. Kim et al., 2016). Since the project aims to achieve the

highest Na-ion conducting electrolyte, the best method shall be investigated in order to obtain the best Na^+ ion HybSSE with the highest ionic conductivity and electrochemical performance.

Ionic doping and elemental substitutions are synonymous in making an inorganic compound better conducting. Grins (1982) also showed that small deviations from the stoichiometry of Na_2ZnSiO_4 showcased large improvement to the overall conductivity of the ceramic SSE. However, little is understood of what and how exactly ionic doping and elemental substitutions cause the rise or fall of ionic conductivity of an SSE (Kuganathan et al., 2019; Van Gog & Van Huis, 2019; B. Zhang et al., 2018), let alone its impact on a HybSSE. This project will study the different aspects of doping and substitutions of various elements on a halloysite clay-derived NZS, their influence on the structural and ionic conductivity of NZS, as well as their impact to the overall performance of the synthesised HybSSE.

1.3 Objectives of Study

The objectives of this research are:

i. To synthesise Na_2ZnSiO_4 via sol-gel method using natural halloysite clay as one of the starting reagents and investigate its characteristics as a ceramic SSE

   Silica will be extracted from halloysite and will be used as the silicon starting reagent for clay-derived NZS (Clay-NZS). NZS from standard analytical-grade starting reagents (Synthetic-NZS) will also be synthesised for comparison and to act as a control. Both samples will be synthesised via sol-gel method and subjected to structural, chemical, physical, and electrical characterisation to evaluate their performance as a ceramic SSE.

ii. To examine the changes and enhancements on the structure and conductivity of Clay-NZS when decorated with IL to become a HybSSE

$Py_{14}TFSI$ will be infused into Clay-NZS through the best possible method to create a highly-conducting HybSSE. Changes in structure and conductivity of Clay-NZS will be studied and the sample with the best enhancement in ionic conductivity will be selected.

iii. To study the influence of the addition of Na salt of the IL on the structural stability and conductivity of Clay-NZS HybSSE

NaTFSI will be dissolved in $Py_{14}TFSI$ to obtain an IL solution containing Na^+ ion, and then added into the sample pellet of Clay-NZS. The best ratio of composition will be investigated to obtain the best-performing Clay-NZS HybSSE.

iv. To dope Clay-NZS ceramic with aliovalent and isovalent cations to further enhance ionic conductivity of HybSSE

Different elements will be doped into Clay-NZS and the effect of such doping will be studied on the structural properties of the ceramic SSE, as well as the conductivity of the HybSSE.

v. To conduct full electrochemical characterisation on a selected HybSSE to evaluate its practicality to be an electrolyte candidate for SIB

The best system evaluated through rigorous screening testing will be placed into an electrochemical cell for further experiments to evaluate its feasibility to be an electrolyte candidate for SIB.

1.4 Scope of Study

The silica in halloysite clay is extracted by way of acid treatment using a strong acid over a pre-defined period of time, based on the desired outcome outlined in the literature. The silica extraction is determined to be a success when the X-ray diffraction (XRD) and X-ray fluorescence (XRF) results show that the end material consists mainly of silica and show characteristics of a material that is predominantly made up of silica, regardless in the crystallite or amorphous form. The acid-treated material is then employed as-is into the synthesis of Clay-NZS without further purification.

Ceramic SSE of NZS is synthesised via citrate-assisted sol-gel method where all analytical-grade starting reagents are made into a solution before being mixed together. The starting reagents used are in the form of powders that are soluble in either water or ethanol for easy removal of impurities during heat treatments. With the exception of the starting reagent for silicon, where Synthetic-NZS involves the starting reagent tetraethyl orthosilicate in liquid form to be employed as-is into the mixture at stoichiometry. Meanwhile, Clay-NZS uses silica from the acid-treated analytical-grade halloysite clay, which is insoluble in water and forms suspension. Nonetheless, the same route of synthesis is taken, where the silica suspension is assumed to achieve the pre-determined molarity and constantly stirred before being employed for synthesis.

The precursor of Synthetic-NZS is subjected to thermogravimetric analysis and differential scanning calorimetry (TGA-DSC) to determine the relevant temperatures for heat treatments in the standard synthesis of NZS. Henceforth, the results are used to derive parameters suitable for Clay-NZS synthesis, where the crystallisation step is fine-tuned by the results obtained through XRD measurements. Complementary structural study methods include Fourier transform infrared spectroscopy (FTIR), field-emission scanning electron microscopy with energy dispersive X-ray spectroscopy (FESEM-EDX), as well

as density and porosity analysis. The standard synthesis route is first established to obtain a working HybSSE and later adapted into a high-throughput set-up to further optimise the resultant material.

Handling of $Py_{14}TFSI$ and NaTFSI are fully done in a glove box of inert ambient due to their hygroscopic nature. NaTFSI is added into the IL while the IL is being warmed at medium heat to ensure all the salt is fully dissolved to form IL solution. The IL solution is then infused into the ceramic electrolyte either dropwise or soaked to fabricate the HybSSE. Multiple ratios of NZS:IL:salt are investigated to obtain the best-performing Clay-NZS HybSSE. Successful synthesis of materials is screened through Electrochemical impedance spectroscopy (EIS). The EIS measurements are taken at varying temperatures by using two blocking electrodes. Samples are heated at 110°C overnight before the experiment is conducted to ensure moisture level is kept at a minimum. Samples fabricated in the glove box are either measured on the EIS as soon as it is removed from the glove box or are vacuum sealed in the glove box before being brought outside for investigation. Initial screening involved EIS measurements taken across temperatures, ranging from room temperature (RT) to 500°C, at 25°C interval. The samples' operable temperatures are determined by the ability of the instrument to capture the conductivity values. Since IL have a very high conductivity at lower temperatures and decompose at high temperature, TGA was performed to determine the right maximum temperature for the HybSSE. When a decent conductivity at RT has been obtained, optimisation of the samples involved EIS measurements in high-throughput set-up taken at RT and 48°C.

Upon obtaining samples with good ionic conductivity, their electrochemical characteristics are investigated using a potentiostat to conduct various experiments of voltammetry and chronoamperometry. All the measurements are taken at RT, with samples sealed in an inert environment.

1.5 Structure of Thesis

Chapter 1 sets the stage with some background of this research. It then highlights the project's problem statement, objectives, scope, as well as the thesis structure.

Chapter 2 illustrates the landscape of this field in the literature to-date, diving deep into the understanding of the different electrolytic materials in a battery, techniques used in material synthesis, as well as the electrochemical theories relevant to this project. This chapter also comprehensively reviews state-of-the-art materials and experimental techniques as a preamble to how the results of this project compare with the literature. The calculations employed in this project are also explained in this chapter elaborately.

Chapter 3 describes the research methodology of the project. This constitutes the synthesis and fabrication methods utilised in obtaining the electrolytic samples, as well as the characterisation methods used to investigate the performance of the samples at different stages of the project. This chapter also outlines the parameters and disciplines employed in the various experiments and how the theories explained in Chapter 2 are used to analyse the data gathered.

Chapter 4 and the subsequent two chapters showcase the results obtained from the various experiments done throughout the length of this project, accompanied by discussions of the results. First, Chapter 4 is dedicated to results and discussion pertaining the SSE system derived from halloysite clay. Next, Chapter 5 tables the results and discussion of data obtained from the journey of fabricating a HybSSE through IL infusion. Finally, Chapter 6 extends the results and discussion of HybSSE when Clay-NZS undergoes fundamental optimisation and enhancements.

Chapter 7 wraps up the overall findings of the project and conclude the results in the context of its relevance to the field of energy storage.

CHAPTER 2: LITERATURE REVIEW

2.1 All-Solid-State Battery

Electrolyte is one of the three main components in a battery. It is a chemical medium that transports ions between anode and cathode. The ions travel from one electrode to another and undergo redox reaction to convert chemical energy to electrical energy and vice versa, either to power up equipment or as a form of energy storage (W. Hou et al., 2018). Increasing usage of high-powered devices in our modern world has made known that the weakest link of conventional batteries is the liquid electrolyte that they typically use, with news outlets occasionally covering the harms inflicted by batteries in latest gadgets. Safety concerns are mainly centred around its toxicity, risk of leakages, and flammability (W. Chen et al., 2018; Marom et al., 2010; Roth & Orendorff, 2012). Since the development of rechargeable battery is considered one of the biggest catalysts for renewable energy and grid storage, it is pivotal to overcome these challenges in order to allow for the sustainable supply of energy in the world of ever-growing energy demand. This has thus led to the countless efforts in realising an all-solid-state battery (ASSB).

ASSB eliminates the issues with liquid electrolyte entirely by substituting the liquid electrolyte with solid (Abbas et al., 2020; Kotobuki et al., 2013), giving rise to SSEs. SSEs are also advantageous due to their bigger electrochemical window, better suppression of dendrite growth, as well as higher energy density (M. Hou et al., 2020; W. Zhou et al., 2017b; Y. Zhu & Mo, 2020). The discovery of solids that can conduct ions was made as early as 1899 by Nernst (Nernst-Gottingen, 1899), yet commercialising an ASSB is proved to be difficult due to SSE's relatively low ionic conductivity when compared with the conventional liquid electrolyte. The reason behind it is the difference in ionic conduction mechanism between SSE and liquid electrolyte. Ions in liquid electrolyte are loosely interacting with each other and diffuse easily when electric field is

applied. In contrast, ions in solids are tightly bonded in a structure and when electric field is applied, the mobile cations hop from one ionic site in the lattice to another (J. Kang et al., 2015; B. Zhang et al., 2018; Zheng et al., 2018). This hopping mechanism in solids results in slower mobility of ions and thus lower conductivity when compared to liquid electrolyte. Unlike other solids, SSEs have the ability to conduct ions in an electric field due to the low binding energy of the mobile cations to the material's lattice framework, which is typically <0.5 eV (Bachman et al., 2015; Deng et al., 2017; Song et al., 2015). This energy is often called the activation energy, ΔE_A. The lower the ΔE_A, the easier for the ions to move, making them ionically conductive. Several other aspects influencing the magnitude of a solid's ionic conductivity include ion size, crystal structure influencing bottlenecks, presence of defects in the material, and temperature (Martínez-Juárez et al., 1998; Padma Kumar & Yashonath, 2006; K. Yu et al., 2018). Thorough understanding of an SSE's structure enables modifications to be made to improve the SSE's performance to be comparable to liquid electrolyte (Adnan et al., 2016; Chotipanich et al., 2018).

Using SSE instead of liquid as the separator of anode and cathode in an electrochemical cell introduces a whole different set of challenges that was never a concern with liquid electrolyte. Amongst those are the issue of electrode-electrolyte interfacial contact and the formation of solid electrolyte interface (SEI) layer. Solid-solid contact between the electrode and the SSE makes it hard for ions from the electrolyte to enter into the electrode during charging and discharging (Eshetu et al., 2020; Lou et al., 2021). Meanwhile, SEI is a passivation layer that forms when the materials in the SSE and the electrode react with each other upon contact, or while plating and stripping (Eshetu et al., 2020; Ferdousi et al., 2021; Tanwar et al., 2019). Therefore, delivering a highly-conducting SSE is only one step towards realising an ASSB because the overall cell performance can still be limited by the solid-solid interface kinetics. These interfacial issues need to be addressed first before an ASSB can be a reliable form of energy storage.

Consequently, various kinds of SSEs are explored to address the different issues in ASSB, expanding decades' worth of research and development (Takada, 2016). Primarily, these SSEs come in the fundamental form of an SPE or ISE. Material advancements for SSE not only occurred in the field of LIB, but also in SIB concurrently. Interests in finding the holy grail for ASSB and also the realisation of a functioning SIB go hand in hand as the energy storage field evolve in the modern world.

2.2 Sodium-Ion Solid-State Electrolyte (SSE)

SIB was developed as early as in 1970s (J B Goodenough et al., 1976; Mitoff et al., 1972), in parallel with the development of LIB. Alongside, was the development of Na-ion SSE. Unfortunately, when LIB started to become commercialised in 1990s (Yoshino, 2006), the interest in SIB dampened. It was only in the recent decade that the interest has picked up again, due to rising concerns over Li supply (Egbue & Long, 2012; Olivetti et al., 2017; Winslow et al., 2018). Outperforming LIB remains a challenge as intrinsically, as Na^+ ion is larger and heavier than Li^+ ion. Even so, a multitude of Na-ion SSE has been studied, with several achieving conductivity values competitive to its Li counterpart.

To overcome the challenge posed by the intrinsic characteristics of Na^+ ion, engineering a superior Na-ion solid electrolyte involves a focus in having a material that has internal defects as well as a disorderly structure to facilitate the motion of Na^+ ions within the system. Similar to the ones in LIB, the types of SSE that have been studied for SIB include organic SPE (Jin Il Kim et al., 2018; Vignarooban et al., 2016; Y. Wang et al., 2019), amorphous glass ISE (J. A. Bruce et al., 1986; Herczog, 1985; Susman et al., 1983), and ceramic ISE (Anantharamulu et al., 2011; M. Hou et al., 2020; Jalalian-Khakshour et al., 2020). Since this project is to first, design the best Na^+ ion ceramic ISE,

this section expands on this specific type of SSE through the different material categories available in the literature.

2.2.1 Sodium β-Alumina SSE

The first fast-ion conductor in a commercialised Na-ion battery is the Na β-alumina electrolyte, with research starting as early as in 1960s (Xiaochuan Lu et al., 2010; J. C. Wang et al., 1975; Whittingham & Huggins, 1971; Yung-Fang Yu Yao & Kummer, 1967). In the crystal structure, Na^+ ions are complexed in between layers of alumina which allows for rapid transport of Na^+ when electric field is applied along the 2D conduction plane. The compound has two polymorphs, namely the β"-alumina and β-alumina. The β"-alumina polymorph recorded highest conductivity of 2.0 mS cm^{-1} at RT and can achieve an astounding ionic conductivity of 1 S cm^{-1} at 300°C (Butee et al., 2016; Z. Liu et al., 2020; Tel'Nova & Solntsev, 2015), making Na β"-alumina the ultimate benchmark for Na-ion SSE. There is a stark difference between the ionic conductivity of β"-alumina and β-alumina due to the number of Na^+ ions in the conduction plane, as illustrated in **Figure 2.1** (Chi et al., 2017). Therefore, obtaining a phase pure β"-alumina is the goal for a high-performing SSE.

However, fabricating the desired β"-alumina compound is an expensive process, requiring very high sintering temperature (~1600°C). Unlike its polymorph, β"-alumina is susceptible to H_2O and CO_2 attacks from the atmosphere, making it chemically unstable in ambient air (Z. Liu et al., 2020; Y. Wang et al., 2021). It is also difficult to achieve a homogeneous β"-alumina crystal structure in a polycrystalline without the presence of β-alumina and other impurities, which further hampers ionic transport and thus negatively impacting ionic conductivity (Butee et al., 2016; Z. Liu et al., 2020; Tel'Nova & Solntsev, 2015). Such chemical instability hinders the ability for the SSE to sustainably deliver its maximum ionic conductivity.

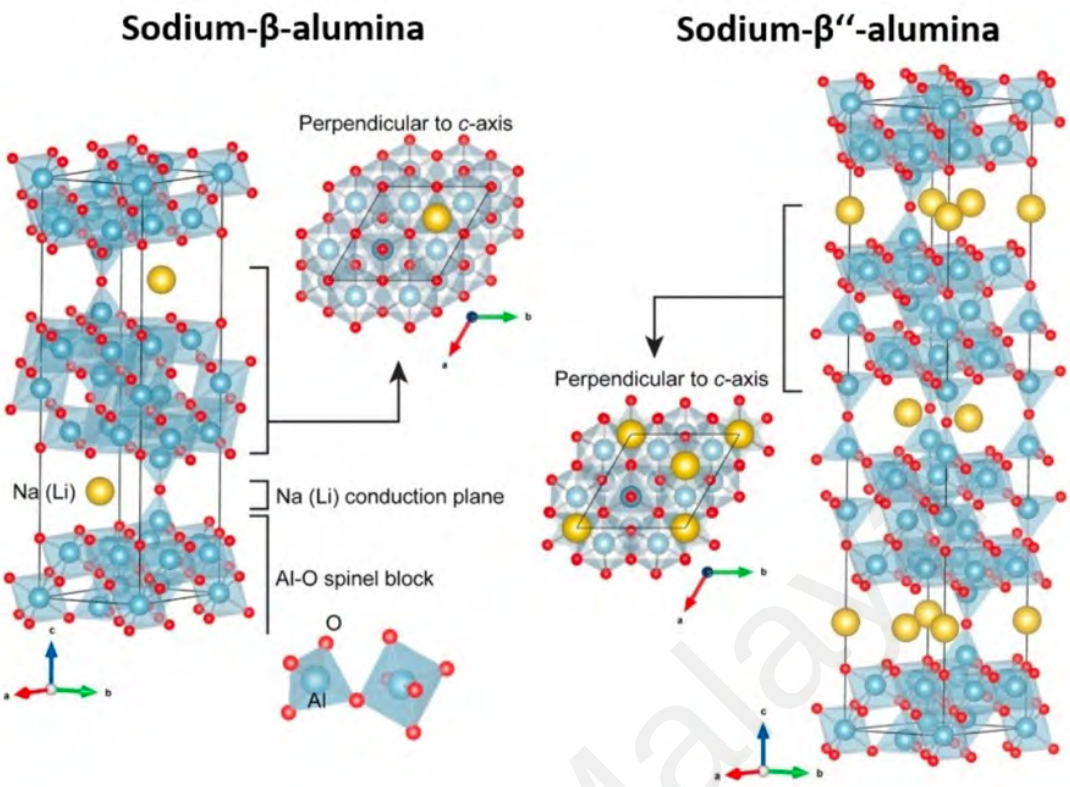

Figure 2.1: Structures of Na β-alumina polymorphs, showcasing the difference in the number of Na^+ ion in the conduction planes. Picture courtesy of (Chi et al., 2017).

2.2.2 Oxide-Based SSE

On the other hand, oxide-based ceramics are typically preferred for electrolytic applications due to its stability in air, wide operating temperature, and relative ease of fabrication (Deng et al., 2017; Etsell & Flengas, 1970; Fergus, 2010). Compared to other SSEs, research efforts in materialising an oxide-based ceramic ISE can focus on enhancing the internal crystal structure favoured for ionic conduction instead of having to overcome external factors that can influence its performance. The main structural aspect that governs the mobility of ions in a ceramic is the crystal framework of the material that determines the bottleneck for ionic diffusion pathway (Bachman et al., 2015; T. H. Wan et al., 2018). Chemically, the Na^+ ion needs to be loosely bonded with other anions while the crystal lattice needs to have a covalently-bonded rigid structure to provide the conduction pathway for the mobile Na^+ ion. It is also known that crystals exist with internal defects, where ionic sites are only partially occupied (Bollmann &

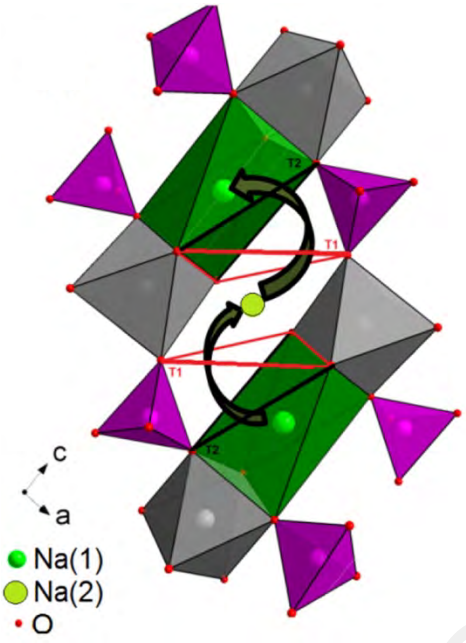

Figure 2.2: A schematic diagram of Na^+ ion hopping from one site in a crystal lattice to another. Picture courtesy of (Naqash et al., 2018).

Bollmann, 1970; Carter & Norton, 2013; T. H. Wan et al., 2018). Theoretically, Na^+ ion hops from one vacant site to another, as shown in **Figure 2.2**, after overcoming the activation energy required to move the conducting ions (Naqash et al., 2018). Therefore, the 3D framework of a crystal, alongside crystal defects, accounts for the bulk ionic conductivity within the crystal lattice (W. Hou et al., 2018; Xia Lu et al., 2017; Y. Yuan et al., 2016).

Amongst the state-of-the-art Na-ion SSEs in the literature is the Na Superionic Conductor (NASICON). The first NASICON-type electrolyte was found by Hong and Goodenough in 1976 using solid solutions of $NaZr_2(PO_4)_3$ and $Na_4Zr_2(SiO_4)_3$ (abbreviated as NZSP) as an SSE candidate for SIB. The original NASICON has a covalent network consisting of ZrO_6 octahedra and PO_4 or SiO_4 tetrahedra that share oxygen vertices. Nowadays, NASICON is a term to describe a crystal structure with general formula of $AM(PO_4)_3$ where the A-site and the M-site can be occupied by a plethora of cations (Anantharamulu et al., 2011; Cao et al., 2014; Xia Lu et al., 2017). Depending on the chemical compositions and stoichiometry, the phase structure of a

NASICON-type ceramic can either be rhombohedral, monoclinic, triclinic, or orthorhombic. The stoichiometry, and therefore phase structure, affects the 3D network of the crystal. This will determine the size of the bottleneck for ionic conduction path, thus ionic conductivity values (Jung-joon Kim et al., 2017). The highest ionic conductivity recorded by a pure NASICON, with stoichiometry $Na_3Zr_2Si_2PO_{12}$, is 0.6 mS cm^{-1} at RT and 0.2 S cm^{-1} at 300°C (Bohnke et al., 1999; Bui et al., 2016; Jalalian-Khakshour et al., 2020; Oh et al., 2019).

Not long after the increased interest in the NASICON-type electrolyte, the Li Superionic Conductor (LISICON) type was found. The LISICON-type came about upon the realisation that the Li-O bond is more covalent than Na-O therefore, for the same oxide crystal structure, Li^+ ion is less mobile than Na^+ ion (Hong, 1978). To curb this issue, a crystal structure is formed by having the oxygen anions bonded in a network of four cations, so the bond with the mobile alkali metal ion is more ionic, hence have lower bond energy, allowing for higher ionic conductivity. In general, LISICON has chemical formula of $Li_{2+2x}Zn_{1-x}GeO_4$, where LISICON-type materials involve cationic substitution in all four ionic sites and Ge can often be interchanged with Si (P. G. Bruce & West, 1983; Mazumdar et al., 1984). The crystal structure of LISICON-type material is related to the compound γ-Li_3PO_4. Similarly, the stoichiometry and chemical composition of the material determines the phase structures of the crystal, affecting the bottleneck size for ionic conduction path, thus ionic conductivity. Song et al. (2015) heavily doped a LISICON-type material to obtain $Li_{0.42}Si_{1.5}P_{1.5}Cl_{0.08}O_{11.92}$ and $Li_{0.42}Ge_{1.5}P_{1.5}Cl_{0.08}O_{11.92}$ ceramic electrolytes with ionic conductivities of 1.03×10^{-5} S cm^{-1} and 3.7×10^{-5} S cm^{-1} at RT, respectively. Unfortunately, LISICON-type materials receive reduced interest nowadays due to the difficulty to further increase its ionic conductivity. While the NASICON-type material can be found in Li-ion SSE, the LISICON-type Na-ion SSE is hardly found in the literature (Grins, 1982).

2.2.3 Sulphide-Based SSE

As the research interest in solid electrolyte grew, scientists figured that moving away from an oxide-based ceramic electrolyte into a sulphide-based would enhance the ionic conductivity tremendously (Hayashi et al., 2019; Schlem et al., 2019; B. Zhang et al., 2019). This is because, an S^{2-} ion is larger than an O^{2-} ion, making the size of bottlenecks for the ionic conduction pathway to be bigger. Moreover, due to the higher polarizability and electronegativity of S^{2-} ion, the cations bonded to S^{2-} ion have lower binding energy when compared to being bonded to O^{2-} ion in the same crystal framework. With lower binding energy, the conducting ion is expected to be more mobile with lower activation energy, thus encouraging a higher ionic conductivity. Even so, a sulphide-based compound is highly unstable in air due to its high sensitivity to humidity (Sahu et al., 2014). The sulphides easily decompose and undergo structural changes when exposed to air (Y. Zhu & Mo, 2020). Therefore, research efforts in the development of sulphide-based SSE are mainly focused in getting the right chemical composition and sealing procedure to stabilise the compound in normal room ambient.

In terms of the type of materials explored in the literature, sulphide-based ceramic electrolytes are largely based off their established oxide counterparts. For example, thio-LISICON is a LISICON-type ceramic, with the O^{2-} ion being substituted with S^{2-} ion (Bonnick et al., 2019; M. Li et al., 2020). Such representation was first introduced by Kanno et al. (2000) and managed to attract large interest. Subsequently, Bron et al. (2013) showed that his thio-LISICON material of $Li_{10}SnP_2S_{12}$ managed to achieve ionic conductivity of 4.0 mS cm^{-1} at RT. For SIB, although similar attempts have been made in creating a thio-NASICON material, the result of the thio- analogue of the oxide-based NASICON have not been as impressive (Schlem et al., 2019). Nevertheless, the highest ionic conductivity value recorded by a sulphide-based Na-ion SSE is 3.0 mS cm^{-1} at RT for the tetragonal compound Na_3SbS_4 (Y. Wang et al., 2021; L. Zhang et al., 2016).

2.3 Hybrid Solid-State Electrolyte (HybSSE)

As discussed in previous section, even amongst ceramic inorganic electrolytes, each of the different types of SSE have their own set of advantages and disadvantages. Since conducting ions in a solid is far more complex than in liquid, there are very limited ways to enhance an SSE when confined to the material's specific category. Hence, in this narrowed view, it is thoroughly impractical to obtain all the necessary properties in ensuring high performance of the electrolyte in SIBs. These properties include, but not limited to, high ionic conductivity, malleability, stability at electrodes, and low electronic conductivity to prevent dendrite formation (Eshetu et al., 2020; Jonderian & McCalla, 2021; Liang et al., 2019; Lou et al., 2021; L. Shen et al., 2021; W. Zhou et al., 2017). Researchers therefore have gone into the path of combining different materials in the pursuit of achieving a superior SSE, thus creating composites and hybrids.

By convention, the term "composite electrolyte" is used in the literature when the electrolytic material is made up of different types of SSEs. This class of material has been developed for many decades and is well-established in this field. Research of composites typically occur within the field of polymers due to its versatility in mixing with other solid materials (W. Hou et al., 2018; Palomares et al., 2012; C. Zhao et al., 2018). Polymer-in-ceramic and ceramic-in-polymer are some of the most common forms of composite electrolytes. Meanwhile, the term "hybrid" in the literature is coined in a more general sense that can encompass a combination of different SSEs or a mixture of SSE with liquid electrolyte. The latter material can be made up of liquid-in-solid, solid-in-liquid, and even quasi-solid (Feng et al., 2021; Gomez, 2021; Liang et al., 2019). Unlike composite electrolytes, the development of hybrid SSEs (HybSSE) is quite recent, in efforts to overcome the setbacks in conventional liquid electrolyte, as well as leveraging on the advantages of SSEs.

Often, the naming conventions of HybSSE in the literature are loosely defined, subjected to the specific research presented in a specific article, and can sometimes be interchangeable as research progresses over the years (Feng et al., 2021; Keller et al., 2018; J. Li et al., 2021). For example, this thesis project that involves infusing an ionic liquid into an ISE may be called a hybrid electrolyte (de la Torre-Gamarra et al., 2018), a quasi-solid electrolyte (Gomez, 2021), or even a composite electrolyte (Barpanda et al., 2011), depending on which scientific group defining it . This inconsistency in HybSSE nomenclature is because of rapid advancements in material technology that allows for the innovative combinations of materials to continue to emerge. Thus, standardisation is yet to be established in this field of materials. Over the years, many scientists have proposed a way to categorise these "hybrids" (Horowitz et al., 2020; Keller et al., 2018) but as of latest literary progress at the time of writing this thesis, there are no standardisation of such categorisation as the field quickly becomes too vast for all types of hybrids to be included.

For the sake of coherence and simplification, this thesis defines all types of material combinations as a HybSSE. As mentioned, the field can be too vast to be discussed in further detail. Therefore, subsequent sub-sections will deliberate some of the common material combinations available in the literature that are most related to this project, i.e. polymer-based HybSSE, polymer-in-ceramic HybSSE, and IL-in-ceramic HybSSE.

2.3.1 Polymer-Based HybSSE

The most common form of HybSSE is the composite polymer electrolyte, where a plethora of additives can be incorporated into polymers like poly(ethylene oxide) (PEO) or poly(vinylidene fluoride) (PVDF) to cater the setbacks of the original SPE and thus enhance their innate mechanical or electrochemical properties. Fundamentally, an SPE is a complex of polymeric chains with alkali metal salts, to which ionic conduction of the alkali metal ions occurs along the polymeric chain (Che et al., 2017; Liang et al., 2019). An SPE has the advantage over other SSEs for being flexible, easy to process, and good electrode-electrolyte contact. On its own, SPE has ionic conductivity of around 10^{-6} S cm^{-1} at RT and transference number of around 0.2 – 0.4 (Horowitz et al., 2020), which is insufficient, making its composite inevitably favoured. Additives that can make an SPE to become a HybSSE include inorganic fillers and organic plasticizers.

Inorganic fillers can either be ceramic or glass and can either be inert or active. An inert filler is an inorganic material that does not contain the conducting alkali metal ions but improves the physical properties of the polymer matrix such as its mechanical strength and thermal stability. Typical inert fillers include SiO_2, Al_2O_3, and TiO_2 (Gebert et al., 2021; J. Liu et al., 2020). These inert fillers act as a solid plasticizer that reduces the crystallinity of the polymer matrix and therefore increases the number of charge carriers in the material. Meanwhile, an active filler means that the inorganic additive material not only improve the physical properties of the polymer matrix, but also contribute alkali metal ions to the original SPE and thus participate in ionic conduction. Na-ion active fillers are usually the commonly known ceramic ISE such as NASICON and sodium sulphides. For both inert and active fillers, the ionic conductivity of the composite electrolyte is usually around 10^{-5} S cm^{-1} at RT (Ran et al., 2021; M. D. Singh & Dalvi, 2019). This value is not very encouraging to replace the conventional liquid electrolyte.

On the other hand, the incorporation of organic plasticizers into an SPE are sometimes better called as gel polymer electrolyte (GPE) in a lot of articles in the literature (Isa et al., 2017; Z. Liu et al., 2021). The term organic plasticizer denotes a highly-conducting liquid additive such as an ionic liquid like $Py_{14}TFSI$, or an ionic solvent like dimethyl carbonate (DMC). The presence of liquid electrolyte in the polymer enhances ionic mobility thus improves ionic conductivity, yet maintains the safety feature attributed to an SPE (M. Zhu et al., 2019). However, adding liquid plasticizer would normally compromise the mechanical strength of the original SPE, hence this type of HybSSE is usually a cocktail of liquid and solid plasticizers being mixed into the polymer to manage all these compromises. With that, it can deliver ionic conduction upwards of 1 mS cm^{-1} (Kuray et al., 2020; Z. Liu et al., 2021), close to that of a liquid electrolyte. Even so, dealing with GPE is complex due to the multifaceted issues within it. To put it simply, too much aqueous liquid electrolyte would compromise safety, too much polymer would compromise energy density, and too much ceramic would compromise ionic conductivity. Striking the right balance is still a work-in-progress in this field.

2.3.2 Polymer-In-Ceramic HybSSE

Ceramic ISE has many advantages over SPE, such as high energy density, low activation energy, and high transference number. Even so, their setbacks include brittleness and poor electrode-electrolyte contact. Meanwhile, an SPE is flexible and can be made to become very thin, despite the poor ionic conductivity and energy density (Horowitz et al., 2020). A polymer-in-ceramic HybSSE is when the concentration of the ionically conducting ceramic in the electrolyte is very high compared to the polymer content. This type of HybSSE aims at leveraging on the high-valued advantages of a ceramic ISE while at the same time harnessing the desirable properties of an SPE. Such composite allows for a jump in ionic conductivity to more than a magnitude from the original SPE (Bonizzoni, 2020).

Having a polymer matrix within a ceramic can be crucial when designing a flexible thin film and an SSE with good interfacial contact. The rigidity and brittleness of a ceramic makes it almost impossible to manufacture a thin film out of a pristine ceramic ISE. Therefore, incorporating a polymer matrix into the SSE binds the ceramic powder together while compromising very little on the performance of the original ceramic ISE (Tang et al., 2021). As such, Cheng et al. (2020) was able to obtain a polymer-in-ceramic HybSSE with ionic conductivity of 2.25 mS cm^{-1} and capacity retention of 85% after 175 cycles, thanks to the mixture of NASICON ceramic and PVDF polymer in their HybSSE.

2.3.3 IL-In-Ceramic HybSSE

It was previously unthinkable to hybridise a ceramic ISE with liquid, until the recent discovery of IL. Unlike the traditional aqueous liquid electrolyte, IL is a molten salt that exists in liquid form at room temperature (Ratti, 2014; Sigma-Aldrich, 2005; Valderrama et al., 2012), hence why some articles in the literature coined the term room temperature ionic liquid (RTIL) (Ohno, 2011; Shin et al., 2005). Due to its pure molten form, it behaves in the very opposite of an aqueous liquid electrolyte. It has no measurable vapour pressure, nor is it flammable. Besides that, it has high chemical, thermal, and electrochemical stability (Bellusci et al., 2020; Benchakar et al., 2020). Most importantly, it has a very high ionic conductivity (Bellusci et al., 2020). Since it can dissolve inorganic salts of the same anion, several studies have been made in finding the best IL for the purpose of LIB and SIB by dissolving Li^+ ion or Na^+ ion in the IL (Appetecchi et al., 2012; Serra Moreno et al., 2014). Amongst thousands of ILs to choose from, the research in SIB field is inclined towards using ILs with mixture of the imidazolium or pyrrolidinium cations with a high-charge delocalized anions such as bis(trifluoromethanesulfonyl)imide (TFSI) (Plashnitsa et al., 2010; Rüther et al., 2020; Wu et al., 2016). Although the results are nothing short of extraordinary, the biggest setback for IL to become a commercial electrolyte on its own is because it is too expensive

for large-scale application. The organic anion in an IL is the main component in providing the fast ionic transport, yet the purification process for the anions is difficult, making it extremely costly to have IL to fully replace the conventional aqueous liquid electrolyte.

Therefore, attempts of incorporating the fast transport characteristic of IL into an SSE have been made. It was found that minimal amount of IL is needed to highly boost the ionic conductivity of any SSE, be it SPE or ceramic ISE (H. W. Kim et al., 2016). Thus, the physical aspect of the SSE remains, despite the addition of IL. Creative ways have been shown in the past decade on how the IL and SSE can be coalesced, especially for ceramic ISE. Barpanda et al. (2011) synthesised the ceramic $LiZnSO_4$ in an IL and obtained a jump in ionic conductivity by ~10^4 S cm^{-1} and a reduction of activation energy by 0.43 eV. Despite the huge success of Barpanda et al., de la Torre-Gamarra et al. (2018) did not manage to improve their NASICON ceramic ionic conductivity when coating the ceramic powder with IL. Therefore, as of now, there are no established way of infusing IL into ceramic that can guarantee the improvement of its conductivity.

2.4 Prospect of Halloysite Clay as an Electrolyte

Clay is a family of minerals that has layered structures of alumina and silica at ratios of either 1:1 or 2:1. Amongst them is the halloysite clay, which belongs to the kaolinite family that has a 1:1 ratio of alumina:silica (Bauluz, 2015). What makes the halloysite unique is because the minerals are layered in rolls of tubes, where the silica form the outer layer and the alumina form the inner layer of the tubular structure (Joussein, 2016; Y. Zhang et al., 2012). Due to the naturally occurring nanotubular structure, halloysite has caught the interest of many scientists to serve a variety of applications. In fact, the number of scientific papers published from the studies and applications of halloysite rose exponentially over the past decade, particularly attributed to its unique structure (Jock Churchman et al., 2016; Rawtani et al., 2012; Y. Zhang et al., 2015).

Direct application of halloysite include replacing carbon nanotubes with halloysite nanotube (HNT) as a more natural alternative for drug delivery (Fu et al., 2017; P. Yuan et al., 2015). Kriaa et al. (2014) studied the electrical properties of clay and results showed that they only have measurable ionic conductivities at very high temperatures (>500°C). Even so, amongst the different types of clays that they studied, it was found that the halloysite clay has an ionic conductivity that is consistently higher by a factor of 1000 compared to the common illite clay at all temperatures, which is as high as 1.0 mS cm^{-1} at 727°C. Kriaa et al. deduced that this is due to the microstructure that is unique to halloysite clay, promoting the mobility of ions along its nanotubes.

Meanwhile, indirect applications of halloysite clay involve some modifications to tap into the potential of its nanosize and large surface area (Q. Chen et al., 2018; Ummartyotin et al., 2016; X. Zhou et al., 2016). The typical modifications is an acid treatment that leaches out the alumina from the inner layer of the HNT and leaves the silica behind, as shown in **Figure 2.3** (Abdullayev et al., 2012; Gaaz et al., 2016; Garcia-Garcia et al., 2017; Saklar & Yorukoglu, 2015). Depending on the strength of acid and the period of treatment, the tubes can either undergo lumen enlargement or disintegrate entirely. Lumen enlargement allows for higher-volume loading whilst disintegration of tubes allows for the harvest of silica nanoparticles (SiNP). X. Zhou et al. (2016) synthesised SiNP from halloysite to obtain a high-performing anode for LIB. Meanwhile, K. Wang et al. (2016) used the SiNP harvested from the acid treatment of halloysite to synthesise a macroporous Li_4SiO_4 carbon dioxide sensor that can absorb more carbon dioxide than the normal Li_4SiO_4. This shows that the yield of SiNP provides a promising output for dielectric materials.

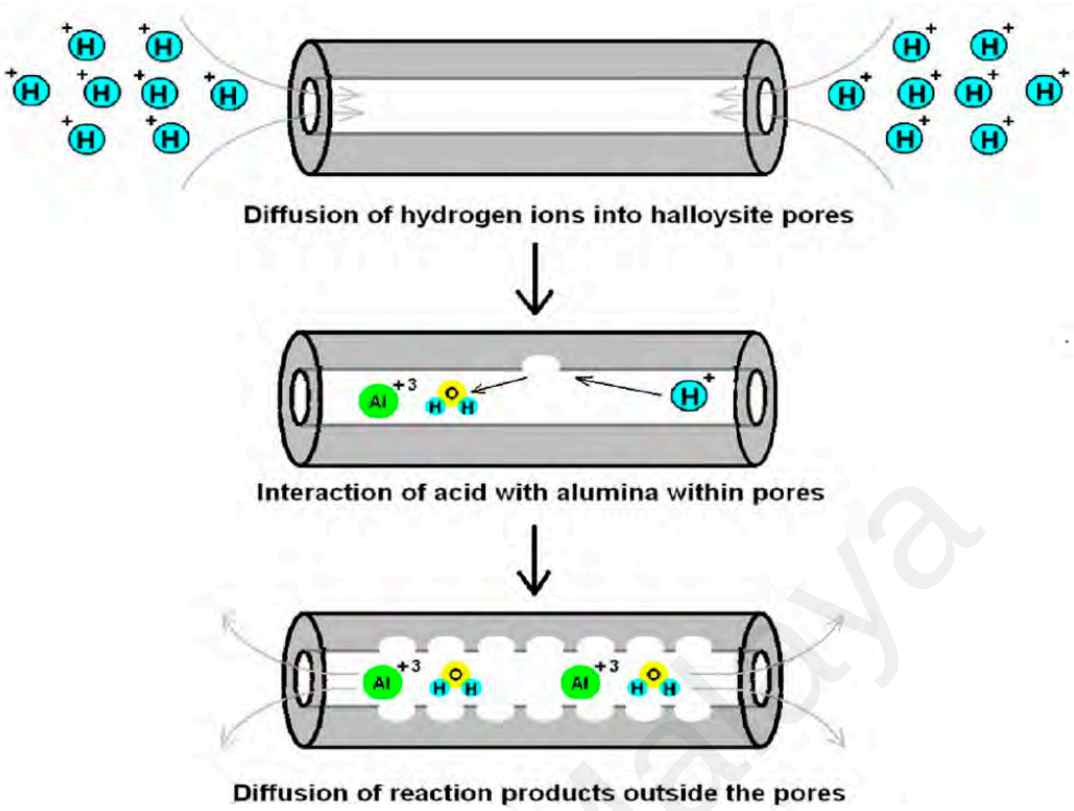

Figure 2.3: Acid leaching of alumina from the inner lumen of HNT. Picture courtesy of (Abdullayev et al., 2012).

Unfortunately, there are limited articles in the literature that shows HNT's application in an electrolyte (Lin et al., 2017; P. Lun et al., 2018; N. Zhao et al., 2016). Some examples include applying the HNT directly as a reinforcing filler in a composite SPE to obtain ionic conductivity of 0.35 mS cm^{-1} at RT (Lazzara et al., 2018; P. Lun et al., 2018). Meanwhile, N. Zhao et al. (2016) mixed HNT with IL to form ionogel electrolyte, achieving ionic conductivity of 3.8 mS cm^{-1} at RT. To-date, no study has been done to see the effect of HNT in ceramic electrolyte, whether applied directly or indirectly. Notwithstanding, it is expected that an HNT-derived SiNP may bring about nanoionics when synthesised to become a ceramic ISE. In nanoionics, resistance due to grain boundaries of the ceramic material is greatly reduced due to the resultant nanosized particulates (Despotuli et al., 2005; Joachim Maier, 2014), leading to a greatly enhanced overall ionic conductivity of the ceramic ISE. (Ahmad, 2015) showed that his nanocrystalline $Li_5La_3Nb_2O_{12}$ (grain size 26 nm) exhibit conductivity value of 3.7×10^{-5}

S cm^{-1} at 27°C, which is an order magnitude higher than its normal crystalline (grain size 1-2 μm) counterpart.

2.5 Synthesis of Ceramic Inorganic Polycrystalline

Ceramics can either be obtained naturally or synthetically. The naturally occurring ceramics are largely silicates, much like clay and minerals. Besides being used in pottery and construction, natural ceramics have very limited applications in technology. Such as the material discussed in Section 2.4, i.e., kaolinite. Even though kaolinite is a big family of clay, only halloysite sees its relevant usage in technological applications. The others, not so much. Meanwhile, ceramic as advanced materials are almost always synthetically made (Bardakhanov et al., 2011; Eliche-Quesada et al., 2019), in order to obtain a high-purity compound. Ceramic synthesis requires the understanding of thermodynamics and mechanics of different elements when put together. As material advancements grew, so do the methods to make synthetic materials. There are various methods used for ceramic synthesis, namely the solid-state reaction method, the co-precipitation method, and the sol-gel method, amongst others. Subsequent sub-sections in this chapter will expand more on the solid-state reaction synthesis, and the sol-gel synthesis used in traditional method as well as in high-throughput setup.

Each of the different synthesis methods has a different reaction route in obtaining the desired ceramic compound. But, the general process for all would be: (1) the starting reagents are thoroughly mixed, (2) precursor is subjected to heat treatments for calcination, (3) powdered sample is moulded into the intended shape, and (4) the green body is crystallised and sintered at high temperature to form a white body ceramic. Since the ceramic synthesis methods discussed in this section produce polycrystalline, the denser the final ceramic obtained in the synthesis, the better (S.-J. L. Kang, 2005). Therefore, there are also a lot of articles in the literature that narrowed down on the effect

of sintering time and temperature in synthesising their ceramic of choice (Huang et al., 2011; Jalalian-Khakshour et al., 2020; Xue et al., 2018). In all methods, reproducibility of process is key to ensure success of the designing and tailoring of advanced ceramic materials (Gonzalo-Juan & Riedel, 2016). However, choice of synthesis method is often due to manufacturing limitations as well as the application of the ceramic material.

2.5.1 Solid-State Reaction Synthesis

The solid-state reaction method of synthesis is considerably the most traditional way of producing an advanced ceramic material whereby the starting reagents, intermediary compounds, as well as the end products are all in solid state. No liquid is involved in any step of the synthesis route. Heterogeneous powders of starting reagents are firstly dry-mixed at stoichiometric ratio for long periods of time to encourage interfacial reactions between the elements. The starting reagents are often oxides or carbonates or any other powder that can undergo thermal decomposition. This is so that the sister elements unwanted in the final phase can easily be combusted during calcination. After the starting reagents are thoroughly mixed to become a solid solution, the precursor powder undergo heat treatments at extreme temperatures, i.e. >1000°C, for an extensive amount of time (Gonzalo-Juan & Riedel, 2016). Packing of the powder to form a green body may occur right after the dry-mixing step or in between heat treatments and calcinations. Ultimately, the green body of the sample undergoes crystallisation and sintered to form a dense white body of the ceramic sample.

This synthesis route was a cutting-edge method in the early days of advanced materials such as ferroelectrics (Kong et al., 2008; Rao & Gopalakrishnan, 1997) because it is simple, yet completely adequate. But, as science progressed and more complex materials were pursued, this synthesis method became undesirable because it does not always behave as expected. Because chemical reactions and diffusion of ions occur solely in solid

state for this synthesis method, it is largely driven by the mass transport of ions at interfaces of particles during the initial dry-mixing step (Ivanov, 2012). Vartanian (2021) akin this method to a black box because it is unclear how exactly the targeted phase is eventually obtained, with a lot of unknown intermediary formations in between. Inhomogeneity of the precursor powder is thus prevalent. Therefore, the handler has little control of the route of reactions besides the mechanochemical aspects, such as making the particles smaller, extensive ball-milling, or continuous grinding of the powders in between calcination steps (Gorrasi & Sorrentino, 2015; Piras et al., 2019). The types of ball mills are shown in **Figure 2.4**. In result, the appearance of secondary phases in the final sample is common and often difficult to manage, making achieving a phase-pure compound unnecessarily complex (Bernardo et al., 2011). Furthermore, the extremely high temperature used in the calcination and sintering steps of this method also result in loss of valuable elements such as lead, bismuth, as well as lithium and sodium (Xue et al., 2018).

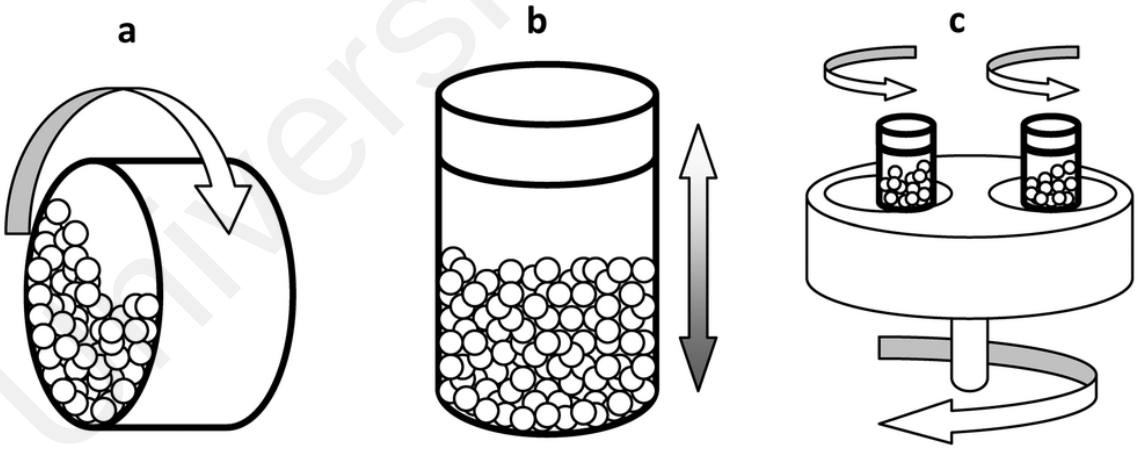

Figure 2.4: Types of ball mill: (a) the tumbler mill, (b) the shaker mill, and (c) the planetary mill. Picture courtesy of (Gorrasi & Sorrentino, 2015).

2.5.2 Sol-Gel Synthesis

Because the solid-state chemistry is not completely understood and poses a lot of issues in the solid-state reaction method, several alternatives have been used to synthesise ceramics in order to have better control of the reactions of the reagents used. Amongst them involves a solution technique, which is the highly regarded sol-gel synthesis method. One of the biggest advantages of the sol-gel synthesis compared to the solid-state method is that ions are mixed at molecular level when in a solution, whereas ions in solid only diffuse in bulk at interfaces. Thus, while homogeneity of sample precursor is a deep challenge in the solid-state reaction method, this is easily obtained in the sol-gel method. Moreover, the sol-gel method of synthesis can achieve better purity of sample at lower temperature because there are a number of parameters that can be controlled throughout the reaction route (Bokov et al., 2021; Esposito, 2019). Thorough understanding of the chemical reactions that occur in the synthesis steps of the sol-gel method removes randomness that often happens in the solid-state reaction method.

Unlike the solid-state reaction method that only deals with powders, the sol-gel method involves the handling of materials in the states of sol, gel, as well as powder. A “sol” is a type of liquid consisting of ions in a molecular colloidal suspension. It is obtained through hydrolysis of precursor powders that are soluble in either water or alcohol such as alkoxides, nitrates, and acetates (Bokov et al., 2021; Brinker & Scherer, 1990; M. M. Li et al., 2021). Meanwhile, a “gel” is a type of solid obtained when the solvent of the colloidal suspension in the sol is evaporated and the solution undergo gelation, eventually leaving polymeric chains in a xerogel. Subsequent steps after forming the “sol” and “gel” are similar to that in the solid-state reaction method in a way that the sample is subjected to heat treatments for calcination and sintering in the form of a powder. The sample powder also undergoes the process of moulding and packing in forming the ceramic sample. The schematic representation of the synthesis process is shown in **Figure 2.5**.

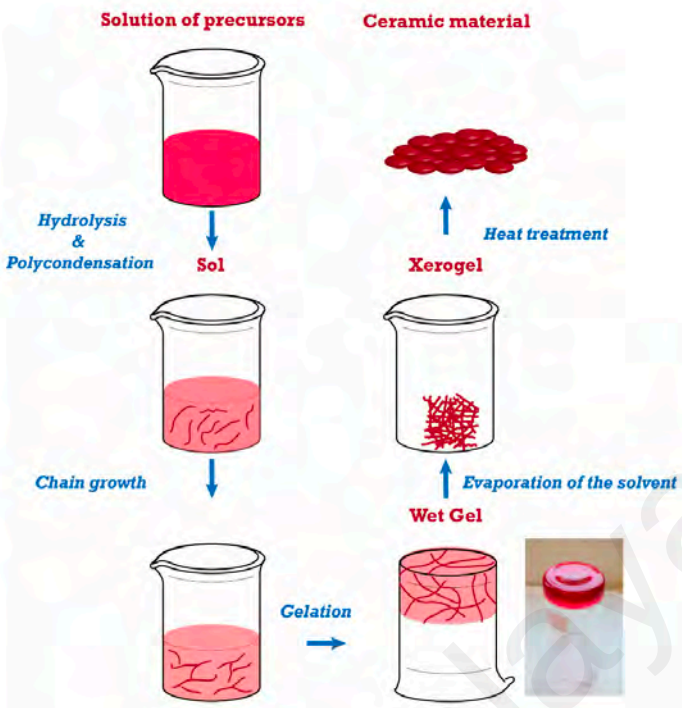

Figure 2.5: A schematic representation of sol-gel synthesis process, from making a sol, to forming a gel, and transforming into powder of ceramic material. Picture courtesy of (Esposito, 2019).

The sol-gel chemistry is largely driven by the process of acid or base catalysis because otherwise the neutral reaction route would be too slow. Therefore, a chelating agent is normally included in the sol (Thiagarajan et al., 2017). Common chelating agents include citric acid as the Lewis acid (Kurajica, 2019) or ethylenediamine (EDA) as the Lewis base (B. G. Kim et al., 2020). These multidentate ligands form complexes with metal cations in the colloid of the sol, isolating the cations to form a homogenous solution. The catalysis also allows for careful fine-tuning of the route of chemical reaction, leaving little margin of error in achieving the right stoichiometric ratio of the targeted phase (Danks et al., 2016). The cationic isolation also warrants for smaller particle size when the polymeric chains are combusted in the latter part of the synthesis. Consequently, the green body of the sample pellet can achieve better packing and the white body of the sample pellet can have better sintering effect, encouraging better grain growth in the polycrystalline.

2.6 High-Throughput Techniques and Combinatorial Methods in Battery Materials

Vast growth in the energy storage field demands for faster development of batteries. While computational works have provided a great insight as to the potential of some material combinations, empirical works still need to be performed to confirm the theoretical simulations. Besides that, computational works like density functional theory (DFT) and molecular dynamics (MD) are still limited to atomistic modelling (Islam & Fisher, 2014; Xia Lu et al., 2017; Z. Yu et al., 2018), whereas external factors also play a role in the synthesis and performance of materials. Often, normal lab work is not fast enough to catch up with the industrial demands that some research groups have developed combinatorial methods and high-throughput techniques to accelerate battery development since the beginning of the millennium (Fleischauer et al., 2005; Yanase et al., 2002). Combinatorial method involves placing samples in a grid that ranges from a six-by-six array to a ten-by-ten array, allowing for a particular experiment to be conducted on a large number of samples in one go. Meanwhile, high-throughput screening is an established technique widely used in the biomedical and pharmaceutical field, often involving the usage of a common 96-well plates. The high-throughput technique is synonymous with the usage of automation, robotics, as well as liquid-handling robots (Mayr & Fuerst, 2008; Tegally et al., 2020). In the same spirit of automation and fast screening, some research groups of the battery field have also developed their own high-throughput infrastructure for material synthesis where the sample output would be fed into combinatorial screening methods (P. Liu et al., 2017).

Because a high-throughput setup requires very small amount of individual samples to work with, adaptations from conventional experiments are not straightforward due to the different chemistries involved in micro and macro systems. Often times, a lot of adjustments from the original procedure are needed so the experiment is not only

validated, but experimental results are also reproducible in a high-throughput setting. The McCalla group at McGill University Canada has developed a suite for high-throughput synthesis and characterisations of battery materials, with methodologies that match the modern techniques to have results comparable to the literature (Jonderian et al., 2022; McCalla et al., 2021). For example, their sol-gel synthesis in high-throughput hastens the gelation step whereas the conventional technique encourages polymeric chain growth by stirring the wet gel before drying into xerogel. Nevertheless, they are still able to produce materials that bear the same characteristics as when they are synthesised traditionally. The flow of their high-throughput procedure is shown in **Figure 2.6**. This project utilised this suite in latter part of the project for enhancements of the material. Detailed explanation of the setup and methodology used are briefed in Chapter 3.

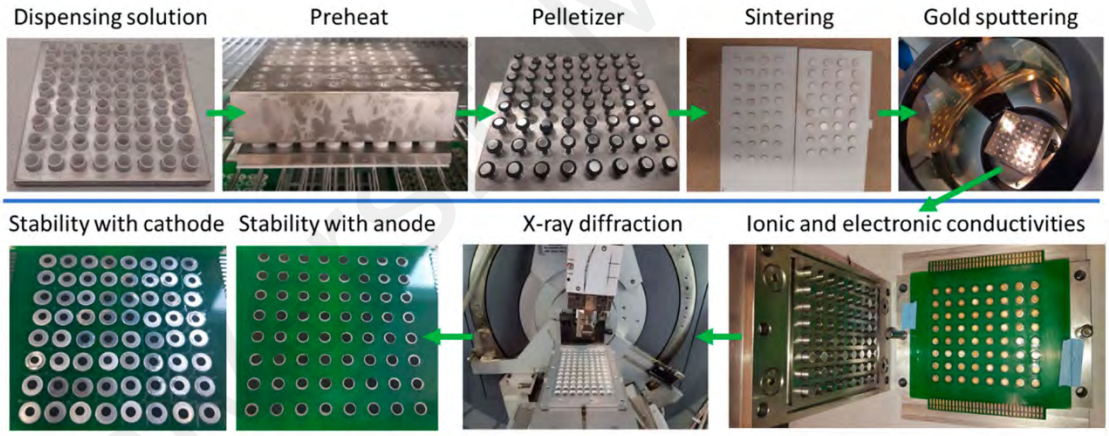

Figure 2.6: A schematic flow of high-throughput procedure in the McCalla lab, where they use a 64-sample eight-by-eight array for material synthesis, as well as structural and electrochemical characterisations. Picture courtesy of (Jonderian, 2022).

2.7 Electrochemical Theories for SSE

2.7.1 Ionic Conduction Mechanism in Solids

Ions in a liquid make for the best ionic conductor because the ions are suspended in a disorderly manner. Paired with their loose bonds, ions in a liquid easily diffuse when an electric field is applied. In solids like ceramics however, ions are mainly bonded covalently with each other and only the alkali metal ions are mobile through ionic hopping when electric field is applied. It is therefore essential for a crystal lattice to have large bottlenecks and internal defects to serve as a diffusion pathway for these mobile metal ions (Padma Kumar & Yashonath, 2006). The large bottlenecks allow for ease of movement of the ions while the internal defects and disorder within a crystalline serve as additional sites for mobile ions to hop across, and thus are the ruling factors that govern ionic mobility and ionic conductivity (Carter & Norton, 2013b).

The diffusion of mobile ions upon application of electric field is described by its resistance (R). Ohm's Law dictates that a material with finite dimensions, when subjected to electric field, will show conductivity (σ) that is inversely proportional to its R:

$$\sigma = \frac{d}{RA} \tag{2.1}$$

where d is the thickness of which the electric field passes through the material and A is the material's area of contact with the electric field source. In ceramics, R may arise from two main sources i.e., the bulk intragrain ionic hopping (R_g) and the grain-boundary intergrain ionic hopping (R_{gb}). Conductivity due to each hopping mechanism can be calculated using **Equation 2.1** to obtain σ_g and σ_{gb}, respectively. Hence, the total conductivity (σ_{tot}) in ceramics can be calculated using **Equation 2.2** below:

$$\frac{1}{\sigma_{tot}} = \frac{1}{\sigma_g} + \frac{1}{\sigma_{gb}} \tag{2.2}$$

Bulk conductivity is often regarded as the true measure of a compound's ability to ionically conduct. The compound's lattice structure and internal crystal point defects give rise to R_g, hence σ_g. Defects in solids are namely the Schottky and Frenkel defects (Adnan et al., 2016; Franklin, 1972; Kuganathan et al., 2019; Van Gog & Van Huis, 2019; T. H. Wan et al., 2018; B. Zhang et al., 2018). Schottky defect is a defect that is due to the vacancy of ionic sites, while Frenkel defect is when there is both vacancy at ionic sites as well as ions occupying at interstitial. Schottky defects commonly occur in a crystal where the anionic and cationic sizes are similar. To maintain the neutrality of the crystal, when one anion vacates a site, one cation follow suit. This means that one Schottky defect leads to the formation of two vacancies, leading to the decrease in density of the solid. Meanwhile, Frenkel defects occur when the cation is significantly smaller than the anions. The cation vacates its own site and then sits at interstitial. Density of solid with induced Frenkel defects remain the same because no atom is lost.

2.7.2 Improving Ionic Conductivity of Ceramic Polycrystalline

A typical method used to improve the ionic conductivity of an ISE is via doping/substitution, in the hopes to reduce the compound's R_g. Elemental doping and ionic substitution expand the crystal lattice and create more defects by encouraging more vacant sites, increasing the conducting cation content, as well as widening the bottleneck for faster ionic transport. Specifically for NASICON, various substitutions done on the original NASICON has led to the increase of ionic conductivity to ~10^{-3} S cm^{-1} at RT (Pal et al., 2020; L. Shen et al., 2021), comparable to state-of-the-art Li-ion oxide-based SSEs. However, research progress for NASICON has plateaued around this figure because a lot of the work done on the compound involve modifications only on its crystal lattice. Whereas, ionic conductivity in ISE is notably also due to other parameters besides R_g (Takada, 2016; Q. Zhang et al., 2021).

Despite R_g being the true resistance of a ceramic material, typically in a polycrystalline, the highest source of resistance is R_{gb} instead of R_g. This is because mobile ions require far greater energy to hop between grains compared to intragrain hopping. In fact, the persistence of high R_{gb} is often the major setback for the advancements of inorganic ceramics as a viable SSE in an actual battery (S. Yu & Siegel, 2017), compared to other types of SSE like polymer and glass. Thereupon, solid-state scientists have tried several methods to reduce the R_{gb}, one of which is by way of crystal growth to eliminate grain boundaries (Carter & Norton, 2013c; Huang et al., 2011). Unfortunately, this effort is unfavourable because encouraging a high sintering effect and thus crystal growth in a polycrystalline often requires sintering the ceramic pellet at extreme temperatures, which can be costly and ineffective for certain materials. Meanwhile, better packing of grains, which is easier to achieve, is also found to reduce R_{gb}, especially when the resultant powders are nanosized. Physically, thermodynamics require a space charge layer of several nanometres to form at grain interfaces. When grains are nanosized, the space charge layer therefore occupies the bulk of the grain, making the interfacial effect to dominate in the overall ionic transport. It is found that at the contact of two nanosized grains, a swift redistribution over both grains' space-charge layers results in huge conductivity enhancement effects, resulting in lower R_{gb} (J. Maier, 2005; Selvamani et al., 2016; H. Wan et al., 2019). This understanding gave rise to the field of nanoionics.

In addition to that, the synthesis of inorganic SSEs often strives towards achieving a phase-pure compound, to the point that enhancements via doping or substitution are usually done very carefully to ensure that the selected ions only enter into the lattice of the primary phase and not create another phase (Ling et al., 2016; J. Lu et al., 2018; Schlem et al., 2019b). What is seldom discussed in the literature is the impact of secondary phases appearing during synthesis. Recently, in the case of Li-La-Ti-O

perovskite materials, it was found that secondary phases present in small quantities can prove to be beneficial, particularly in improving grain boundary conductivities. Jonderian et al. (2021) calls these new secondary phases a "sintering agent". The conductivity might have been improved due to the better packing of the sample or due to the synergy between the different phases in the compound. Taking into account all the variables involved, this project therefore tackles both the R_g and R_{gb} in enhancing the overall performance of the selected compound as an electrolyte.

2.7.3 Ionic Conduction Measurement and Calculation

The concept of resistance can be extended to the alternating current (AC) circuit to become impedance (*Z*). *Z* is a complex value, denoted by the real (*Z'*) and the imaginary (*Z"*) components. The conductivity of an SSE can be probed by applying a sinusoidal electric field at different frequencies to obtain the *Z'* and *Z"* values of the material. When each data point across the frequencies is represented in an Argand diagram, their *Z'* and *Z"* values result in a Nyquist plot with a shape that is characteristic to the type of material tested. In the Nyquist plot, *Z'* and *Z"* represent the resistance and reactance (*C*) of an equivalent electrical circuit, respectively. The characteristic Nyquist plot of a dielectric like ceramics would have two semicircles, signifying the presence of both R_g and R_{gb}, in accordance with the theory discussed in earlier subsections. The semicircle indicates an equivalent *R*|*C* circuit, where the *R* and the *C* components are assembled in parallel. Thus, two semicircles correspond to having a series of two *R*|*C* circuits, as shown in **Figure 2.7**. In a real circuit representation, *C* is usually replaced by the constant phase element, *CPE*. The fitted *R* value from the Nyquist plot is then used to calculate the sample's σ using **Equation 2.1**.

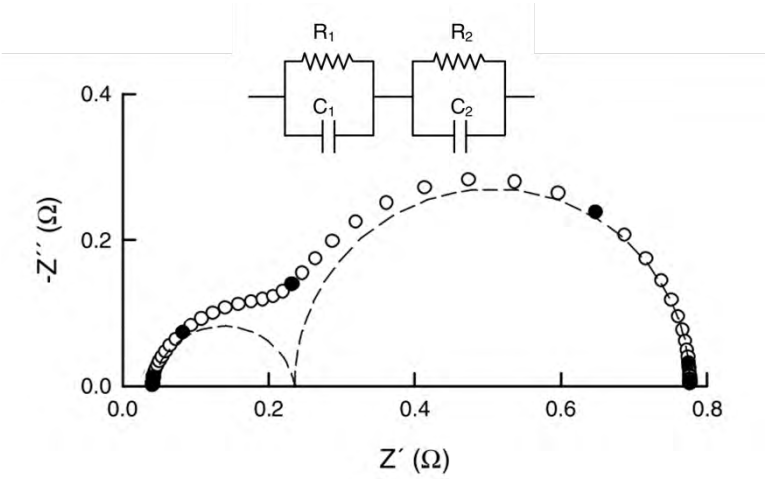

Figure 2.7: A Nyquist plot characteristic to a dielectric ceramic. Inset is the equivalent circuit used to fit the plot.

Ionic hopping in SSE can only happen when the mobile ions obtain the minimum energy required to move, namely the activation energy (ΔE_A). The sample's ΔE_A can be derived from the conductivity values calculated from the Nyquist plot using the Arrhenius relation. Because the Nyquist plot does not explicitly reveal the frequencies used in the impedance measurements, the conductivity value obtained through this method is a frequency-independent conductivity (σ_{DC}). When σ_{DC} values are measured across different temperatures (T), the Arrhenius equation is therefore modified to become **Equation 2.3**:

$$\sigma_{DC} = \sigma_0 e^{\frac{-E_A}{k_B T}} \tag{2.3}$$

where σ_0 is the pre-exponent factor and k_B is the Boltzmann constant. From here, ΔE_A can easily be calculated.

Since ceramic electrolyte is susceptible to polarisation, the dielectric permittivity, (ε) of samples can be calculated from the impedance values. **Equations 2.4** and **2.5** show how the real (ε') and the imaginary (ε") components of ε is calculated respectively:

$$\varepsilon' = C_0 \frac{Z'}{[(Z')^2+(Z")^2]\omega} \tag{2.4}$$

$$\varepsilon" = C_0 \frac{Z"}{[(Z')^2+(Z")^2]\omega} \tag{2.5}$$

where C_0 is vacuum capacitance and ω is angular frequency ($\omega = 2\pi f$). The frequency-dependent conductivity (σ_{AC}) can then be calculated using **Equation 2.6** shown below (Jonscher, 1972) :

$$\sigma_{AC} = \varepsilon''\varepsilon_0\omega \tag{2.6}$$

where ε_0 is the permittivity of free space. **Equation 2.6** can then be extended to **Equation 2.7** to arrive at the Jonscher's Universal Dynamic Response (UDR) (Jonscher, 1972):

$$\sigma_{AC}(\omega) = \sigma_{DC} + A\omega^S \tag{2.7}$$

where A is a pre-exponent constant and S is the exponent that corresponds to the ionic mobility behaviour. Graph of σ_{AC} as a function of ω unravels a number of things that Nyquist plots overlook and hence allow for subsequent derivation of information. Amongst those is the ionic hopping frequency (ω_H). Almond & West (1983) theorised that ω_H is the frequency where $\sigma(\omega) = 2\sigma_{DC}$ because σ_{DC} abides by the Nernst-Einstein relation as shown in **Equation 2.8** below:

$$\sigma_{DC} = en_c\mu \tag{2.8}$$

where e is ionic charge, n_c is charge concentration, and μ is ionic mobility. From the Nernst-Einstein relation, the ionic mobility can also be described by its hopping frequency, ω_H, since $\mu \propto \omega_H$.

Henceforth, a similar Arrhenius relation as per **Equation 2.3** can then be used to find the energy needed specifically for ionic hopping within the lattice and from one site to another (ΔE_H), in accordance to the theory laid out by Almond & West (1983). Typically, in ceramics, $\Delta E_H = \Delta E_A$ but in the case where $\Delta E_H \neq \Delta E_A$, the difference is the energy needed to mobilise ions from their sites (ΔE_C). Therefore, in general, the activation energy is equivalent to the sum of the two, i.e., $\Delta E_A = \Delta E_C + \Delta E_H$.

2.7.4 Ionic Transport and Transference Number

The conductivity of a material is essentially the movement of electrically conducting species across a medium. This conductivity can either be electronic or ionic, i.e., the travelling species is either electrons or ions. Comprehensive study of SSE includes quantifying the number of conducting ions at play in contrast to electrons. An electrolyte in a battery functions as an insulating barrier between the anode and cathode. Hence, a good electrolyte is defined as a material with negligible electronic conductivity, where the only conducting species is ions. This understanding of a material can be investigated through chronoamperometry (Kamat et al., 2010; Mortimer, 2016), where a sample material is subjected to a step DC potential below its decomposition voltage. When a DC potential is applied across an electrolytic material, it experiences mass transport of ions due to polarisation. This mass transport can be visualised by calculating the transference number, which is evaluated through the flow of current across the medium when the DC potential is applied, until it reaches saturation point. Transference number may sometimes be interchangeably called the transport number (Fong et al., 2019; Takada & Ohno, 2016), depending on the context of usage.

A few methods are available to quantify the ions travelling across a medium. Amongst those is the Wagner's DC polarisation method, which is extensively employed in the field of electrolytes to investigate the total ionic transference number (t_{ion}) across an unknown medium (Agrawal, 1999; Wagner & Wagner, 1957). This method is favoured by many due to its simple cell assembly of two blocking electrodes sandwiching the electrolytic material. Upon the DC voltage perturbation, the ions in the electrolyte are polarised and transported across the cell until full dissolution of ions is accomplished at steady state. The current is observed from its initial point (I_i) until it reaches steady state (I_{ss}) and t_{ion} can be calculated using **Equation 2.9** below:

$$t_{ion} = \frac{(I_i - I_{ss})}{I_i} \quad (2.9)$$

If the calculated t_{ion} is close to unity, it can be deduced that the electronic conductivity across the medium is negligible and that it is indeed only ionic species that travel across the medium.

In extension to that, quantifying the amount of Na^+ cation from the total conducting ions is crucial to identify whether the electrolytic material is suitable for SIB. For this purpose, the Bruce-Vincent method can be utilised to determine the cationic transference number (t_+) by way of a non-blocking symmetrical cell (Evans et al., 1987; J. Zhao et al., 2008). In the case of Na^+ ion, the symmetrical cell shall consist of Na metal electrodes. Similarly, a small DC potential (ΔV) is applied across the cell and measurement of current against time will show an initial current value (I_i). Over time, a steady-state of current will be achieved (I_{ss}), denoting the establishment of a concentration gradient. This method relates to t_+ using **Equation 2.10** below:

$$t_+ = \frac{I_+}{I_+ + I_-} = \frac{I_{ss}}{I_i} \quad (2.10)$$

where I_+ is the current carried by the cation across the plane and I_- is the current carried by the anion. Because it is understood that an electrolyte obeys the Nernst-Einstein relation (Gao et al., 2015), the impedance of the SSE is measured before and after the polarisation to eliminate any electrode effect. Henceforth, **Equation 2.10** is altered to become **Equation 2.11** below:

$$t_+ = \frac{I_{ss}\,(\Delta V - I_i R_i)}{I_i(\Delta V - I_{ss} R_{ss})} \quad (2.11)$$

where R_i is the resistance before polarisation and R_{ss} is the resistance after polarisation. A t_+ value of more than 0.5 indicates that the material is a good conductor of the selected cationic species. The conductivity due to the cationic species is therefore the product of t_+ and σ.

2.7.5 Electrochemical Stability Window and Sodium Compatibility

A complete study of a battery component should ultimately include its performance when serving its function in an electrochemical cell. It is therefore pivotal to also consider other parameters essential for an SSE's operationality in a battery besides its individual electrolytic characteristics. Voltammetry techniques are often employed as an extensive testing method to further evaluate a material's performance in a true cell setup. As such, an SSE is known to have a wide electrochemical stability window (ESW). While a Na^+ liquid electrolyte has an ESW of around 2.6 V (Y. Shen et al., 2020), a Na^+ SSE can have stability at upwards of 4.0 V (Meng et al., 2020). A voltametric study on an electrolytic sample probes the voltage points at which the chemical oxidation or reduction in the sample is irreversible and therefore limiting.

The voltametric studies include the linear sweep voltammetry (LSV) and cyclic voltammetry (CV). LSV involves the sweeping of potential linearly across the SSE sample from a low voltage to a predefined upper voltage limit at a regular scan rate (Bontempelli et al., 2016). Meanwhile, CV is an extension of LSV in which the sweeping of potential is cyclical between a predefined lower and upper voltage limit (Elgrishi et al., 2018). The upper limit of a material's ESW can be identified with an overpotential during a positive potential sweep, indicating the oxidation breaking point. Meanwhile, the lower limit is identified with a negative overpotential when the potential sweeping is done negatively, indicating the reduction breaking point. Thus, a material's ESW is defined to be the range of potential at which no redox reaction occurs within the electrolytic material. Often times in the literature, only the upper voltage limit is tested but to truly see its function in a real battery, the lower voltage limit is necessary information too (Eshetu et al., 2020; Rüther et al., 2020).

On the other hand, the voltametric studies can also be employed to identify the compatibility of an electrolytic sample with selected anodic and cathodic materials. When the ESW of the electrolytic sample is determined, cycling the sample within the ESW range will show the reversibility of the material with certain electrodes. Electrodes are typically the ones to cause redox reactions across the voltametric cycles to showcase the intercalation of ions across the electrolyte. Such redox is reversible when it occurs within the electrolyte's ESW. With that, plating and stripping of metal ions can be observed (L. Shen et al., 2021; Tanwar et al., 2019) and the possibility of the formation of solid electrolyte interface (SEI) can also be detected (Chotipanich et al., 2018; Ferdousi et al., 2021). Therefore, the test for electrode compatibility and passivation layer formation are crucial to evaluate an SSE's potential on a use-case basis before putting it into a real battery.

CHAPTER 3: METHODOLOGY

3.1 Overview

The general process flow of the research project is shown in **Figure 3.1**. Briefly, the empirical works of the project are divided into three segments, namely the preparation of samples, structural characterisation, and electrochemical measurements. The structural characterisations are done concurrently with the preparation of samples, ensuring that each step is verified and validated in obtaining the material of interest. The electrochemical measurements serve as a screening method to evaluate the best-performing sample in contrast to one another. Each method within each segment will be further elaborated in **Section 3.3** through to **Section 3.5**.

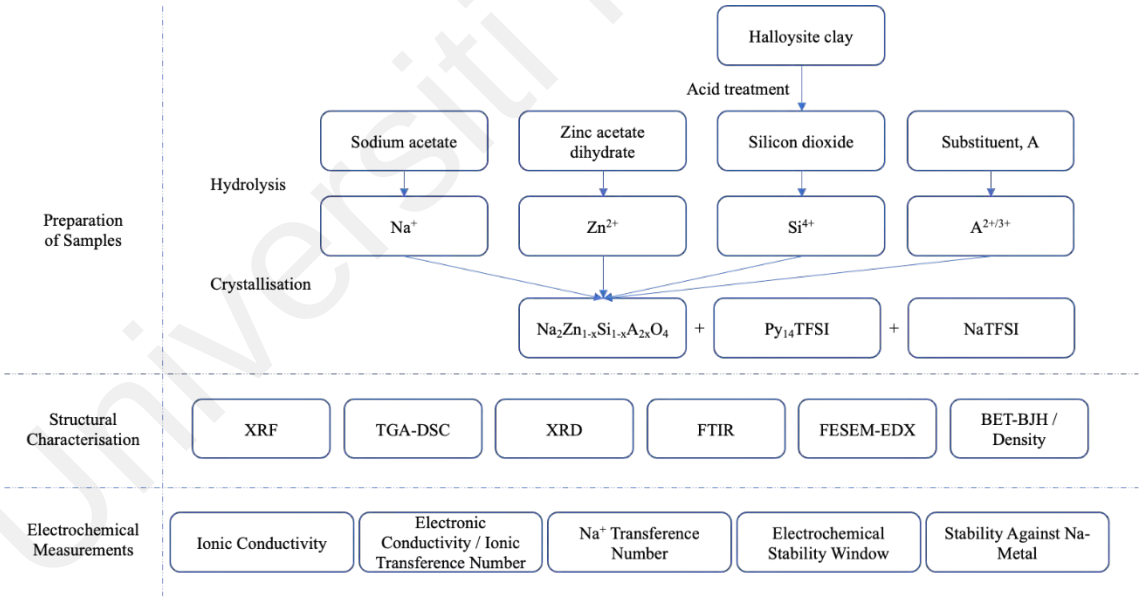

Figure 3.1: Flow chart of research project, outlining sample preparation, structural characterisation, and electrochemical measurements.

3.2 Materials

The chemicals and materials used throughout the project are listed in **Table 3.1** below. All the reagents were of analytical grade and used without further purification.

Table 3.1: List of chemicals and materials used in the project.

Name of chemical/material	Formula	Supplier
Halloysite nanoclay (HNT)	$Al_2Si_2O_5(OH)_4 \cdot 2H_2O$	Sigma-Aldrich
Sulphuric acid	H_2SO_4	Sigma-Aldrich
Sodium acetate	CH_3COONa	Sigma-Aldrich
Zinc acetate dihydrate	$(CH_3COO)_2Zn \cdot 2H_2O$	Acros Organics
Tetraethyl orthosilicate [TEOS]	$(CH_3CH_2O)_4Si$	Sigma-Aldrich
Citric acid	$C_3H_5O(COOH)_3$	Sigma-Aldrich
1-butyl-1-methylpyrrolidinium bis(trifluoromethylsulfonyl)imide [Py_{14}TFSI]	$C_{11}H_{20}F_6N_2O_4S_2$	Sigma-Aldrich
Sodium bis(trifluoromethylsulfonyl)imide [NaTFSI]	$C_2HF_6NNaO_4S_2$	Alfa Aesar
Magnesium nitrate hexahydrate	$Mg(NO_3)_2 \cdot 6H_2O$	Sigma-Aldrich
Aluminium nitrate nonahydrate	$Al(NO_3)_3 \cdot 9H_2O$	Thermo Fisher Scientific
Calcium nitrate tetrahydrate	$Ca(NO_3)_2 \cdot 4H_2O$	Sigma-Aldrich
Scandium nitrate hydrate	$Sc(NO_3)_3 \cdot H_2O$	Thermo Fisher Scientific
Titanium(IV) butoxide	$Ti(OCH_2CH_2CH_2CH_3)_4$	Sigma-Aldrich
Vanadium(III) trichloride	VCl_3	Sigma-Aldrich
Chromium(III) nitrate nonahydrate	$Cr(NO_3)_3 \cdot 9H_2O$	Sigma-Aldrich
Manganese(II) nitrate hydrate	$Mn(NO_3)_2 \cdot H_2O$	Sigma-Aldrich
Iron(III) nitrate nonahydrate	$Fe(NO_3)_3 \cdot 9H_2O$	Sigma-Aldrich
Cobalt(II) nitrate hexahydrate	$Co(NO_3)_2 \cdot 6H_2O$	Sigma-Aldrich
Nickel(II) nitrate hexahydrate	$Ni(NO_3)_2 \cdot 6H_2O$	Sigma-Aldrich

Table 3.1 continued: List of chemicals and materials used in the project.

Name of chemical/material	Formula	Supplier
Copper(II) nitrate hemi(pentahydrate)	$Cu(NO_3)_2 \cdot 2.5H_2O$	Sigma-Aldrich
Gallium nitrate hydrate	$Ga(NO_3)_3 \cdot H_2O$	Thermo Fisher Scientific
Strontium nitrate	$Sr(NO_3)_2$	Thermo Fisher Scientific
Yttrium(III) nitrate hexahydrate	$Y(NO_3)_3 \cdot 6H_2O$	Sigma-Aldrich
Zirconium dinitrate oxide hydrate	$ZrO(NO_3)_2 \cdot H_2O$	Thermo Fisher Scientific
Niobium(V) oxide	Nb_2O_5	Sigma-Aldrich
Ammonium molybdate (para)tetrahydrate	$(NH_4)_6Mo_7O_{24} \cdot 4H_2O$	Thermo Fisher Scientific
Rhodium(III) nitrate hydrate	$Rh(NO_3)_3 \cdot H_2O$	Sigma-Aldrich
Silver nitrate	$AgNO_3$	Thermo Fisher Scientific
Cadmium nitrate tetrahydrate	$Cd(NO_3)_2 \cdot 4H_2O$	Sigma-Aldrich
Indium nitrate hydrate	$In(NO_3)_3 \cdot H_2O$	Thermo Fisher Scientific
Dimethyl carbonate [DMC]	$(CH_3O)_2CO$	Sigma-Aldrich
Carbon black	C	Thermo Fisher Scientific
N-methyl-2-pyrrolidone [NMP]	C_5H_9NO	Sigma-Aldrich
Polyvinyl fluoride [PVDF]	$(C_2H_3F)_n$	Sigma-Aldrich
Sodium metal	Na	Sigma-Aldrich
Sodium manganese oxide [NMO]	$Na_{0.7}MnO_{2+x}$	NEI Corporation

3.3 Preparation of Samples

The main objective of this project is to synthesise a high-performing HybSSE made of halloysite clay-derived NZS ceramic infused with Py_{14}TFSI:NaTFSI IL solution. The fabrication stages of this project include synthesising and fabricating these systems in phases:

System 1. Pristine ceramic SSE of NZS derived from different Si source, namely TEOS (Synthetic-NZS) and HNT (Clay-NZS)

System 2. HybSSE of Clay-NZS through the infusion of IL solution into the ceramic SSE

System 3. Enhanced Clay-NZS HybSSE through structural modifications and elemental doping

Preliminarily, HNT undergo acid treatment to yield SiNP as one of the starting reagents for Clay-NZS synthesis. Then, pristine NZS ceramic was synthesised from the different starting reagents (TEOS vs SiNP) through citrate-assisted sol-gel method to create samples of System 1. Next, Clay-NZS synthesised through optimised procedures from System 1 was infused with IL solution of Py_{14}TFSI and NaTFSI to create samples of System 2. Finally, Clay-NZS HybSSE obtained from the optimum composition of IL solution determined in System 2 underwent further structural modifications and elemental doping to achieve the ultimate high-performing Clay-NZS HybSSE of System 3.

3.3.1 Acid Leaching of Halloysite Nanotube (HNT) to become Silica Nanoparticle (SiNP)

Sulphuric acid (H_2SO_4) was used to selectively etch alumina (Al_2O_3) in the inner lumen of the HNT to yield SiNP. 250 ml of 5 M H_2SO_4 was poured into a flask containing 10 g of HNT and stirred continuously with a magnetic stirrer for 21 h on a hotplate at 70°C under reflux. The white suspension was then filtered and washed several times using deionised (DI) water until the pH level is increased to neutral. The washed residue of white wet slurry was dried in an oven at 150°C for at least 48 h or until bone dry to retrieve a fine white powder of SiNP, which will be used as one of the starting reagents for the synthesis of Clay-NZS.

3.3.2 Citrate-Assisted Sol-Gel Synthesis of Na_2ZnSiO_4 (NZS)

The sol-gel synthesis method is divided into two parts, namely wet chemistry and heat treatments, as shown in **Figure 3.2**. In the wet chemistry part, the starting reagents include the acetates of sodium and zinc, dissolved in DI water, to initiate hydrolysis reactions as per **Equations 3.1** and **3.2** below:

$$(CH_3COO)Na\ (s) + H_2O\ (aq) \rightleftharpoons CH_3COOH\ (aq) + NaOH(aq) \quad (3.1)$$

$$(CH_3COO)_2Zn.H_2O\ (s) + H_2O(aq) \rightleftharpoons 2CH_3COOH(aq) + Zn(OH)_2(aq) \quad (3.2)$$

For Si starting reagent, it is either TEOS for Synthetic-NZS or SiNP for Clay-NZS. **Equation 3.3** represent the hydrolysis of TEOS:

$$(CH_3CH_2O)_4Si\ (aq) + 2H_2O\ (aq) \rightleftharpoons 4CH_3CH_2OH\ (aq) + SiO_2(s) \quad (3.3)$$

Meanwhile, SiNP readily exist as insoluble SiO_2 and were therefore dispersed in DI water using an ultrasonicator to ensure even dispersion, and later continuously stirred on a hotplate using a magnetic stirrer before being used in the synthesis of Clay-NZS. The SiNP suspension was assumed to have the same molar mass as SiO_2.

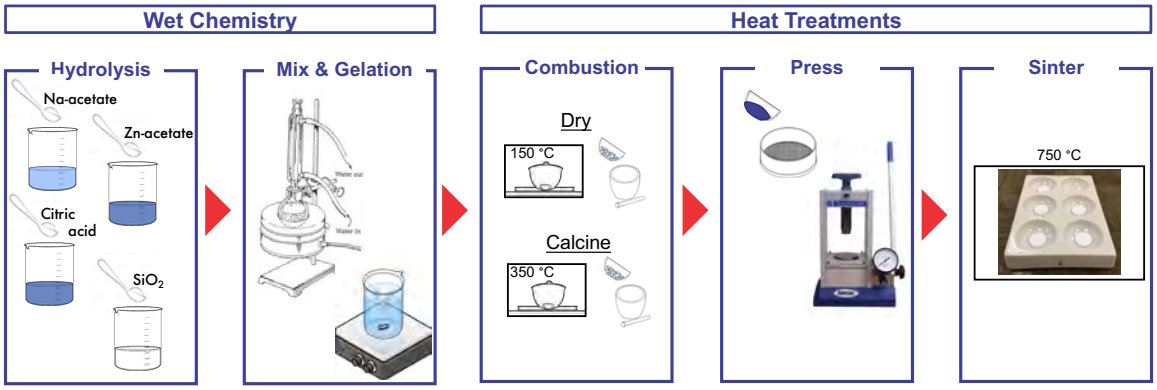

Figure 3.2: Process flow for citrate-assisted sol-gel synthesis employed in the project.

As the name of the method goes, citric acid was included in the reaction to act as chelating agent for the cations with molar ratio of 1:3 for Citrate:Metal due to each citrate ion having three carboxyl functional groups that can form ligands with metal cations. To achieve the stoichiometry of Na_2ZnSiO_4, the hydrolysed reagents were mixed together to obtain a sol of desired ions with molar ratio of 2:1:1:1 for Na:Zn:Si:Cit. The citric acid dissociates upon contact with water and when mixed with cations of Na^+ and Zn^{2+}, form complex ligands as in **Equations 3.4** and **3.5** below:

$$C_3H_5(COO)_3^{-3}(aq) + Na^+(aq) \rightleftharpoons [C_3H_5(COO)_3Na]^{-2}\ (aq) \qquad (3.4)$$

$$C_3H_5(COO)_3^{-3}(aq) + Zn^{2+}(aq) \rightleftharpoons [C_3H_5(COO)_3Zn]^{-1}\ (aq) \qquad (3.5)$$

The sol was stirred continuously with a magnetic stirrer for 24 h on a hot plate at 70°C under reflux to ensure homogeneity of the solution. The resulting white colloidal solution was then vapourised on a hot plate magnetic stirrer at 70°C to produce a wet gel, and later left to age at RT to further strengthen its colloidal network and form xerogel.

The wet chemistry stage is then followed by the heat treatments, where the gel was first dried in an oven at 150°C for 24 h to remove its water content and form a dry precursor powder. Further heat treatments on the sample include calcination in a box furnace at 350°C (2°C step/min, 6 h) to combust the organic compounds involved in the wet chemistry part, namely acetate and citrate. Before the sample reaches crystallisation

stage, the sample powder is cooled to RT, ground, sieved using a 90 μm aperture sieve to produce discreet particles, and later dry-pressed in a hydraulic uniaxial press at 2 tonnes for 30 s to produce pellets of 13 mm diameter. Lastly, the green body pellets were sintered at temperatures 700, 750, and 800°C (2°C step/min, 6 h) to produce a white body monolithic NZS ceramic. The final heat treatment in air causes crystallisation to occur as in **Equation 3.6** below:

$$2Na^{+}(s) + Zn^{2+}(s) + SiO_2(s) + O_2(g) \rightarrow Na_2ZnSiO_4(s) \quad (3.6)$$

3.3.3 Infusion of Ionic Liquid (IL) Solution into Ceramic

Due to the hygroscopic nature of NaTFSI and Py_{14}TFSI, the handling of IL solution and the infusion process into sintered NZS pellet were entirely done in an Argan-filled glove box from Mbraun UNIlab pro under inert ambient of O_2 <1 ppm and H_2O <1 ppm. Py_{14}TFSI was first heated on a hotplate and the NaTFSI salt was added into the IL at concentrations 0, 10, 20, and 30 wt% until fully dissolved to become the desired IL solution. Each IL solution is continuously heated to reduce their viscosity prior to infusion into the ceramic pellet.

There were two methods of infusion used where first, a dropper is used to permeate the IL solution into the pores of sintered pellet of Clay-NZS which were then left overnight to fully soak. The second method used is that the pellets were fully immersed in the IL solution for 10 s to ensure full penetration of IL solution into the pores of the ceramic pellet before being left to rest overnight on a hotplate to fully soak. Both methods established consistent results with one another. The weight of pellets before, during, and after soaking were recorded to determine the amount of IL solution infused into the pellet.

Pellets infused with IL solutions were sealed in sample holders before being brought out of the glove box for subsequent experimental procedure. For normal single-cell experiments, samples are assembled in either a battery jig or a Swagelok-type cell, sealed using Teflon tape and parafilm. For screening in high-throughput, the pellets were placed in an eight-by-eight combinatorial electrochemical cell (combi cell) (Jonderian et al., 2021; McCalla et al., 2021), where they were sandwiched between custom-made printed circuit board by Optima Tech and spring-loaded stainless-steel custom-built pistons. The combi cell was assembled in the glove box and sealed using an o-ring coated with vacuum grease before being brought out of the glove box.

3.3.4 Modified Sol-Gel Synthesis in High-Throughput

In the later phase of the project, the established synthesis method of NZS as per **Section 3.3.2** was adapted into the high-throughput system at McCalla lab to allow for further optimisation of the Clay-NZS HybSSE through structural modification and ionic doping. This is because the high-throughput system (Jonderian et al., 2022; McCalla et al., 2021) allows for a total of 64 samples to be synthesised and investigated in one go. The sol-gel synthesis method that was modified to suit the high-throughput setting is visualised in **Figure 3.3**.

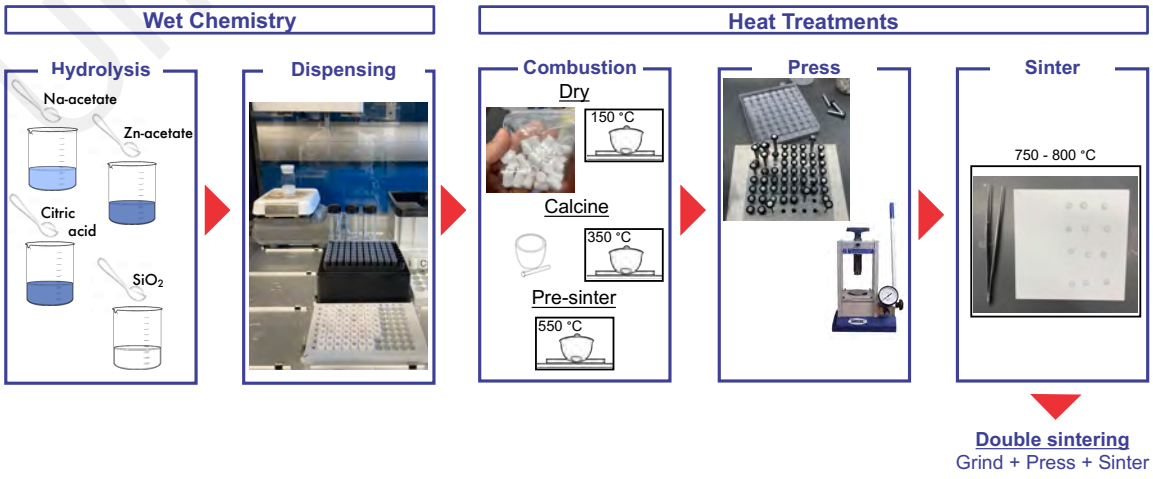

Figure 3.3: Process flow for high-throughput citrate-assisted sol-gel synthesis employed in the later phase of the project.

Similarly presented in **Section 3.3.2**, the wet chemistry starts with the hydrolysis of starting reagents at predetermined molarity. The same starting reagents were used for the synthesis of Clay-NZS as in **Section 3.3.2**. Stoichiometric amounts of sodium acetate and zinc acetate precursor solutions were then dispensed into 350 µl alumina cups held in an eight-by-eight 3D-printed sample holder using a solution-dispensing robot. This was followed by the addition of citric acid at citrate:metal volumetric ratio of 1:3. SiNP suspended in DI water was constantly stirred before being dispensed last into the sample solutions at stoichiometric amount, 10%, or 20% excess. Similar to **Section 3.3.2**, it was assumed that the molar weight of the Si nanoparticles to be equivalent to pure SiO_2.

As soon as the SiNP suspension was added into the sample solutions as a final dispensing step, the samples were straight away set into a series of heat treatments. Unlike in **Section 3.3.2**, the gelation step is skipped altogether in high-throughput. The alumina cups containing the sample solutions were immediately placed in a pre-heated oven set at 105°C and left to dry for 24 h. The resulting powder samples were then calcined in a box furnace at 350°C (2°C/min ramp) for 6 h in air to remove the organic solvents and further heat-treated to 550°C (2°C/min ramp) for 10 h in air to remove carbon. This additional pre-sinter heat treatment step was included to ensure the final sample pellet is as dense as possible. The pre-sintered sample powders were then crushed and pressed (~1.4 tonnes) to form green body pellets of 0.5 mm diameter using a hydraulic press. Next, the sample pellets were placed in a box furnace again to fully crystallize and sinter at temperatures of either 750, 800, or 850°C (2°C/min ramp) for 6 h to form white body pellets.

A big modification to the original synthesis steps is the double-sintering of ceramic whereby after the sample pellets have been sintered, they were crushed into powder again, re-pressed at 1.0 tonne, and re-sintered for 2 h. The modified synthesis procedure was

optimized in this high-throughput setting by making over 350 samples under various sintering and pressing conditions.

3.3.5 Ionic Doping of NZS in High-Throughput

Going across the periodic table, 22 different substituents were utilized for ionic doping of Clay-NZS, namely Mg, Al, Ca, Sc, Ti, V, Cr, Mn, Fe, Co, Ni, Cu, Ga, Sr, Y, Zr, Nb, Mo, Rh, Ag, Cd, and In. All the 22 substituents selected have starting reagents that are soluble in either water or ethanol for ease of hydrolysis and dispensing. The optimized procedure for high-throughput in **Section 3.3.4** was employed, where each substituent is dispensed into the alumina cups before SiNP. The overall stoichiometry of the doped samples was $Na_2Zn_{1-x}Si_{1-x}A_{2x}O_4$ (where A is the substituent). All substituents were initially tested at $x = 0.05$ and $x = 0.1$, while the promising compounds were later expanded to other substitution levels.

3.4 Structural Characterisation

3.4.1 X-Ray Fluorescence (XRF)

HNT and SiNP powders were studied under XRF to obtain the composition of oxides in the compounds. The phase compositions were used to determine whether Al_2O_3 in the inner lumen of HNT has been completely removed through acid leaching using H_2SO_4, thus forming SiNP. Existence of other phases were also noted to identify the sample purity and their role in the subsequent performance of Clay-NZS.

The XRF machine used was the Thermo Scientific ARL QUANT'X EDXRF Spectrometer. Sample of about 3 g were inserted into a sample holder, and readings were taken by a silicon drift detector.

3.4.2 Thermogravimetry and Differential Scanning Calorimetry (TGA-DSC)

The sample's thermal behaviour was evaluated using TGA-DSC. The study was first done onto the dry precursor powder of Synthetic-NZS after the sample has completed the wet chemistry part of the sol-gel synthesis. This is to evaluate the heat treatment steps necessary for combustion of sister elements as well as to determine the right temperature for the sample to undergo complete crystallisation. The same heating procedures were replicated to the synthesis of Clay-NZS. Next, TGA-DSC was also employed on the final systems of Clay-NZS SSE and Clay-NZS HybSSE to investigate the thermal stability of the samples, hence the temperature range for the samples' operability in varying temperatures for impedance measurements.

The TGA-DSC measurements were taken using Setaram LABSYS EVO thermal analyser. Measurements were taken at the temperature range of 25 – 850°C at 10°C/min under flowing N_2 gas.

3.4.3 X-Ray Diffraction (XRD)

XRD measurements were first taken on powder samples of Synthetic-NZS after each heat treatment to evaluate the evolution of powder samples in forming NZS. XRD measurements were also taken after the ceramic samples of Synthetic-NZS and Clay-NZS have undergone full synthesis and crushed into powders to evaluate their structural properties and to determine the right sintering temperature.

Using Malvern PanAlytical Empyrean XRD machine, the diffractometer was equipped with Cu Kα radiation source and assembled using Bragg-Brentano configuration, operating at reflection mode. XRD data were taken at room temperature across 2θ range of 10 – 80° with a step scan of 0.02° per 96 seconds. The measured experimental XRD structural data were then refined using Rietveld technique against the reference structures from the ICDD database in HighScore Plus software. This is to calculate the sample's

lattice parameters, phase compositions, and crystallite sizes. The refined data were further processed using VESTA program to obtain the Bragg peaks and schematic diagram of the structure.

3.4.4 High-Throughput X-Ray Diffraction (XRD)

In the high-throughput lab, the XRD diffractometer used was a combinatorial XRD that was custom-built using Malvern PanAlytical Empyrean with a Mo Kα radiation source and a GalaPIX area detector, operating in transmission mode. Powder samples were placed in an eight-by-twelve array sample holder for their XRD patterns to be collected in high-throughput. As described in detail by McCalla et al. (2021) the XRD patterns were processed in batches using the HighScore Plus software in such a way that yields precision and data quality comparable to that typically obtained with Cu radiation. Specifically, the processing (1) adjusts the scattering angles to match those obtained with a Cu-source for ease of comparison to the literature, (2) subtracts the $K\alpha_2$ peaks, and (3) refines the XRD patterns using Rietveld method. The phases used in the refinement were obtained from the ICDD database.

When the refinement shows that the sample consists of multiple phases, the relative densities of each phase in the ceramic compared to their theoretical values was calculated using **Equation 3.7** below:

$$Relative\ density\ (\%) = \frac{1}{\frac{wt\%\ Phase\ 1}{\rho_{Phase\ 1}} + \frac{wt\%\ Phase\ 2}{\rho_{Phase\ 2}} + \cdots + \frac{wt\%\ Phase\ n}{\rho_{Phase\ n}}} \quad (3.7)$$

where "*wt% Phase n*" is obtained from the result of Rietveld refinement and "$\rho_{Phase\ n}$" is the theoretical density of the given phase.

3.4.5 Fourier Transform Infrared Spectroscopy (FTIR)

The chemical interactions of the molecular constituents in the final samples were studied using FTIR performed using Perkin-Elmer Frontier FT-IR/FIR Spectrometer. Small amount of powder samples was placed on a sample plate to cover the diamond crystal and IR readings were taken using the Attenuated Total Reflection (ATR) method. Data were taken at 0.5 cm^{-1} resolution over the range of 600 – 4000 cm^{-1} to obtain the spectrum of molecular absorption and transmission in the samples. Spectra of the samples were then compared to the literature and with one another.

3.4.6 Field-Emission Scanning Electron Microscopy and Energy Dispersive X-ray Spectroscopy (FESEM-EDX)

The microstructures and elemental compositions of the samples were analysed using FESEM-EDX by Hitachi with a cold field emission source. Samples in either powder or pellet form were pasted on a carbon tape before being placed in a vacuum chamber. Images of the samples' surface and cross-sections were taken at 1.0 – 90.0 kV acceleration voltage to obtain micrographs of the sample at varying magnifications.

Through the same setup, EDX analysis were done on the samples using the Oxford Instrument's AZtecLive software, at acceleration voltage suitable for the targeted elements. The EDX analysis shows the elemental composition of a predefined area within the sample. The ratios of the elements were then calculated to identify the stoichiometry of the observed compound in the sample.

3.4.7 Density Analysis via Archimedes' Principle, Brunauer-Emmett-Teller (BET), Barrett-Joyner-Halenda (BJH) and t-Plot Methods

A lot of aspects within the project involved the measurement of density and porosity and thus, a number of approaches have been used on the samples to gather such insights. Firstly, the density of IL was determined using Rudolph Research Analytical's density meter to be compared with the literature. Then, the density of ceramic samples was evaluated through Archimedes' principles using a Sartorius density kit set on a 0.1 mg weighing balance, where the weight of sample pellets in air and in ethanol are compared, in order to obtain the density of the pellet.

In terms of porosity analysis of the sintered samples, IUPAC has classified the types of pores to include macropores (width >50 nm), mesopores (intermediate size), and micropores (width <2 nm) (International Union of Pure and Applied Chemistry, 2014). The macroporous volume of sintered sample pellets was evaluated using Archimedes' method in water based on **Equation 3.8** below:

$$V = \frac{m_{wet} - m_{dry}}{\rho_{water}} \tag{3.8}$$

where V is the macropore volume, m_{wet} is the mass of pellet soaked in water, m_{dry} is mass of pellet before soaking, and ρ_{water} is the density of water. Meanwhile, the volume of mesopores and micropores were directly obtained, via BJH and t-Plot methods respectively, using N_2 gas adsorption system in a surface analyser. The surface analyser is also used to measure the total surface area within a pellet using BET measurements.

The degassing program of the Micromeritics TriStar II Surface Area Analyser was set at 90°C for 1 hour and 200°C for 4 h. MicroActive software was used to analyse the isotherm data and churn out results for BET, BJH, and t-Plot calculation methods. These methods directly calculate the surface area and pore volume within the pellet for their respective pore types.

3.5 Electrochemical Measurements

3.5.1 Ionic Conductivity via Electrochemical Impedance Spectroscopy (EIS)

EIS equipment by Solartron was used to measure the impedance of individual sample pellets, sandwiched between two-blocking stainless steel electrodes, inside a temperature-controlled chamber. AC measurements were taken between RT and 500°C temperature range at 25°C step within the frequency range of 1 MHz to 10 Hz (100 mV amplitude). In between the temperature steps, samples were left to acclimatise for >30 mins before impedance measurements were taken. The sample's operable temperatures were determined by the ability of the instrument to capture the impedance of the compound at that particular temperature.

The obtained Nyquist plots from the EIS measurements were fitted with equivalent circuits in ZView to calculate the sample's conductivity using Ohm's Law, as described in **Equation 2.1**. The sample's ΔE_A were then calculated using the Arrhenius relation stated in **Equation 2.3**, based on their conductivity values at different temperatures. The impedance data were also used to calculate the sample's frequency-dependent conductivity values using **Equations 2.5** and **2.6**, from which the ionic hopping frequency can be derived.

3.5.2 High-Throughput EIS

Meanwhile, in high-throughput EIS, samples were placed on a 64-plate custom-made printed circuit board by Optima Tech, and then layered with spring-loaded custom-built stainless steel pistons on top to form a combi cell. The combi cell was then placed in a temperature chamber and loaded onto an in-house-assembled system of Pickering 64-channel multiplexer and Biologic SP-150 potentiostat. The setup was operated using an in-house-written software to measure EIS at frequencies 1 MHz to 1 Hz (100 mV

amplitude) for batches of 64 samples. Measurements were taken at temperatures 22°C (RT) and 48°C after the cell were left to acclimatise in the temperature chamber for 12 h.

The impedance data were analysed in batches using EC-Lab to fit the Nyquist plots of each sample with an equivalent circuit to calculate their ionic conductivities using **Equation 2.1**. The samples' ΔE_A were then also calculated using Arrhenius relation in **Equation 2.3**, based on the data obtained at the two temperature values.

3.5.3 Electronic Conductivity and Ionic Transference Number via Chronoamperometry

To fulfil the requirement to become an electrolyte, the electronic conductivity of the synthesised material needs to be negligible. This is investigated via chronoamperometry where the sample pellet is sandwiched between two blocking stainless steel electrode and subjected to a step potential of 1 V at RT. Experiments were undertaken using the equipment ZIVE MP2A Multichannel Electrochemical Workstation. The current across the sample pellet was measured instantaneously and continuously through time, until the current reaches a steady state. The ionic transference number is calculated after the steady state is achieved using **Equation 2.7**.

3.5.4 Electronic Conductivity in High-Throughput

Meanwhile, in high-throughput, the chronoamperometry was done on a lab-built electrochemical system assembled using Keithley 213 quad voltage source and Keithley 2750 multichannel multiplexer. Similarly, a step voltage of 1 V was applied across sample pellets at RT. The current across a batch of 64 samples in a combi cell were measured every second for ~3 h to ensure steady state. The system obtains current by measuring the voltage drop across 10 kΩ precision resistors. Based on the large internal impedance of the Keithleys, the precision of the instrument is <1 nA. The electronic conductivities of

the samples were then calculated using Ohm's Law as in **Equation 2.1** when the current reached a steady state.

3.5.5 Na^+ Ion Transference Number via Chronoamperometry

On the ZIVE MP2A Multichannel Electrochemical Workstation, individual sample pellets were polarised in a symmetrical cell of non-blocking Na metal electrodes by 1 V step potential until a steady state of current was reached. EIS measurements were taken before and after the chronoamperometry and the Na^+ ion transference number was calculated using **Equation 2.9**.

3.5.6 Electrochemical Stability Window via Voltammetry

The ESW of the samples were initially evaluated using the LSV method, where the experiments were undertaken using the ZIVE MP2A Multichannel Electrochemical Workstation. The individual sample pellet was sandwiched between two blocking stainless steel electrodes and a potential is applied across the sample, with voltage being swept from 0 V to 5 V at 5 mV s^{-1} sweep rate. The ESW of the sample was determined to be the intersection between the tangent of decomposition and the voltage axis. This method serves as a preliminary evaluation of the ESW of samples that were synthesised at the early stage of the project.

3.5.7 Electrochemical Stability Window via Voltammetry in High-Throughput

In later stages of the project, the samples' ESW were evaluated through CV in high-throughput by cycling the sample as an electrode material in an electrochemical cell. This method has been shown to give a more accurate stability windows, while simply performing a voltammetry across the sample may over-estimate its stability (Jonderian & McCalla, 2021; Potts et al., 2019). Firstly, the sample pellets were crushed to become the active material of a composite electrode that is mixed with ~20 wt% carbon black and

~20 wt% PVDF, in NMP solution. The composite is then drop-casted onto either an Al- or a Ni-plated PCB and dried in an oven at 80°C overnight, which will become the working electrode in the 64-plate combi cell. The electrolyte used for the combi cell was 1 M sodium perchlorate in propylene carbonate with 2 wt% fluoroethylene carbonate, soaked in a GF/D glass microfiber separator. The counter electrode was Na metal. The combi cell was assembled inside a glove box and sealed before being brought outside.

To obtain the upper limit of the samples' ESW, the Ni-plated PCB was used, and the CV was employed at a sweep rate of 0.1 V/h over the voltage range 2.7 – 5.5 V vs Na/Na^+ for 1.5 cycles. Meanwhile, to obtain the lower limit of ESW, the Al-plated PCB was used, and the CV was employed from 2.7 to 0.1 V vs Na/Na^+ for 1.5 cycles at the same scan rate. The oxidation and reduction potentials were then determined by comparing the CV patterns with the control cells where the active materials were absent, but carbon black and binder were present in the same amounts as the test cells.

3.5.8 Stability against Na Metal

To evaluate a sample's reversibility as well as stability against Na metal, CV was employed by ZIVE MP2A Multichannel Electrochemical Workstation in a half-cell setup where the sample is sandwiched between the working and reference electrodes. The working electrode is a composite electrode which active materials were made up of NMO and Clay-NZS mixed at 75:25 ratio. The active materials were then mixed with PVDF and carbon black at 80:10:10 ratio before being tape-casted onto Al current collector using the doctor-blading method and dried in vacuum oven at 90°C overnight. Meanwhile, Na metal was made the reference electrode. The cell was assembled in a battery jig inside a glove box and sealed before being brought outside. CV measurements were taken from 1.5 V to 4 V at 100 mV/s rate, over four cycles. The cyclic stability and peaks of oxidation and reduction were analysed to evaluate the cellular activity and stability across the redox process.

3.5.9 Stability against Na Metal in High-Throughput

Another method that was used to evaluate samples' stability against Na-metal was by chronoamperometry with cell assembly that is similar to finding the Na-ion transference number, as described in **Section 3.5.3**. The sample pellet was sandwiched between Na-metal in a Swagelok-type cell assembled in a glove box and sealed before being brought outside. The cell was then subjected to a direct current (DC) test on a Biologic potentiostat where the voltage was held at 0.1 V for 5 min, and the current was measured every 0.002 s. After the DC test, EIS was performed to determine the changes in impedance during the Na exposure and DC test. This method allows for tracing the presence of passivation layer when the sample is exposed to Na metal at a potential.

CHAPTER 4: SYNTHESIS OF CLAY-NZS SSE FROM HALLOYSITE CLAY

4.1 Extracting SiNP from HNT

It is understood that HNT has Al_2O_3 in its inner lumen that can be dissolved with H_2SO_4 in a process called acid leaching to leave out SiO_2 on its outer lumen (Gaaz et al., 2016). The dissolution eventually leads to the breakdown of the nanotubular structure of HNT to form SiNP. **Figure 4.1(a)** displays the renowned nanotubular structure of pure HNT before undergoing acid treatment, while **Figure 4.1(b)** shows the remains of the nanotubes that were broken down through the acid leaching process to form SiNP. This transformation is verified by running XRD, FTIR, as well as XRF experiments on the sample powder before and after the acid treatment.

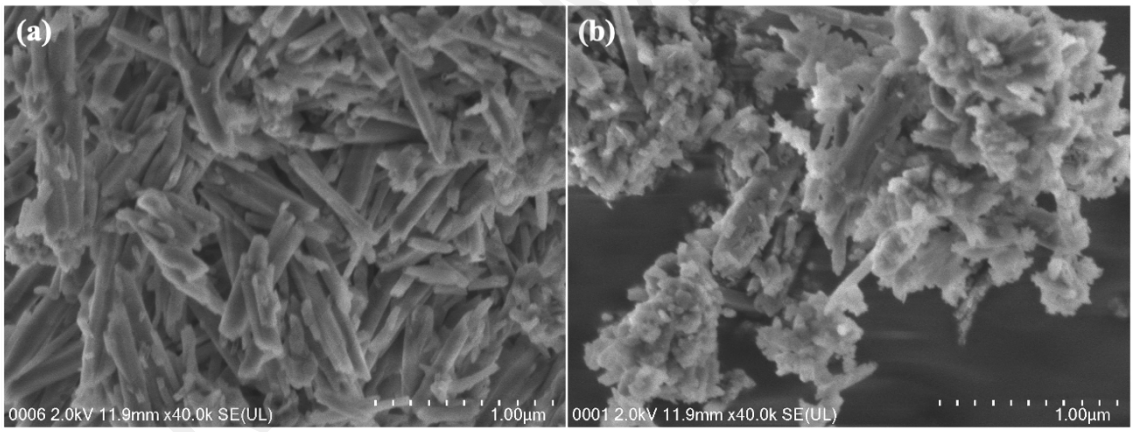

Figure 4.1: Micrographs of (a) pure HNT showcasing its nanotubular morphology, and (b) acid-treated HNT showing the disintegration of the nanotubular structure to form SiNP.

On the other hand, **Figure 4.2** shows the XRD spectra of HNT and SiNP. **Figure 4.2(a)** displays the characteristic HNT spectra as per the literature (Gaaz et al., 2016; Garcia-Garcia et al., 2017; X. Zhou et al., 2016), while **Figure 4.2(b)** shows the XRD pattern after the acid treatment. The two XRD spectra prove that the acid treatment has completely modified the HNT to become a mixture of amorphous SiO_2 (broad peak across $2\theta = 15.0°$ to $2\theta = 31.5°$) and crystalline SiO_2 (sharp peaks at $2\theta = 21.0°, 26.7°$), confirming the yield of SiNP.

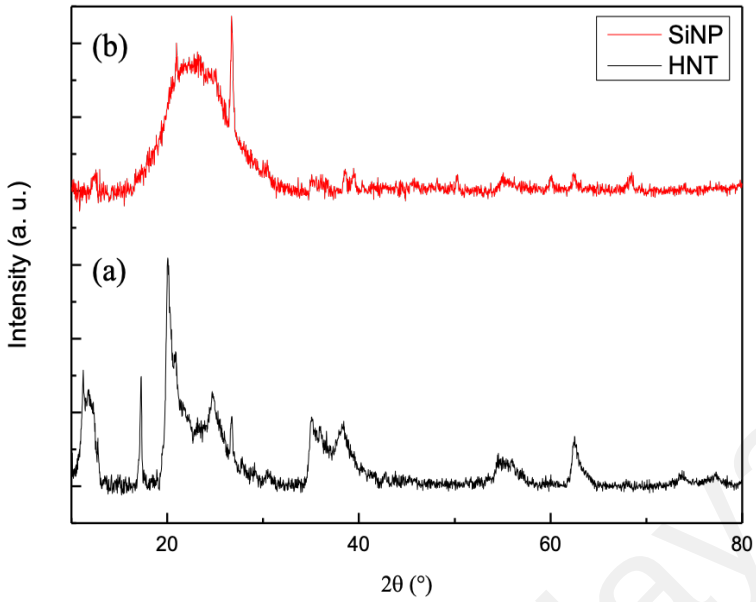

Figure 4.2: XRD spectra of (a) HNT before acid treatment, and (b) SiNP yielded after acid treatment.

The FTIR spectra of the two samples are shown in **Figure 4.3**, where the characteristic peaks of HNT in **Figure 4.3(a)** are seen to have diminished in **Figure 4.3(b)**. In particular, the peaks at 3620 cm^{-1} and 3695 cm^{-1}, which represent the O-H stretching vibrations in Al-OH groups (H. Lun et al., 2014). Instead, they are replaced by a broad peak around 3366 cm^{-1} indicating remnants of water content being present after Al has been extracted. Absorption peaks at 1070 cm^{-1} and 944 cm^{-1} assigned to Si-O-Si and Si-OH stretching vibration respectively (Gaaz et al., 2016) are present in both **Figures 4.3(a)** and **4.3(b)**, indicating that SiO_2 is unaffected by the acid treatment. Besides that, **Figure 4.3(b)** is also characteristic to that of a silica nanoparticle in the literature (Feifel & Lisdat, 2011), further confirming the transformation of HNT to SiNP.

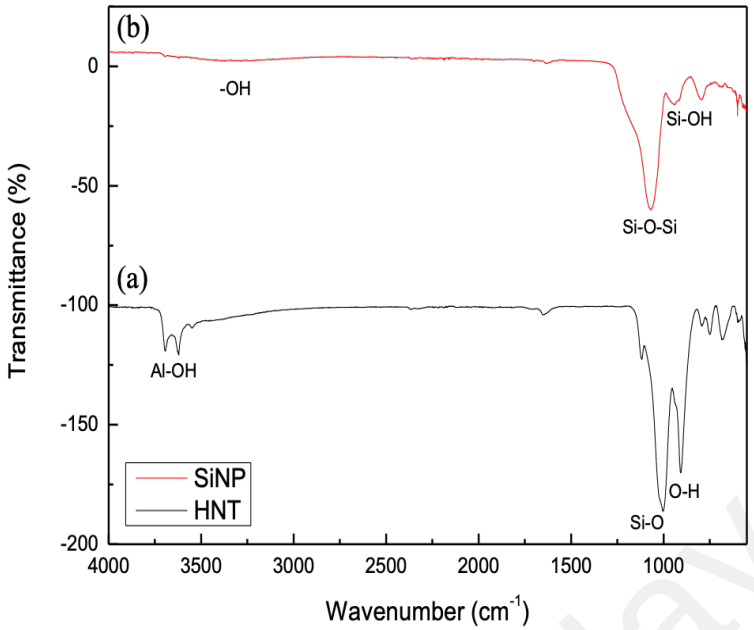

Figure 4.3: FTIR spectra of (a) HNT, and (b) SiNP, indicating the loss of alumina in the compound.

The result of XRF measurements shown in **Table 4.1** quantifies the Al_2O_3 content to be reduced from 27.4(6)% to 6.7(4)% upon acid leaching, demonstrating a reduction of 21(1)%. Moreover, the concentration of SiO_2 improved by 13(1)% to become 83.5(4)%. Other oxides content are unaffected, with the exception of SO_3 that increased tremendously, contributed by the sulphates from H_2SO_4 during the acid treatment. Nevertheless, its presence is not significant enough to modify the final structure of SiNP. Therefore, it can be concluded from the above that while SiNP is successfully harvested from HNT, its content is not entirely phase pure.

Table 4.1: XRF data of HNT and SiNP

Compound / m%	Halloysite Nanotube (HNT)	Silica Nanoparticle (SiNP)
SiO_2	70.5	83.5
Al_2O_3	27.4	6.7
P_2O_5	0.8	0.5
Fe_2O_3	0.5	0.2
SO_3	0.3	8.7
CaO	0.3	0.3

4.2 Synthesis and Structure of Pristine NZS SSE

TGA-DSC was employed on dried precursor powder of Synthetic-NZS to obtain the optimum thermal conditions to synthesise the standard polycrystalline of NZS, as shown in **Figure 4.4(a)**. After the water boiling point at ~100°C, the TG data exhibits major decomposition between 238.7°C and 518.0°C (Δm_1 = 30.75%), with the DSC data displaying exothermic peak at 338.3°C. This decomposition occurs due to the combustion of the organic compounds used to facilitate the wet chemistry in sol-gel synthesis, namely the acetates and citrates. Thus, a calcining step at 350°C is necessary to ensure that the organic compounds are combusted to not interfere with the crystallisation process at higher temperature. Subsequent peaks of exothermic heatflow at higher temperatures, alongside further decomposition slope in TG, indicate that additional combustion processes occur between 518.7°C to 750.0°C (Δm_2 = 4.74%). The last exothermic peak

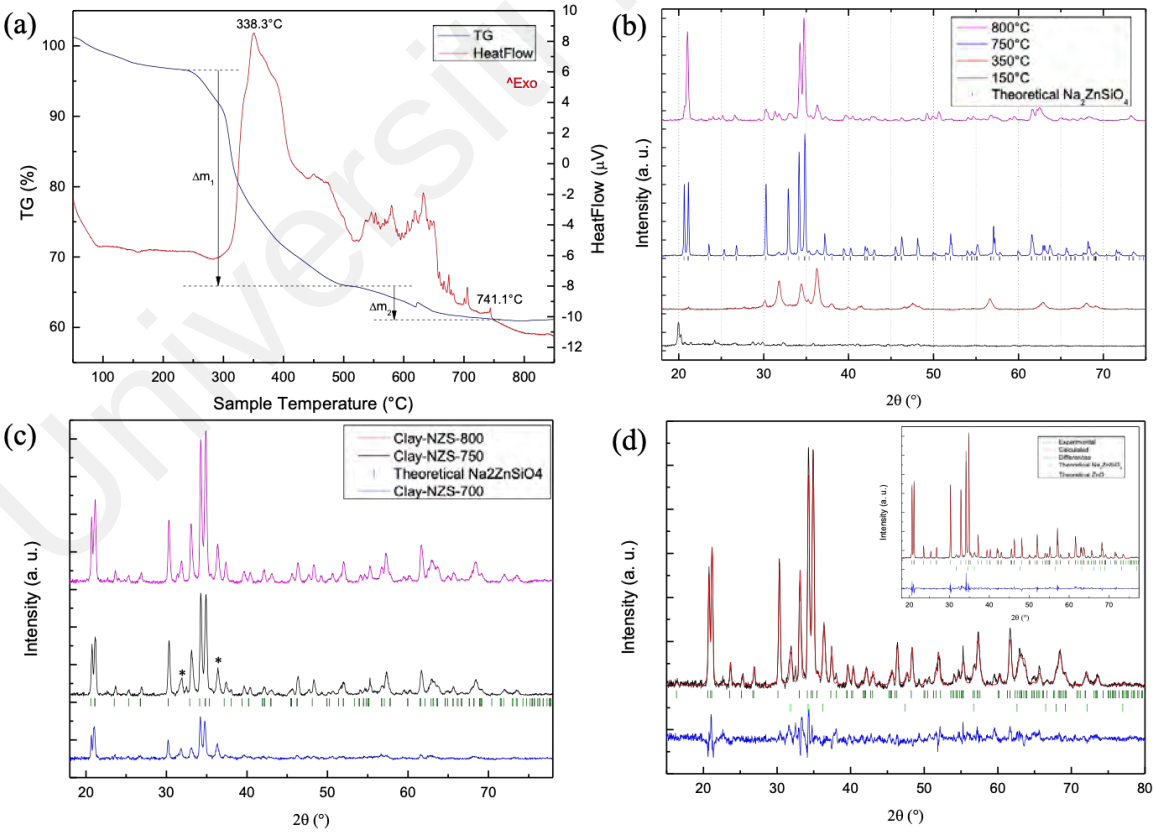

Figure 4.4: (a) TGA-DSC of NZS, showing the two main decompositions Δm_1 and Δm_2, (b) XRD patterns of Synthetic-NZS across different temperatures of heat treatments, showcasing polycrystalline peaks at 750 °C, yet disappearing at 800 °C, (c) XRD spectra of Clay-NZS sintered at different sintering temperatures. Star symbol indicates peak of impurity due to ZnO, and (d) Refined XRD data of Clay-NZS. Inset is the refined XRD data of Synth-NZS.

is seen at 741.1°C, signifying the crystallisation point of NZS because the mass and heat flow of sample has stabilised beyond this temperature point. Therefore, any heat treatment at temperature upwards of 750°C is considered a suitable sintering temperature, as crystallisation is acknowledged to be complete beyond this point.

To complement the deduction made from TGA-DSC measurements, **Figure 4.4(b)** shows the evolution of the XRD patterns of Synthetic-NZS sample powders retrieved after each heat treatment step. The precursor powder obtained after the drying step at 150°C has an XRD spectrum that displays a small broad peak around 20° scattering angle. This represents the amorphous nature of the sample, which is in agreement with the theory that polymeric chains of citrate-metal complex ligands are formed in a citrate-assisted sol-gel synthesis (Danks et al., 2016). When the sample is calcined at 350°C, the XRD data shows that this broad peak disappears, indicating the disintegration of the polymeric chain, thus confirming the combustion of organic components. After heating at 750°C, crystallinity is observed in Synthetic-NZS, in agreement with the theorical peaks of Na_2ZnSiO_4. But, when the temperature is increased to 800°C, some peaks have disappeared.

The same heating procedure was then done onto the synthesis of Clay-NZS and **Figure 4.4(c)** shows the XRD spectra when different sintering temperatures were used. At 700°C, the peaks corresponding to Na_2ZnSiO_4 has not fully formed, indicating that crystallisation process is not yet complete. This is expected from the results of TGA-DSC of Synthetic-NZS above, where crystallinity should only occur above 741.1°C. Peaks matching the theoretical peaks of Na_2ZnSiO_4 are only visible when the sample was heat-treated to 750°C, which is similar to the behaviour of Synthetic-NZS when sintered at the same temperature. Even so, concurrent peaks due to ZnO emerged, marked by the star symbol on **Figure 4.4(c)**. This is an impurity that was not significantly seen by eye in the XRD

spectrum of Synthetic-NZS sintered at the same temperature. Another difference that is eminent in Clay-NZS is that the Na_2ZnSiO_4 peaks are preserved when the sample was heated to 800°C, while Synthetic-NZS showcases the breakdown of the material at this heating temperature through the loss of peaks in its XRD spectrum in **Figure 4.4(b)**.

Thus, Rietveld refinement was performed on the XRD spectra of both samples sintered at 750°C, as shown in **Figure 4.4(d)**. It was found that both samples crystallised to the monoclinic structure of *P1c1* space group Na_2ZnSiO_4 and the hexagonal structure of *P63mc* space group ZnO. Rietveld refinement done onto their XRD measurements obtained a goodness of fit (χ^2) of less than 2, which gave confidence to their quantitative results illustrated in **Table 4.2**. As expected from the noisier peaks of Clay-NZS shown in **Figure 4.4(d)**, Clay-NZS has a lower weight percentage of the Na_2ZnSiO_4 phase at 88.0%, whereas Synthetic-NZS has 95.8% purity of Na_2ZnSiO_4. Besides that, there is no significant difference in the lattice parameters for the Na_2ZnSiO_4 phase of both Clay-NZS and Synthetic-NZS as shown in **Table 4.2**.

Table 4.2: Rietveld refinement values of Synthetic-NZS vs Clay-NZS

		Synthetic-NZS	Clay-NZS
	R_{wp} [%]	3.664	5.610
	GOF (χ^2)	1.950	1.842
Phase	**Na_2ZnSiO_4 [%]**	95.8	88.0
Phase	**ZnO [%]**	4.2	12.0
Lattice parameters of Na_2ZnSiO_4	**a [Å]**	5.2486	5.2469
Lattice parameters of Na_2ZnSiO_4	**b [Å]**	5.4447	5.4218
Lattice parameters of Na_2ZnSiO_4	**c [Å]**	8.7663	8.7834
Lattice parameters of Na_2ZnSiO_4	**α [Å]**	90	90
Lattice parameters of Na_2ZnSiO_4	**β [Å]**	126.69	126.58
Lattice parameters of Na_2ZnSiO_4	**γ [Å]**	90	90
Lattice parameters of Na_2ZnSiO_4	**V [Å^3]**	200.90	200.65
	Crystallite size [Å]	4154.1	406.9

Synthetic-NZS was subjected to further analysis to probe the structural stability of its phase. The schematic diagrams of the NZS crystal structure are shown in **Figure 4.5(a-d)**, at various angles. It was found that not all Na atoms in the lattice assemble themselves to form tetrahedral coordination with their neighbouring atoms. Instead, only Na atoms occupying the Na_2 sites have a four-coordinate polyhedron whilst Na atoms occupying Na_1 sites form a five-coordinate polyhedron. Furthermore, the Na_1 polyhedra share edges with Na_2 (seen in **Figure 3(c)**), Si (seen in **Figure 3(c)**), and also Zn (seen in **Figure 3(d)**). By Pauling's rules (Carter & Norton, 2013), such assembly is not a stable ionic structure because the cations are considered to be "unreasonably close". The most stable structure for Na_2ZnSiO_4 can be observed through the computational work of (Persson, 2014a) using DFT calculation, where all cations form tetrahedral coordination with neighbouring anion. Rodríguez-Ramírez et al. (2020) attempted to synthesise Na_2ZnSiO_4 and also obtained a ZnO content of <5%. Therefore, empirically, this phase composition can be considered phase-pure because the minute ZnO content is necessary to stabilise the whole structure of synthesised NZS due to its unstable ionic assembly (Carter & Norton, 2013).

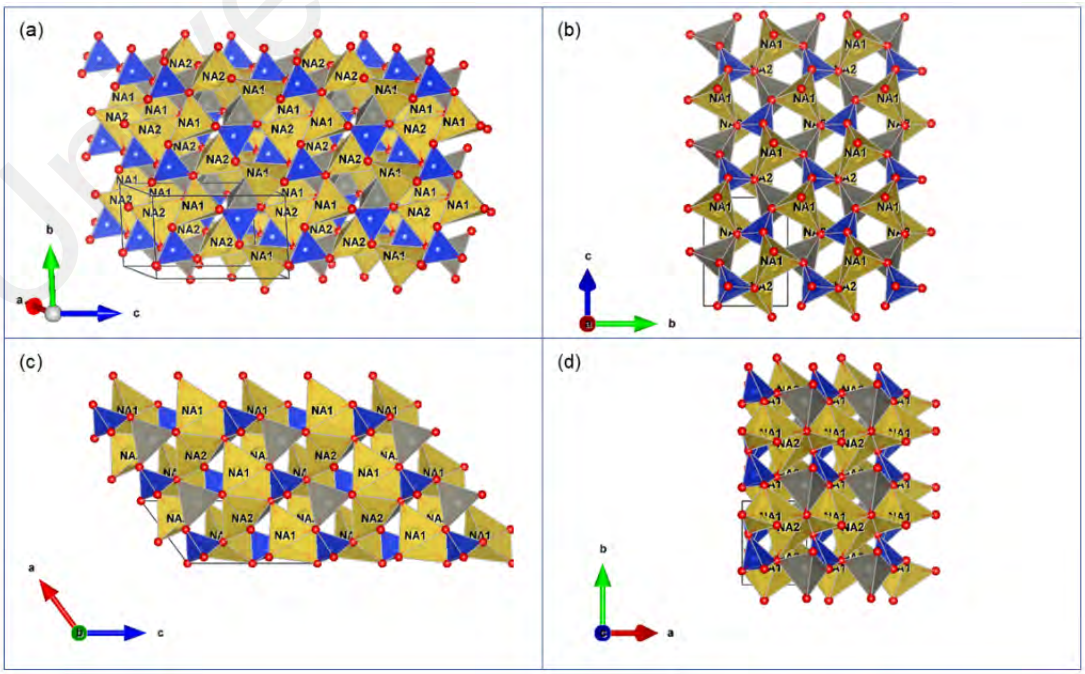

Figure 4.5: A schematic diagrams of refined NZS crystal structure (Na: yellow; Zn: grey; Si: blue; O: red).

On the other hand, the calculated crystallite size of Clay-NZS is found to be significantly smaller, where categorically, 406.89 Å denotes that Clay-NZS is nanosized (A. K. Singh & Singh, 2016). This is also notable qualitatively in the XRD spectrum of Clay-NZS in **Figure 4.4(d)**, where its peaks are significantly broader than Synthetic-NZS. This is further confirmed by comparing the micrographs of Clay-NZS and Synthetic-NZS, as shown in **Figure 4.6**. The different scales used in **Figure 4.6(a)** and **Figure 4.6(b)** made evident that the spherical grains of Clay-NZS are much smaller than that of Synthetic-NZS, with the former ranging between 50 – 70 nm whilst the latter being ~200 nm. Therefore, this micrograph solidifies the fact that Clay-NZS forms a nanocrystalline ceramic. Rod-like grains are also observed in **Figure 4.5(a)**, which is later identified to be ZnO. Such rod-like structure is not evident in the micrographs of Synthetic-NZS, which lack of presence confirms the phase purity of NZS.

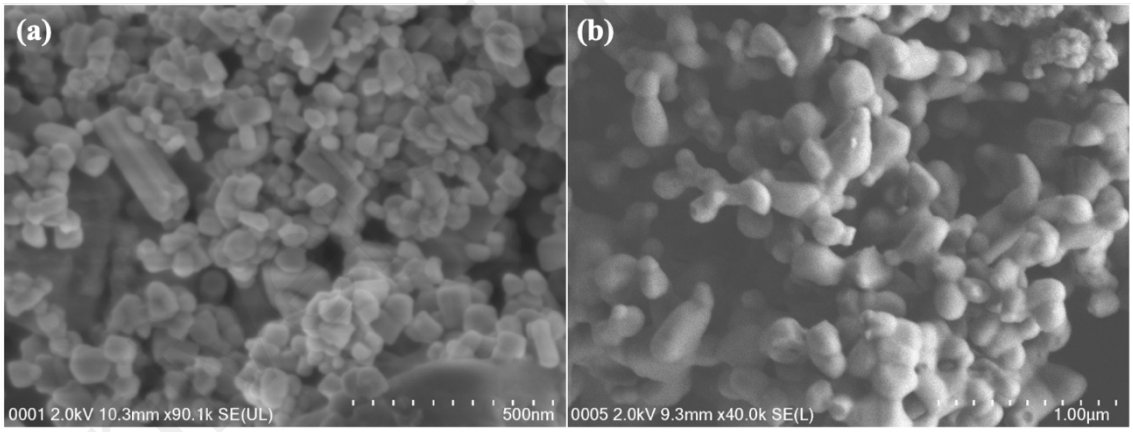

Figure 4.6: Micrographs of (a) Clay-NZS, and (b) Synthetic-NZS.

These results concluded that although Synthetic-NZS and Clay-NZS both form the desired phase of Na_2ZnSiO_4, synthesising Pristine NZS SSE from SiNP showcases a slight deviation of structural behaviour and characteristics when compared to synthesising it with the standard starting reagents. Most importantly, halloysite clay has proved to allow for the synthesis of nanocrystalline NZS, hence possibly encouraging nanoionics (Joachim Maier, 1995) in Clay-NZS, the desirable structure for fast ionic transport.

4.3 Chemical and Physical Characteristics of Pristine NZS SSE

Upon establishing the right procedure for the synthesis of Pristine NZS SSE, the chemical and physical characteristics of Synthetic-NZS and Clay-NZS were probed. Besides XRD, FTIR is also known to provide the fingerprint of a material, albeit in terms of chemical interactions and bonds within the compound. **Figure 4.7(a)** shows how the two samples are compared. It is found that similar to their XRD data, the FTIR spectra of Clay-NZS and Synthetic-NZS are comparable to one another, but not exactly the same. Both samples exhibit the characteristic SiO_4 peak in a silicate (Chandra Babu & Buddhudu, 2011) at about 887.5 cm^{-1}, with similar intensity. Other prominent peaks are the ones at wavenumber 560.5 cm^{-1} and 1435.5 cm^{-1}, attributed to the vibration due to Zn-O (Praseptiangga et al., 2020) and Na-O (Miller & Wilkins, 1952) stretching, respectively. Even so, the peak intensity due to Na-O is seen to be significantly higher in Clay-NZS than in Synthetic-NZS, indicating higher concentration of such bond (Ashenhurst, 2020). This may imply higher concentration of Na^+ in the compound. Paired with the broader peak of Zn-O in Clay-NZS, it is possible that there are additional defects within the lattice of Clay-NZS that encourage higher concentrations of Na^+. Next, the broad peak between 2567.0 cm^{-1} and 3643.0 cm^{-1} is very substantial in Clay-NZS but absent in Synthetic-NZS. Such peak is also present in SiNP, as shown in **Figure 4.3(b)**, demonstrating the continued existence of -OH bond from the halloysite clay through to Clay-NZS, albeit it remains undetected in the structure when investigated via XRD. Traces of such bond and element in Clay-NZS may cause enhanced defects in its lattice, increasing the possibility of the sample having higher intragrain ionic conductivity.

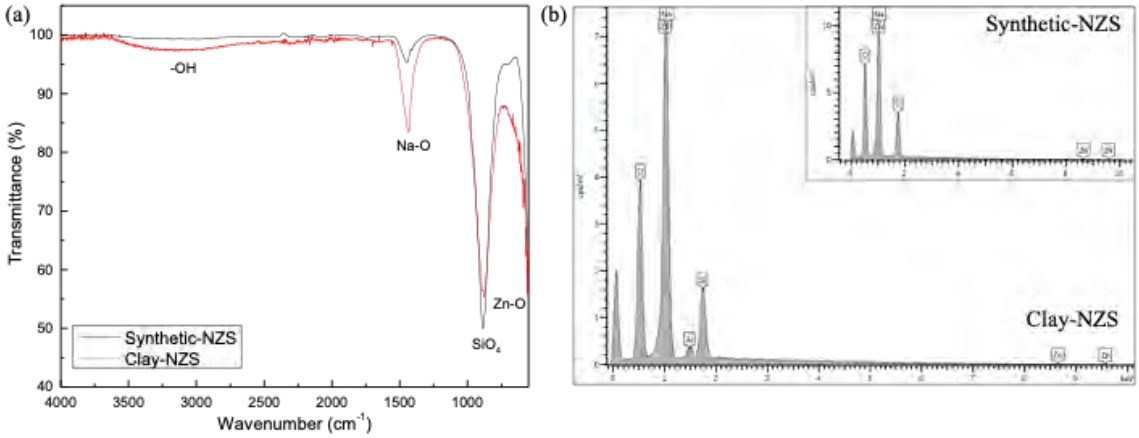

Figure 4.7: (a) FTIR spectra of Clay-NZS and Synthetic-NZS, and (b) EDX analysis of Clay-NZS and Synthetic-NZS where the first peak in both graphs denotes the carbon tape used to hold the pellets.

On the other hand, **Figure 4.7(b)** shows the comparison of EDX measurement done onto Clay-NZS and Synthetic-NZS. All peaks correspond to the atoms expected to be present in both Na_2ZnSiO_4 and ZnO, except for the small amount of Al found in Clay-NZS. This shows that although the acid treatment is successful in yielding SiO_2, there is residual Al being carried forward to the synthesis of NZS, brought by the small traces of Al_2O_3 in SiNP, as discussed in **Section 4.1**. Similar to the result obtained from FTIR, the XRD data of Clay-NZS did not signal any new phases due to Al in the compound. Therefore, although the concentration is unknown, it is probable that the Al is doped into NZS, at the interstitial, causing defects to the lattice structure. Al doping at interstitial may induce Frenkel defects (Carter & Norton, 2013) and give rise to the overall increase of ionic conductivity as well.

As pointed out in Chapter 2, ionic conductivity in a polycrystalline is driven by both the intra- and inter-grain resistance, namely R_g and R_{gb}, respectively. While the results of FTIR and EDX contribute more on the understanding of the samples' intragrain characteristics, their inter-grain characteristics may be understood better via pore analysis. The results of the pore volume and surface area analysis done on the white body pellets of Clay-NZS and Synthetic-NZS are shown in **Table 4.3**. For all pore categories, the volumes are found to be much smaller in the sample pellet of Clay-NZS compared to

Synthetic-NZS. This means that under the same pressing and sintering conditions, Clay-NZS is able to form a more densely packed ceramic compared to Synthetic-NZS. This is further confirmed by the lesser surface area within the pellet of Clay-NZS. Such high density is much attributed to the nanosized grain that can make the same weight of powder be more compact when pressed into a pellet. A denser pellet allows for a greater contact between the grains, hence reducing the R_{gb}.

By virtue of having additional defects in the lattice as well as having a better grain-grain contact, it is concluded that Clay-NZS is capable of having a much higher ionic conductivity than Synthetic-NZS due to the possible reduction of both R_g and R_{gb}.

Table 4.3: Pore volume and surface area analysis of Synthetic-NZS and Clay-NZS.

		Synthetic-NZS	Clay-NZS
Pore volume ($cm^3\ g^{-1}$)	**Macropore**	0.398562	0.059499
	Mesopore	0.008652	0.003131
	Micropore	0.000822	0.000025
Surface Area ($m^2\ g^{-1}$)		3.1849	2.3321

4.4 Ionic Conductivity of Pristine NZS SSE

Figure 4.8(a-b) shows the collection of Nyquist plots of Clay-NZS and Synthetic-NZS across their respective operable temperatures. Evidently, Synthetic-NZS has an operable temperature at upwards of 300°C ($\sigma_{300(\text{Synthetic-NZS})} = 9.44 \times 10^{-8}$ S cm^{-1}). that is typical of an oxide, while Clay-NZS's operable temperature is lowered to 175°C ($\sigma_{175(\text{Clay-NZS})} = 8.74 \times 10^{-9}$ S cm^{-1}). They both exhibit the semicircle shape characteristic of a dielectric polycrystalline. This semicircle reduces in size as temperature increases for both Clay-NZS and Synthetic-NZS, due to the mobile ions in the lattice obtaining thermal energy to hop from one site to another. This denotes a negative temperature coefficient of resistance (NTCR) behaviour, correlated to the increased mobility of the charge carrier as temperature increases (Adnan et al., 2019).

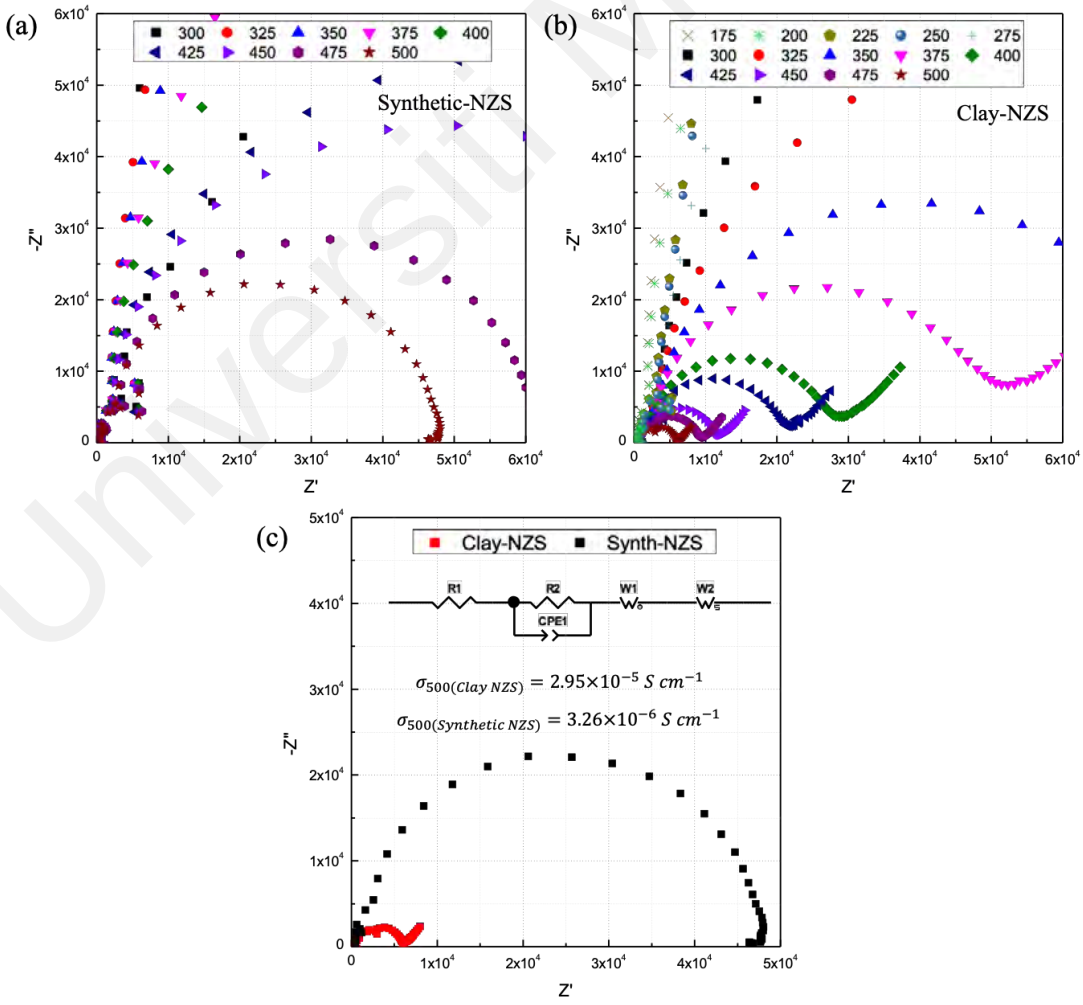

Figure 4.8: Nyquist plots of (a) Synthetic-NZS at 300 - 500°C, (b) Clay-NZS SSE at 175 - 500°C, and (c) Synthetic-NZS and Clay-NZS SSE at 500°C, with the equivalent circuit shown inset.

Each Nyquist plot was fitted using the equivalent circuit displayed in **Figure 4.8(c)**, which is derived from the common Randles circuit (Choudhary et al., 2017). In the Randles circuit, R1 represent the electrode-electrolyte interfacial resistance while R2 and CPE makes up the semicircle for ionic hopping within the sample. Additional components include W1 and W2, which are the Warburg diffusion elements in an open and short circuit respectively. The open Warburg is used due to the finite length of the sample while the short Warburg is used due to the localised porosity of the polycrystalline SSE. In all plots of Synthetic-NZS and Clay-NZS, R1 is not very significant due to the sheer size of R2 in the samples. While most polycrystalline would illustrate two semicircles in the Nyquist plot to showcase both R_g and R_{gb}, the Nyquist plots of both Synthetic-NZS and Clay-NZS only exhibit a single semicircle. It is deduced that R2 bears both the R_g and R_{gb} for the samples, where R_g is embedded within the larger semicircle of R_{gb}. Therefore, ionic conductivities were calculated in total using R2 being inputted into **Equation 2.1**. Meanwhile, the diffusion element is almost non-existent in Synthetic-NZS, evident by the lack of "tail" after the semicircle. This suggests that mobile ions passing through Synthetic-NZS SSE are largely transported through hopping instead of having some component of diffusion as shown in Clay-NZS.

The Nyquist plots of Synthetic-NZS and Clay-NZS at 500°C are isolated from the rest to compare in **Figure 4.8(c)**. The conductivities of Clay-NZS and Synthetic-NZS at this temperature were calculated to be 2.95×10^{-5} S cm^{-1} and 3.25×10^{-6} S cm^{-1}, respectively. Noticeably, the difference between the two samples is of one order magnitude from one another. As discussed in **Section 4.3**, a lot of components within the sample of Clay-NZS are at play that can contribute to its tremendous reduction in resistance, be it intra- or inter-grain. Nevertheless, it is believed that R_{gb} dominates, especially since only one

semicircle is displayed in the Nyquist plot. Therefore, it is deduced that the smaller semicircle of Clay-NZS is largely attributed to the nanocrystallinity and better packing of the sample. Nanosized grains that are in good contact allow for the space charge at the granular interface layer to dominate the overall system (Joachim Maier, 1995), which in turn reduces R_{gb} significantly (Schoonman, 2000).

A plot of conductivity against inverse of temperature was charted for both samples in **Figure 4.9** in order to calculate the ΔE_A required for ionic mobility using the Arrhenius relation in **Equation 2.3**. Their activation energies were both calculated to be 0.71(2) eV, which is comparable to the ΔE_A of NZS reported in (Grins, 1982). Therefore, the energy required to necessitate ionic conduction in both Clay-NZS and Synthetic-NZS are the same, anchored by the fact that they are of the same compound. Yet, Clay-NZS is a better ionic conductor due to numerous factors, affording it to operate at a lower temperature, therefore yielding the potential of expanding the usability of NZS in a practical system.

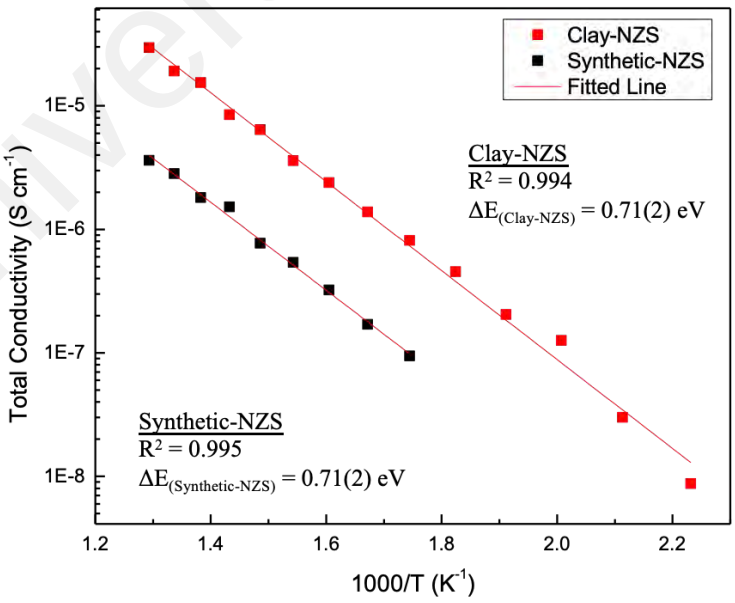

Figure 4.9: Arrhenius plot of Synthetic-NZS and Clay-NZS to obtain the activation energy, ΔE_A, for ionic conduction.

4.5 Frequency-Dependent Ionic Conduction of Pristine NZS SSE

Z values gathered from EIS measurements across temperatures were used to derive σ_{AC} for Clay-NZS and Synthetic-NZS using **Equations 2.5** and **2.6**. In the graph of σ_{AC} against ω shown in **Figure 4.10(a-b)**, three regions are observed across frequencies for both samples. The first region is at the lower frequency range, where polarisation comes into effect for ionic diffusion, particularly evident in Clay-NZS. This was reflected by the prominent diffusion element in the Nyquist plot of Clay-NZS and the lack of it in Synthetic-NZS, as per discussed in **Section 4.4**. The second region is at mid-range frequency, where the plateau manifests itself as σ_{DC}, the conductivity that is independent of frequency. The third region, at higher range, is the frequency-dependent region for conductivity as ions become mobile in variant to frequency. For both compounds, this frequency-dependency region starts further to the right as temperature increases, which means σ_{DC} extends to higher frequency with higher operating temperature. The frequency-dependent region abides the Jonscher UDR Power Law as in **Equation 2.7**, which unravels the mobile ions' behaviour. The data for lower temperatures of Clay-NZS, i.e., at 175°C and 200°C, are excluded due to the presence of two UDR slopes, as shown at the inset of **Figure 4.10(a)**. The two slopes signify the enhanced visibility of two semicircles in the Nyquist plot at those two lower temperatures compared to just a single semicircle in higher temperatures. Since subsequent analysis explores the trend across temperatures, these two data points are considered outliers.

From the UDR fit, the hopping frequency (ω_H) at each temperature is obtained by measuring the ω value from the plots in **Figure 4.10(a-b)** when $\sigma_{AC}(\omega) = 2\sigma_{DC}$. The values of ω_H are plotted against 1000/T, as shown in **Figure 4.10(c)**, to construct the Arrhenius relation and to obtain the energy due to ionic hopping (ΔE_H). It is found that both samples have two ranges of temperature with which the ΔE_H are of different values.

For both samples, ΔE_H at the higher temperature range, i.e., between 400 – 500°C, is lower than ΔE_H at lower temperature range. This means that less energy is required to move the ions at higher temperature. This is because ions have higher kinetic energy at higher temperature, thus lower energy barrier needed to be overcome. Therefore, based on the theory laid out by Almond & West (1983), the remaining energy used to activate the ions is mainly used for the creation of ions (ΔE_C). Since both samples have a constant ΔE_A throughout all of their operable temperatures. this implies that more ions are being mobilised at higher temperatures.

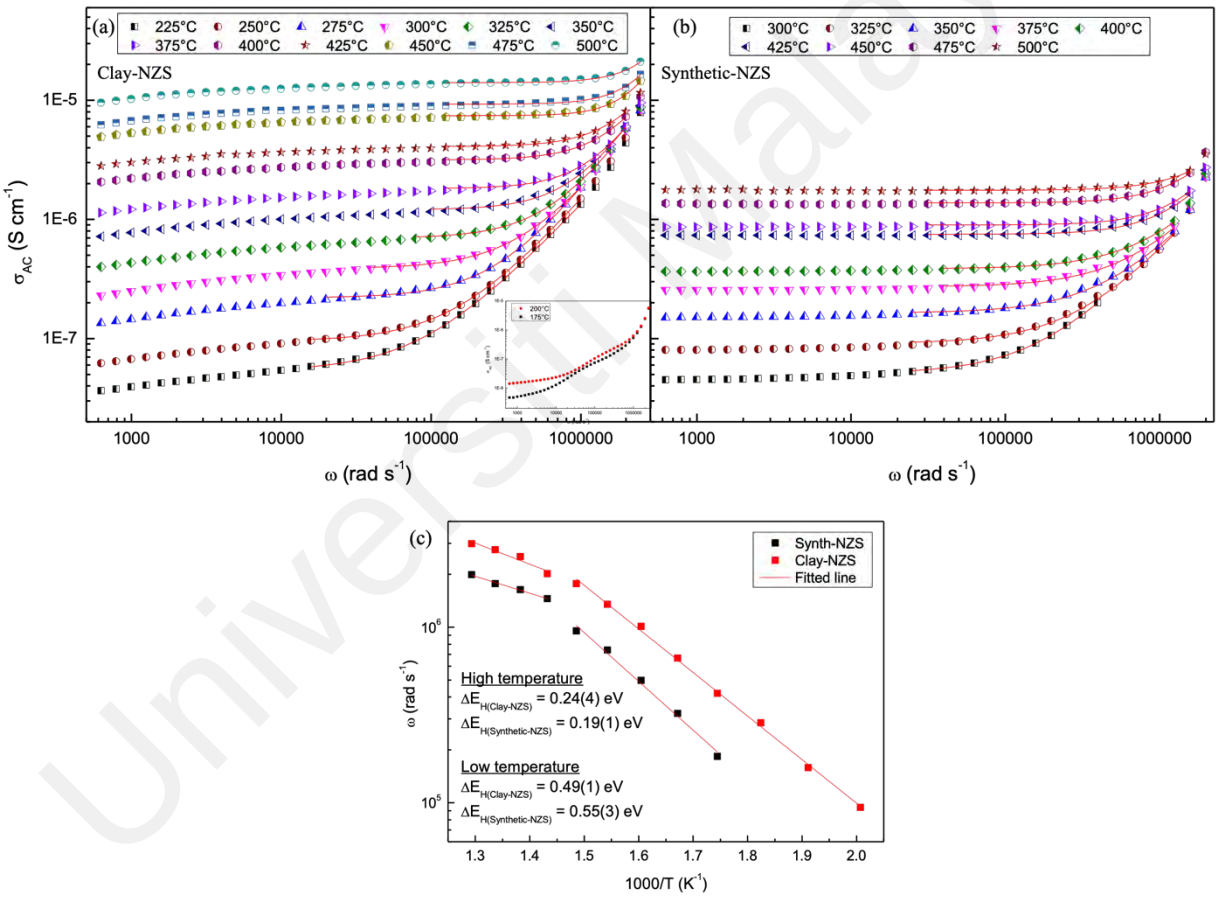

Figure 4.10: Frequency-dependent conductivity of (a) Clay-NZS with the outlier data inset, and (b) Synthetic-NZS across respective operable temperatures. Same scales are used to compare. (c) Arrhenius plot to obtain the energy required for ionic hopping, ΔE_H.

Besides having two values of ΔE_H across operable temperatures, the fact that $\Delta E_A \neq \Delta E_H$ in both compounds means that NZS's increased conductivity with temperature is not only due to increase in ω_H but also due to increase in charge concentration (n_c) in accordance to the Nernst-Einstein relation in **Equation 2.8**. Therefore, there are higher concentration of charge at temperatures above 400°C, which explains why most oxides are only operable at very high temperatures i.e., due to the high energy required to create mobile ions. **Table 4.4** shows the overall energy values for Clay-NZS and Synthetic-NZS. In every circumstance, less energy is needed for the mobile ions in Clay-NZS to be moved. This further strengthens the argument that nanoionics, as per the works of Joachim Maier (1995, 2009, 2014), allow for easier diffusion pathway.

Table 4.4: Energy values of Clay-NZS and Synth-NZS with respect to different temperature regions.

		Clay-NZS	Synthetic-NZS
Low temperature	ΔE_A	0.71(2) eV	0.71(2) eV
	ΔE_H	0.49(1) eV	0.55(3) eV
	ΔE_C	0.22(2) eV	0.16(5) eV
High temperature	ΔE_A	0.71(2) eV	0.71(2) eV
	ΔE_H	0.24(4) eV	0.19(1) eV
	ΔE_C	0.47(5) eV	0.52(3) eV

CHAPTER 5: DEVELOPMENT OF CLAY-NZS HYBSSE THROUGH INFUSION OF IL SOLUTION

5.1 Fabrication of Clay-NZS HybSSE

A HybSSE is obtained when the ceramic pellet of NZS is infused with IL solution of $Py_{14}TFSI$ and NaTFSI. The initial density of $Py_{14}TFSI$ was found to be 1.3949 g cm^{-3}, which is in agreement with the literature (Valderrama et al., 2012). Based on the pore analysis done on Clay-NZS in **Section 4.3**, the IL solution at this base density can be deemed to completely fill up the pores at ~20 wt% of the overall mass of the pristine sample pellet. **Figure 5.1** shows the micrograph of Clay-NZS HybSSE, after it was soaked with IL solution of ~20 wt%. It was observed under microscopy that the liquid flows between the pores of the pellet, albeit no excess liquid was seen through naked eye. This indicates that the ceramic in the form of a sintered pellet acts like an electrolytic host to house the IL solution, much like a wet sponge soaked with water. This microstructural environment of the HybSSE is bound to pose a good liquid-solid dynamic in achieving a high ionic conductivity.

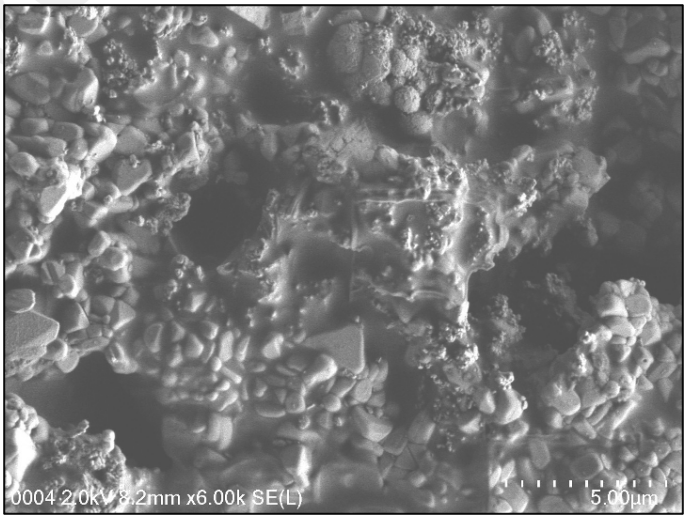

Figure 5.1: Micrograph of Clay-NZS HybSSE where the ceramic pellet is fully soaked with IL solution.

When NaTFSI is dissolved into $Py_{14}TFSI$ to make the IL solution, it was observed that as the concentration of NaTFSI salt increases, the viscosity of the IL solution increases. It was also observed that the IL solution with higher salt concentration took longer time to fully infuse into the pristine ceramic pellet. This is a direct indication that as the IL solution has more solute content, the ions within the solution diffuse less freely. **Figure 5.2(a)** shows how the atomic percentages in Clay-NZS HybSSE vary as NaTFSI salt concentration increase from 0 wt% to 10 wt%, 20 wt%, and 30 wt%. As anticipated, the atomic percentage of Na in the sample increases with increased concentration of NaTFSI. At the same time, the atomic percentage of carbon decreases. Since carbon atoms in the HybSSE largely came from Py_{14}^+ cation in the IL, this trend exhibits the reduction of the organic cation content in terms of overall percentage. This therefore shows that Na^+ in NaTFSI displaces Py_{14}^+ from $Py_{14}TFSI$ as the salt concentration in the HybSSE increases.

Meanwhile, the FTIR spectra in **Figure 5.2(b)** of Clay-NZS HybSSE at varied NaTFSI concentration show that across all salt concentrations in the IL solution, the original peaks of Clay-NZS remain. Instead, the primary peaks attributed to Clay-NZS are simply furnished with secondary peaks that are related to the bonds within $Py_{14}TFSI$ (*IR Spectrum Table & Chart*, 2022), demonstrating the fact that the IL solution infused into the ceramic pellet does not alter the chemical interactions within the pellet itself. This confirms that the pristine ceramic of Clay-NZS serves as a host to the IL solution in the overall HybSSE. On the other hand, peaks associated with the organic cation of Py_{14}^+ decrease in intensity as the concentration of NaTFSI increases, namely the C-N stretching (1183 cm^{-1}), C-H bending (1465 cm^{-1}), and C-H stretching (2969 cm^{-1}). This agrees with EDX result in **Figure 5.2(a)**, where Na^+ from NaTFSI displaces the Py_{14}^+ in $Py_{14}TFSI$ as the salt concentration increases.

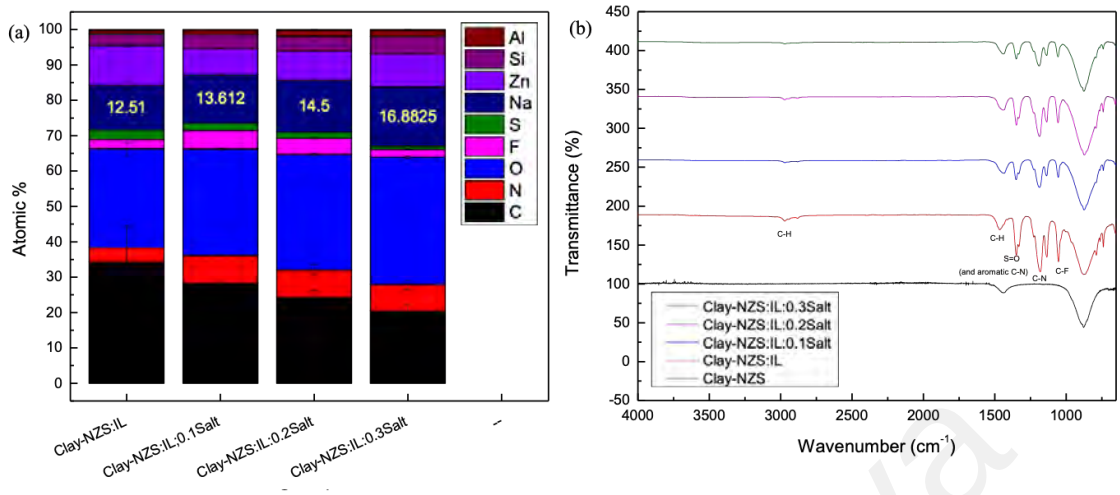

Figure 5.2: (a) Calculated atomic percentage from EDX measurements when Clay-NZS HybSSE is added with different concentrations of NaTFSI salt, i.e. 0 wt%, 10 wt%, 20 wt%, and 30 wt%, labelled as 0.XSalt, and (b) FTIR spectra of Clay-NZS HybSSE at different concentrations of NaTFSI salt. Peaks associated with the functional groups in the organic compound of IL is labelled on Clay-NZS:IL IR spectrum.

5.2 Ionic Conductivity and Activation Energy of Clay-NZS HybSSE

TGA was performed on both Clay-NZS SSE and Clay-NZS HybSSE to compare the samples' thermal stability, therefore the suitable operable temperatures for subsequent impedance measurements of the HybSSE. It is understood that while the ceramic is able to withstand a very high temperature elevation, $Py_{14}TFSI$ ionic liquid used in the fabrication of HybSSE has a theoretical boiling point of 486.65°C (Valderrama et al., 2012). **Figure 5.3** shows that besides the weight loss due to water at ~100°C for both samples, the pristine Clay-NZS ceramic is considered stable across the range of temperature selected, as expected. Meanwhile, Clay-NZS HybSSE experience a steep drop in weight (~25%) in the range of temperature between 300.0°C and 513.4°C. Because the amount of IL infused into the ceramic is around the same weight, this weight loss is therefore deduced to be the combustion of the infused IL solution from the HybSSE. Thus, it is pre-determined that the maximum operable temperature for Clay-NZS HybSSE is 300°C to preserve the IL solution in the sample, which is nevertheless a broad temperature window for practical use in SIB (Monti et al., 2014).

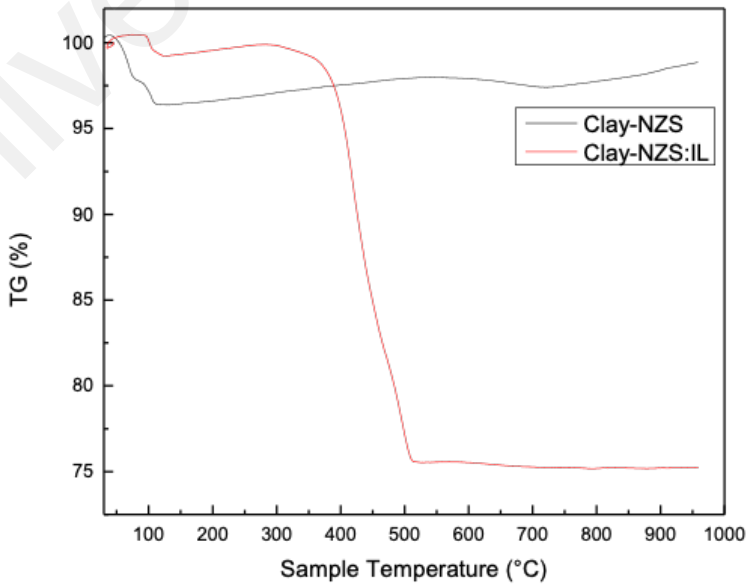

Figure 5.3: TG comparison between the final system of Clay-NZS and Clay-NZS HybSSE, indicating loss of weight in the HybSSE due to combustion of IL solution.

When the IL solution is infused into the ceramic pellet of Clay-NZS, it was found that the newly-formed HybSSE is capable of showcasing a decent ionic conductivity at temperatures as low as RT. The values obtained is as high as 2.3×10^{-5} S cm^{-1} at RT for Clay-NZS:IL:0.1Salt HybSSE. This is an astounding figure in contrast to the 8.74×10^{-9} S cm^{-1} ionic conductivity obtained by Pristine Clay-NZS SSE at its lowest operable temperature of 175°C, as discussed in **Section 4.4**. It is believed that the IL solution greatly enhances the conductivity at grain boundaries by wetting the ceramic, thereby overcoming the largest limitation in the pristine Clay-NZS SSE. Therefore, Clay-NZS HybSSE allows for a more practical application as opposed to its SSE counterpart. **Figure 5.4(a)** shows the Nyquist plot of Clay-NZS HybSSE across the range of salt concentrations at RT and **Figure 5.4(b)** at 300 °C. Clay-NZS HybSSE with no salt content in the IL solution is no longer considered in this section forward due to the absence of Na^+ in the liquid matrix of the HybSSE, making it unsuitable for SIB.

The equivalent circuit fitting the Nyquist plots is shown in the inset of **Figure 5.4** where all plots across NaTFSI concentration and across temperatures showed a consistent agreement to the circuit. This is the same circuit used for the fitting of the pristine NZS SSE samples in **Section 4.4**, yet their behaviours deviate slightly. First, unlike in Clay-NZS SSE, R1 component of the Randles circuit is relatively significant in the HybSSE, exhibited by the Nyquist data point not starting at zero. R1 is typically attributed to the electrolytic behaviour of a liquid, which in this case, is due to the IL solution. Next, the parallel RC circuit that showcases itself as a semicircle in the Nyquist plot is similar to the SSE, in the sense that there is only one semicircle visible. Nevertheless, it is much smaller compared to Clay-NZS SSE across all temperatures, which also explains why R1 is more prominent here. Nonetheless, the significantly smaller semicircle in HybSSE

compared to SSE means that the R_{gb} is greatly reduced when the IL solution is at play, improving the mobility of ions at grain boundaries.

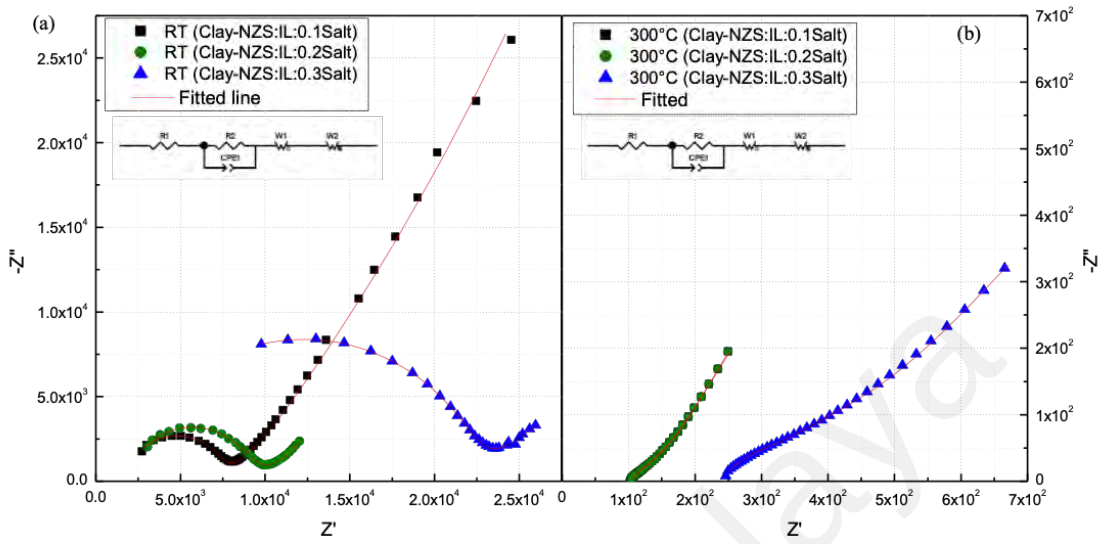

Figure 5.4: Nyquist plots of Clay-NZS HybSSE of different salt concentrations at (a) RT and (b) 300°C, with the results of Clay-NZS:IL:0.1Salt overlayed by Clay-NZS:IL:0.2Salt due to them having the same plots. Plots are fitted with equivalent circuits displayed inset.

In terms of the trend within the HybSSE, both R1 and R2 are observed to be bigger as the wt% of NaTFSI in the IL solution increase. This means that as the IL solution becomes more concentrated with NaTFSI and hence more viscous, the HybSSE becomes more resistive towards both ionic diffusion (represented by R1) and inter-grain ionic hopping (represented by R2), making it less conducting overall. The conductivities of the three samples across all temperatures are displayed in **Figure 5.5(a)**. The graph shows that the conductivities of Clay-NZS:IL:0.1Salt and Clay-NZS:IL:0.2Salt often times overlap within their uncertainty range, exhibiting similarity in value. Such result is also evident in **Figure 5.4(b)** where the Nyquist plots of the two samples at 300°C overlap each other. Meanwhile, Clay-NZS:IL:0.3Salt consistently exhibits the lowest conductivity value at all temperatures. This is in agreement with the understanding that ionic mobility is reduced with increased viscosity of IL solution, therefore reducing the overall conductivity (F. Chen et al., 2018). Therefore, it is deduced that only a minimal amount of NaTFSI is needed to generate Na^+ ions in the liquid matrix of the HybSSE, beyond which will hinder ionic conductivity due to the IL solution's increased viscosity.

Henceforth, a test was made by soaking a cell separator with the IL:0.1Salt solution and did EIS on it in a Swagelok-type cell to evaluate the impedance value of the IL solution itself as an electrolyte and compare it with the HybSSE samples. Interestingly, it was found that the IL solution has an RT ionic conductivity of approximately 1×10^{-5} S cm^{-1}, as shown in **Appendix A**. This conductivity value is well below the advertised conductivity of the Py_{14}TFSI IL without the NaTFSI salt, which is 2.76 mS cm^{-1}, according to its safety data sheet (SDS) (Solvionic, 2021). The difference between the SDS and the test value is attributed to the test being done with a separator, as would be the case in a commercial battery. Meanwhile, the conductivity quoted in the SDS is believed to be of the liquid as-is, without the separator, let alone a metal-ion salt. As such, it is believed that this test result is a better indication of how the IL solution would perform in a practical device, and to be Na^+ ion conducting, relevant for application in SIB. Thus, when comparing the ionic conductivity of the IL:0.1Salt solution with Clay-NZS:IL:0.1Salt HybSSE, the HybSSE has about double the ionic conductivity. Therefore, the synergy between the ceramic and IL in the HybSSE is deduced to be better than the synergy between the IL and a commercial separator.

When displayed in an Arrhenius plot as shown in **Figure 5.5(b-d)**, the activation energies of all samples are very similar to one another, which is ~0.22 eV. Therefore, it is difficult to comprehensively compare the electrical behaviour of these samples just by analysing their impedance values and activation energies only. Nevertheless, the ΔE_A value of Clay-NZS HybSSE, regardless of salt concentration in the IL solution, is much lower when compared to the pristine Clay-NZS SSE value of 0.71 eV, as discussed in **Section 4.4**. This means that there is lower energy barrier pertaining ionic conduction in Clay-NZS HybSSE in contrast to Clay-NZS SSE. Meanwhile, the IL solution itself is found to have ΔE_A value of 0.14 eV, which is expectedly lower than the HybSSE due to the fully-liquid nature of the IL solution electrolyte. Nevertheless, the ΔE_A value of the

HybSSE is closer to its standalone IL solution than its pristine ceramic SSE values, signifying the liquid-solid dynamic within the sample pellet.

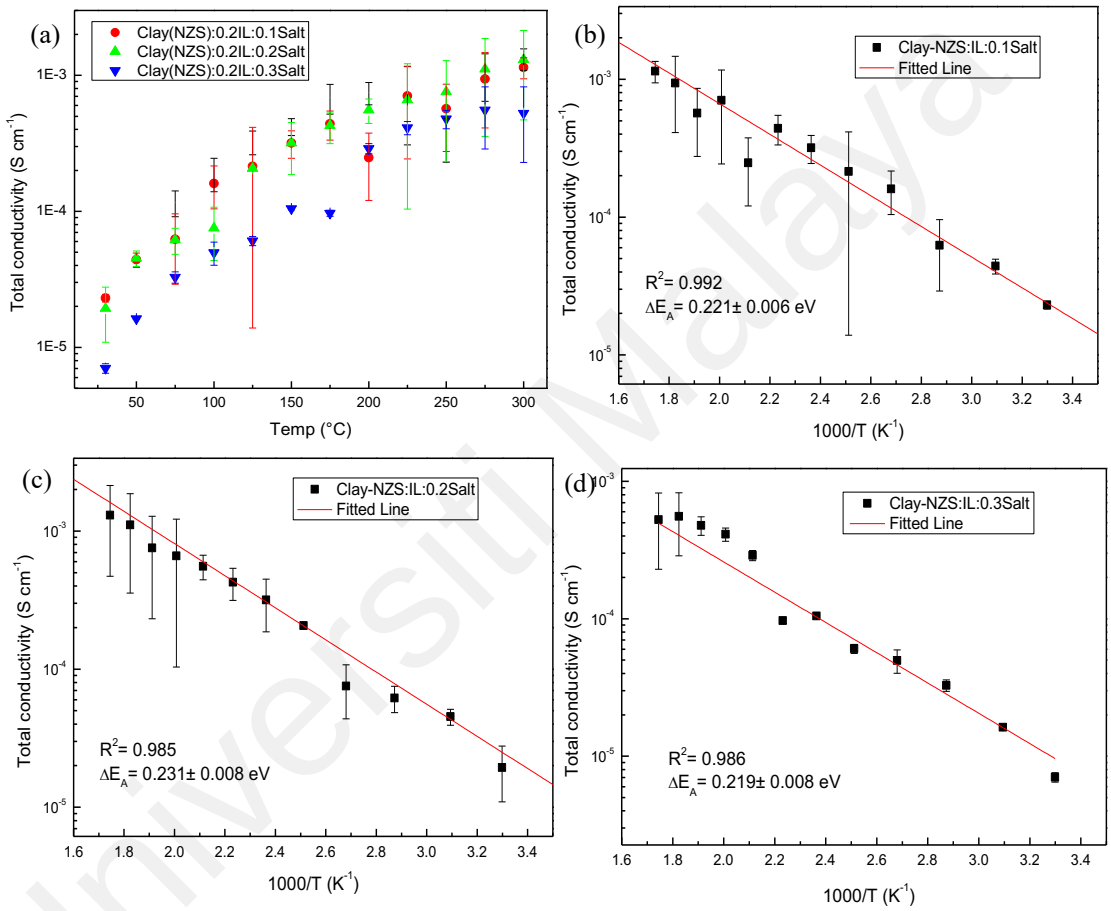

Figure 5.5: (a) Total conductivity of HSE across temperatures, (b) Arrhenius plots of Clay-NZS:IL:0.1Salt, (c) Clay-NZS:IL:0.2Salt, and (d) Clay-NZS:IL:0.3Salt.

5.3 Frequency-Dependent Ionic Conductivity of Clay-NZS HybSSE

In extension to the ionic conductivity analysis discussed in **Section 5.2**, the frequency-dependent conductivity of the three Clay-NZS HybSSE samples is assessed. It can be seen from **Figure 5.6(a-c)** where the trend in all three samples resemble one another. On the high-frequency region for all samples, the UDR curve is clearly recognised at RT but slowly diminish at temperatures above 100°C. This is unlike the typical polycrystalline behaviour where the UDR withholds across all temperatures (Ahmad, 2015; W.-X. Yuan & Li, 2012), signifying the consistency of ionic hopping mechanism in the sample. Thus, the diminishing UDR in the HybSSE as temperature increases equates to the fact that ionic conduction in HybSSE becomes lesser reliant on ionic hopping as temperature increases. Because the dielectric response measurement is antecedent in determining the conduction mechanism in a solid (Austin & Mott, 2017; Dhahri et al., 2018; Rahal et al., 2018; Rizwana et al., 2018), such displayed behaviour of the HybSSE samples can therefore be deduced that as temperature goes up, the ions in the HybSSE are no longer mobilised through hopping mechanism, but instead diffuses across the sample.

The latter argument on diffusion is further strengthened by the trend seen in the low-frequency region of all three samples. The tangent in the low-frequency region displays the diffusion and mass transport of ions within the electrolyte. This tangent is normally non-existent in a typical SSE, i.e., σ_{DC} persists at very low frequency. Instead, in HybSSE, the existence of this tangent is prominent. **Figures 5.6(a)** and **5.6(b)** show that the tangents due to diffusion in Clay-NZS:IL:0.1Salt and Clay-NZS:IL:0.2Salt are ramped up significantly at 100°C and remain high until 300°C. This confirms the argument that the ions in HybSSE are conducting mainly by way of ionic diffusion, instead of ionic hopping, especially at high temperatures. Meanwhile, **Figure 5.6(c)** shows that despite the UDR curve being absent in Clay-NZS:IL:0.3Salt, the diffusion gradient still remain low even when temperature goes up. It is therefore evident that at

this concentration of NaTFSI salt, where the IL solution is considered saturated, the mass transport of ion in the HybSSE is slowed down in overall.

Thus, while Clay-NZS:IL:0.1Salt and Clay-NZS:IL:0.2Salt showcase a behaviour unlike that of a dielectric, they are consistent with being a hybrid of liquid and solid. Clay-NZS:IL:0.3Salt on the other hand, has proven itself to be a poor-performing electrolyte.

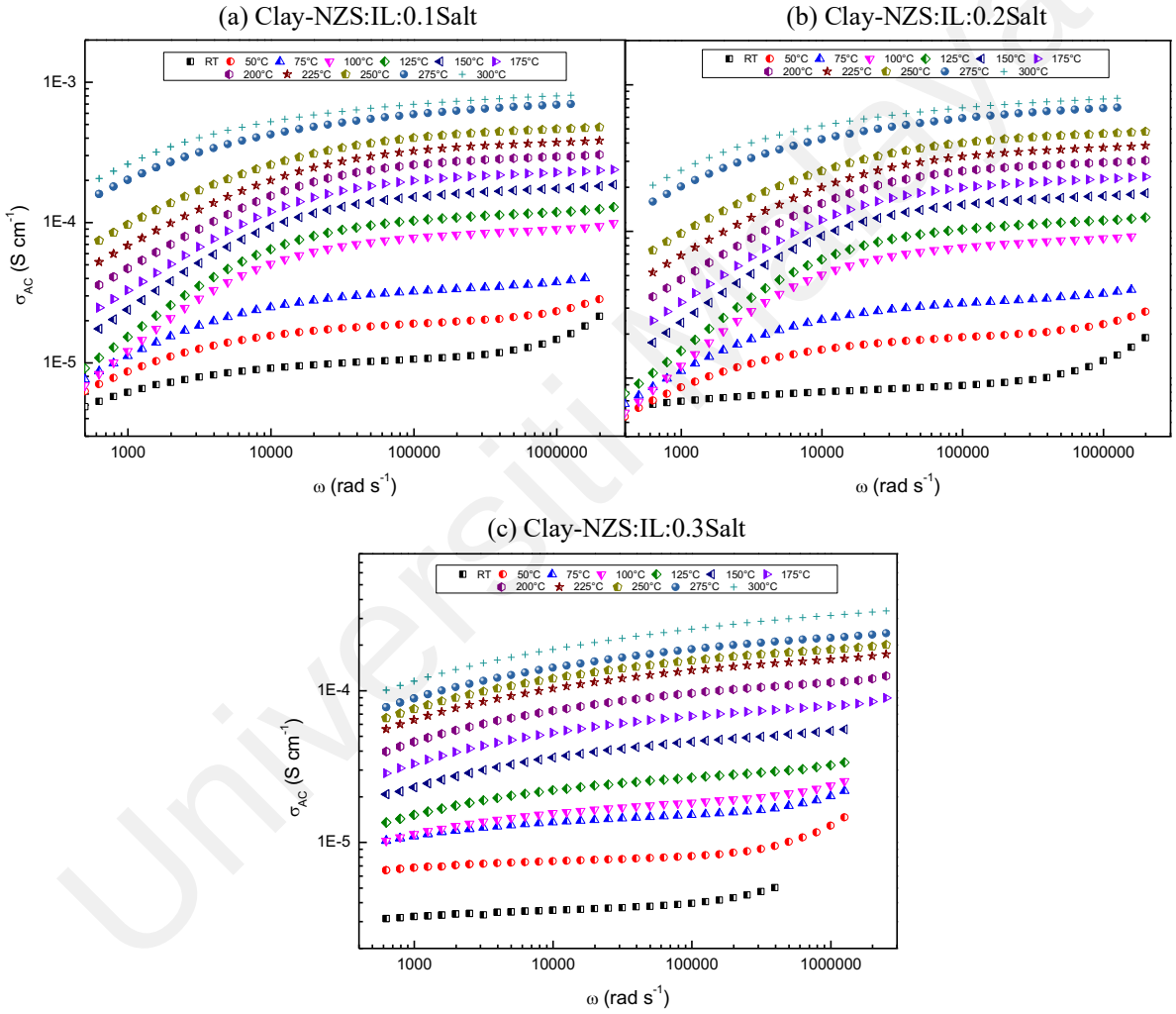

Figure 5.6: Frequency-dependent conductivity of Clay-NZS HybSSE with salt concentration at (a) 10 wt%, (b) 20 wt%, and (c) 30 wt%.

5.4 Ionic and Cationic Transference Number of Clay-NZS HybSSE

While the results from impedance measurements showed that making HybSSE out of Clay-NZS is the best way forward in terms of ionic conductivity, impedance analysis on its own is insufficient to determine the best composition of IL solution for Clay-NZS HybSSE. For this reason, their electrochemical characteristics are further probed to evaluate their other aspects of being an electrolyte. The ionic transference number of the three different Clay-NZS HybSSE samples are therefore investigated via Wagner's DC polarisation method. **Figure 5.7** shows the result of the chronoamperometry measurements done onto the samples and inset is the value of t_{ion} calculated using **Equation 2.9**.

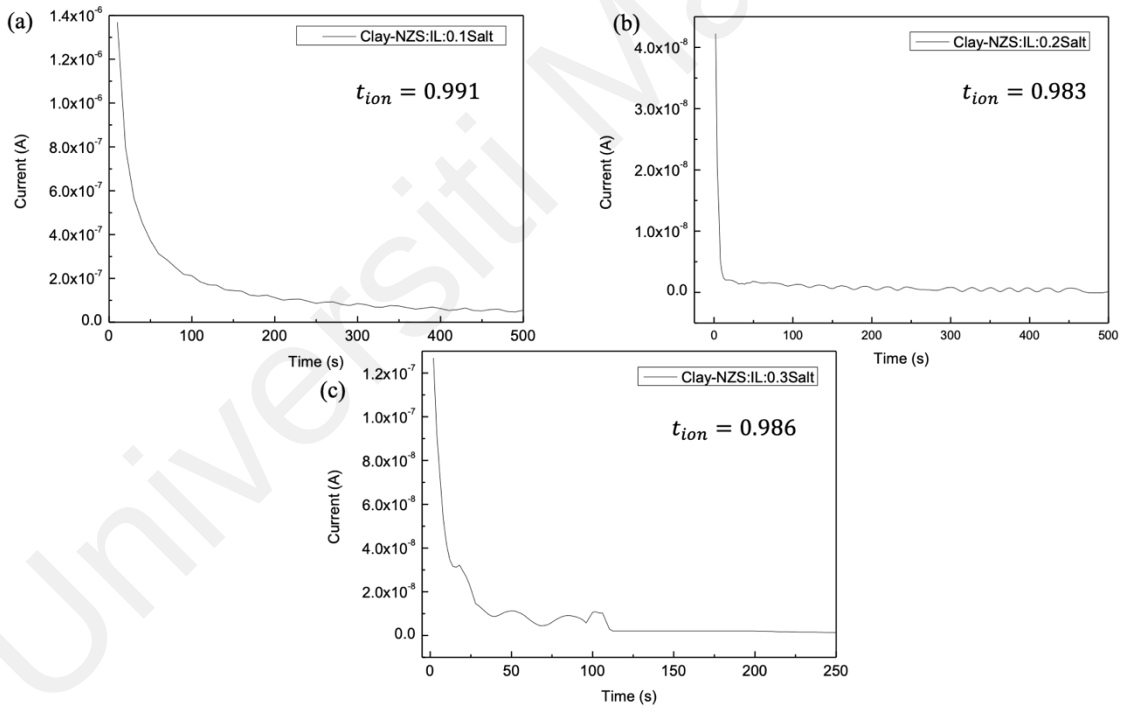

Figure 5.7: Chronoamperometry and total ionic transference number of Clay-NZS HybSSE with NaTFSI salt concentration of (a) 10 wt%, (b) 20 wt%, and (c) 30 wt%.

All three samples of Clay-NZS HybSSE give a t_{ion} value that are very close to unity, confirming that the charge transport in all samples are mainly due to ions and that the electronic contribution is negligible. Amongst the three samples, **Figure 5.7(a)** shows that Clay-NZS:IL:0.1Salt has the highest reliability of being a pure ionic compound,

where its t_{ion} is equivalent to 0.991. Another distinct observation is that the initial current of Clay-NZS:IL:0.1Salt is ~10^{-6} A, while others have initial current that are much lower. The instantaneous current measured upon exposure to electric field correlates back to the ionic conductivity of the samples through Ohm's Law. Lower instantaneous current shows slower current flow. As discussed in **Section 5.1**, the viscosity of the IL solution increased as the salt concentration increased. Since current is directly proportional to drift velocity ($I \propto v$) (Huggins, 2009), it can be deduced that the ions in a more concentrated IL solution move much slower across the electrolyte. This result agrees with the literature that states Py_{14}TFSI's high viscosity at RT negatively impacts its ionic conductivity, which is also reflected in the Clay-NZS HybSSE's ionic conductivity value, as discussed in **Section 5.2**. This subsequently leads to slower ionic transport (Monti et al., 2014; Tong et al., 2020). Paired with its high cost of material, this is the fundamental reason why Py_{14}TFSI-NaTFSI is seldom used as an electrolyte on its own. Therefore, it is crucial to ensure that when adding IL solution into an SSE to make a HybSSE, the viscosity of the IL solution is kept at a minimum. In this case, not only is Clay-NZS:IL:0.1Salt combination is the best sample for Clay-NZS HybSSE due to its t_{ion} value being closest to unity, but also because it shows the highest ionic transport.

Next, the samples' transference numbers due to Na^+ ion (t_+) were explored using the Bruce-Vincent method and calculated using **Equation 2.10**. Typically, a ceramic SSE would have $t_+ \approx t_{ion}$ because the mobile ions in a polycrystalline is just the alkali metal cations. The other cations and anions make up the rigid lattice framework which remain immobile under electric field. With the addition of IL solution to form Clay-NZS HybSSE, it is expected for $t_+ < t_{ion}$ due to the anionic contribution of mobile $TFSI^-$ ion moving freely within the pores of Clay-NZS ceramic. Therefore, isolating the transference number due to Na^+ of the whole system is bound to result in a lower figure. Previous studies of Na-ion IL electrolyte found that their standalone t_+ value ranges

around 0.3 (Forsyth et al., 2016; Isa et al., 2017). The significantly low value is very much attributed to the large molecular size of the anions in the IL. This is another reason why a full cell made up of IL electrolyte is undesirable.

Figure 5.8 shows that Clay-NZS HybSSE in general have t_+ values that are comparable, if not higher than its corresponding standalone IL solution electrolyte. It is therefore deduced that the ceramic component of Clay-NZS also plays a role in contributing mobile Na^+ to the system, thus increasing the overall Na^+ concentration at play. **Figure 5.8(a)** shows that the t_+ value reduces when the concentration of NaTFSI in the IL solution increase from 10 wt% to 20 wt%, but goes back up at 30 wt%. While this may be peculiar and out of trend, recent studies showed that "super-concentrated" IL solution can exhibit higher cation (Na^+/Li^+) transport than solutions with lower salt concentrations (F. Chen et al., 2018; Tong et al., 2020). Even so, in this experiment, the t_+ value of Clay-NZS:IL:0.3Salt is not as high as Clay-NZS:IL:0.1Salt, which is 0.506. Paired with other results in previous sections, the Clay-NZS:IL:0.1Salt is therefore established to be the best composition to form Clay-NZS HybSSE.

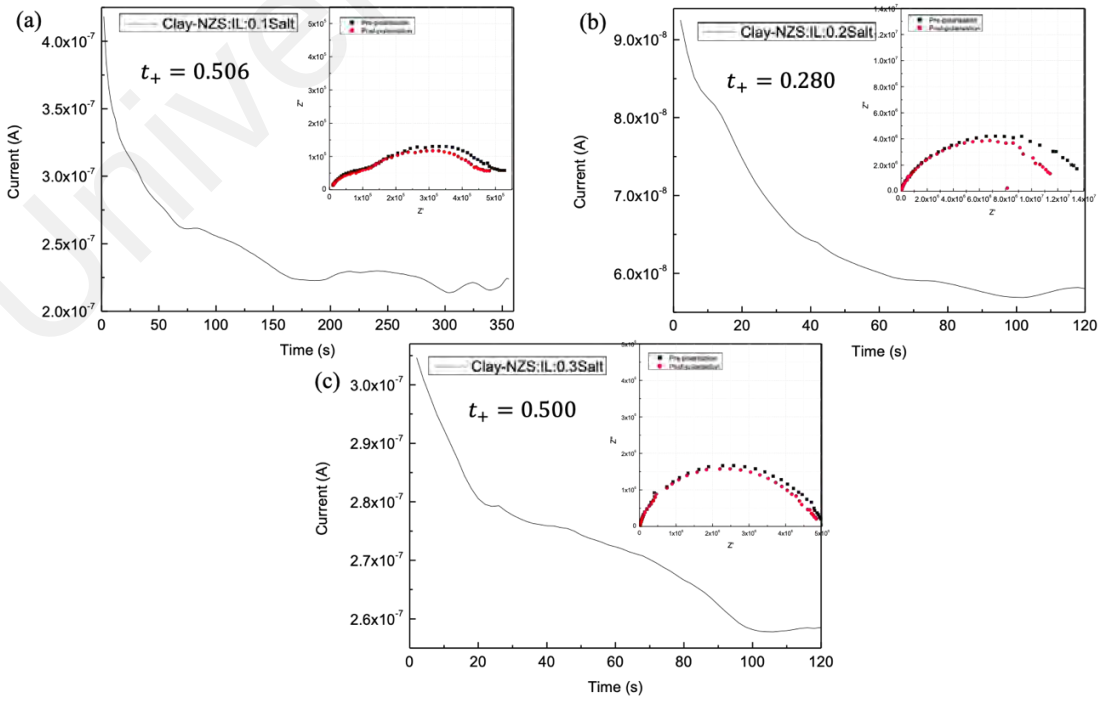

Figure 5.8: Na-ion transference number of Clay-NZS HybSSE with NaTFSI salt concentration of (a) 10 wt%, (b) 20 wt%, and (c) 30 wt%. Insets are the Nyquist plots from pre-polarisation (black) and post-polarisation (red).

5.5 Electrochemical Stability of Clay-NZS HybSSE

LSV measurements using two blocking electrodes were taken on all three HybSSE samples to evaluate their ESW, shown in **Figure 5.9**. It was found that despite the experiment being executed with the same parameters, current collected by the sample decreases tremendously with increasing salt concentration in the IL solution, in agreement with the results discussed in earlier sections. Amongst all, Clay-NZS:IL:0.1Salt showcase the most reliable voltammetry data and exhibits ESW of up to 4.32 V. Meanwhile, Clay-NZS:IL:0.3Salt and Clay-NZS:IL:0.2Salt have current signals that are very close to the equipment noise, indicating near-zero current flow even at high potential. Even though separately Clay-NZS:IL:0.3Salt has an ESW that is deemed to be the highest at 4.66 V as shown inset of **Figure 5.9**, its low current indicates that it might be too resistive to conduct below its decomposition potential. On the other hand, Clay-NZS:IL:0.2Salt has the lowest ESW of only up to 3.90 V. Therefore, time and again the experimental data show that the Clay-NZS:IL:0.1Salt is the best composition for Clay-NZS HybSSE.

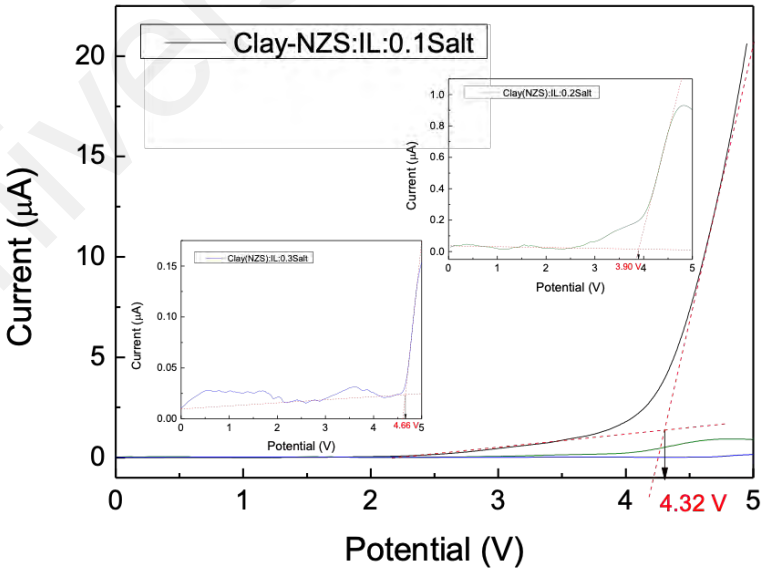

Figure 5.9: LSV of Clay-NZS HybSSE to determine ESW of the samples.

Henceforth, based on the results discussed in the preceding sections above, the half-cell CV test to evaluate the system's cyclability and stability against Na metal was done on Clay-NZS:IL:0.1Salt as the chosen sample for Clay-NZS HybSSE. The voltammetry data is shown in **Figure 5.10**. In **Figure 5.10(a)**, where oxidation and reduction peaks are observed at 2.42 V and 2.19 V versus Na/Na^+, respectively. These peaks correspond to the Mn^{4+}/Mn^{3+} redox couple in the composite electrode (Do et al., 2019). The oxidation peaks are not very visible due to the fast scanning rate selected. Fast scanning is employed to minimise the formation of passivation layer when the sample is in contact with Na-metal (Lou et al., 2021), which is evident in the few cycles ran, yet allowing us to confirm the cyclability of the sample within the ESW. Meanwhile, **Figure 5.10(b)** shows that the current across the half-cell is reduced with every cycle of triangular potential waveform. This means that like a lot of other Na-ion electrolyte candidates, Clay-NZS HybSSE is not exempted from instability against Na-metal (Ferdousi et al., 2021; Makhlooghiazad et al., 2017). Nonetheless, the curves indicate reversibility of charge transfer across the sample, posing Clay-NZS HybSSE as a viable candidate for rechargeable battery. To overcome the instability issue, a different anode needs to be selected for future works of this material in perfecting it for Na-ion battery application.

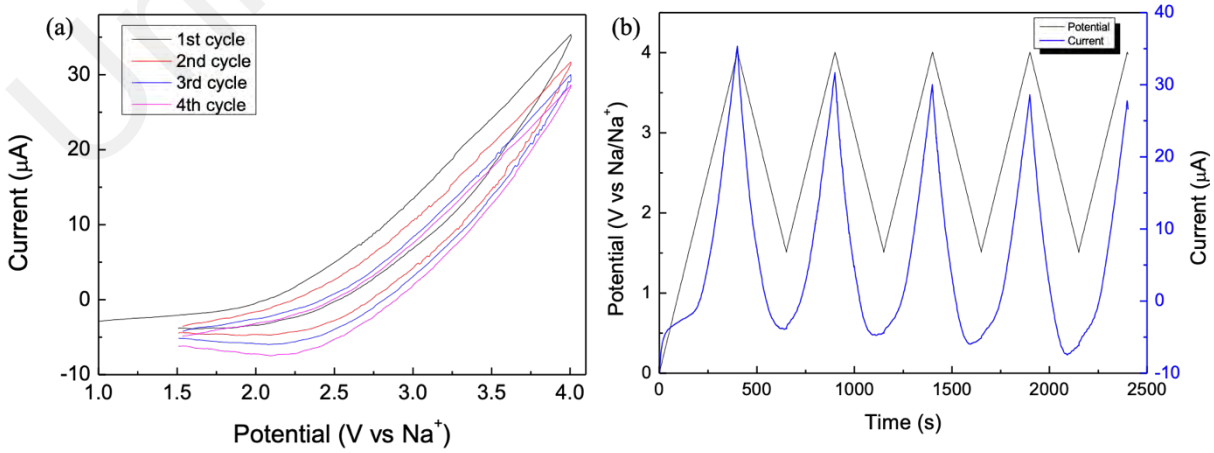

Figure 5.10: CV of Clay-NZS HybSSE plotted at (a) current against potential, and (b) potential & current against time.

CHAPTER 6: ENHANCEMENTS OF CLAY-NZS HYBSSE IN HIGH THROUGHPUT

6.1 Synthesis Optimisation of Clay-NZS HybSSE

The procedures employed to synthesise Clay-NZS in the traditional sol-gel method discussed in **Section 4.2** was adapted into a high-throughput setup to further optimise the ceramic. This is in efforts to maximise the performance potential of Clay-NZS HybSSE as an electrolyte in SIB. **Figure 6.1** shows the key results obtained from this optimisation work while **Appendix B-D** show the compilation of selected XRD patterns done on Clay-NZS out of >350 samples processed.

6.1.1 Modification of Heating Steps

One of the modifications made in the new synthesis process was adding an extra heat treatment step at 550°C. The sample powder after being calcined at 350°C turned out to be black, indicating large presence of carbon. Based on the TGA-DSC data shown in **Figure 4.4(a)** in **Section 4.2**, there is an additional mass loss of Δm_2 between 518.7°C and 750.0°C, which means there are some residual compounds that are combusted in this range of temperature before crystallisation occur. It was found that the pre-sintering step done on the sample powder at 550°C gave out a white powder, indicating that carbon has been fully burnt off at this stage. Thus, the powder is pressed into pellets after this step and subsequently sintered. This modification in step eliminates the possible formation of pores due to carbon loss during sintering and thus ensuring a denser pellet. Upon crystallisation, the sintering temperature was configured accordingly as below.

It was found that when the starting reagents of Clay-NZS were mixed in stoichiometric amounts in the high-throughput set-up, the sample pellets were speckled with blueish-grey particles when sintered at 750°C and 850°C, as shown on the left side of **Figure**

6.1(a). This was not observed previously in the synthesis works done in Chapter 4. The blueish-grey speckles showcase the enhanced presence of coesite, a type of SiO_2 normally obtained when treated with high pressure and prolonged high temperatures (Bohlen & Boettcher, 1982), confirmed by the samples' phase compositions shown in **Figure 6.1(b)**. When the sintering time at these temperatures was increased from 6 h to 10 h, no structural change was observed, and the phase composition remained. This shows that at these

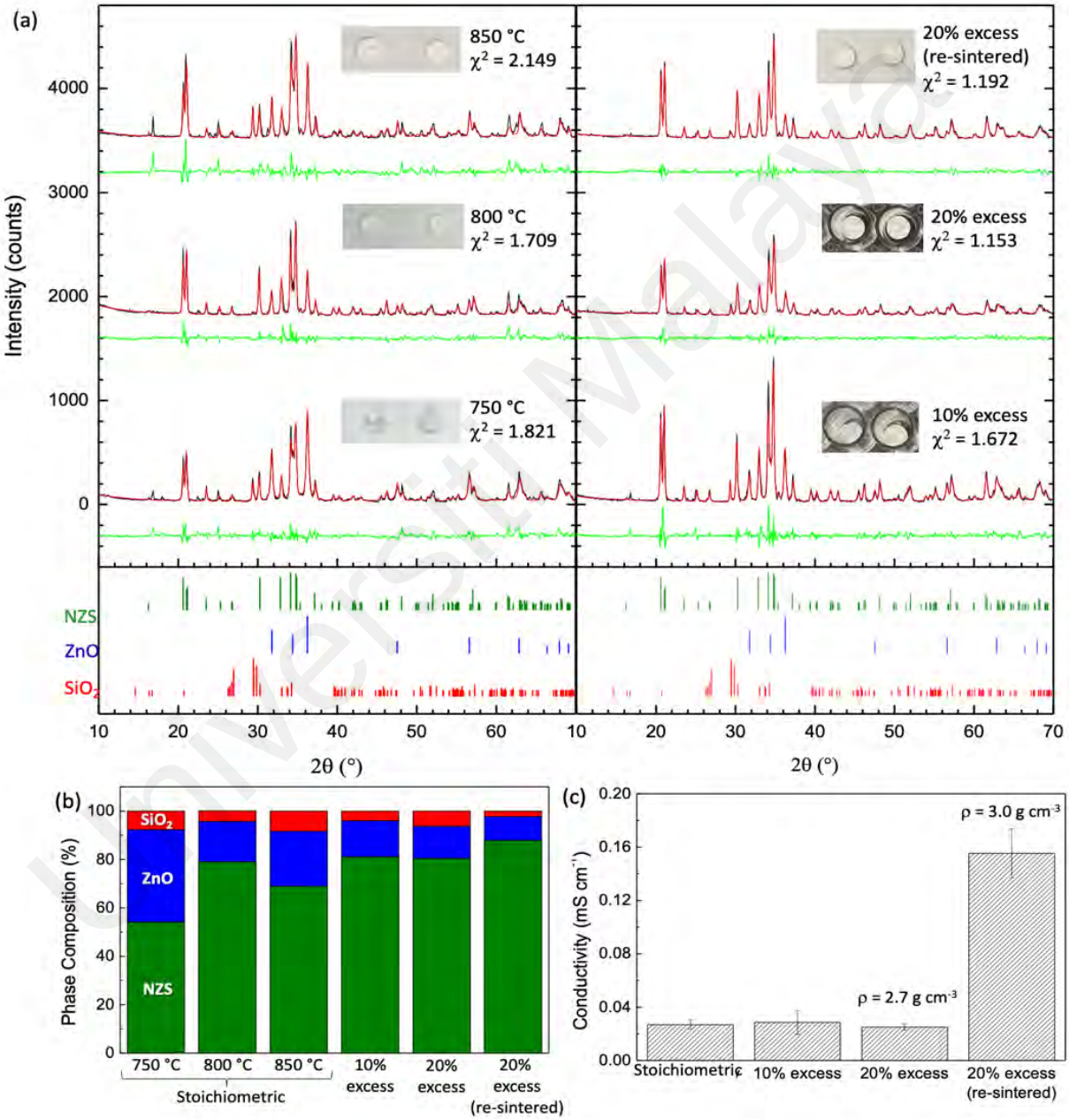

Figure 6.1: (a) Refined XRD patterns of six variations of the synthesis of NZS, where the black line is the experimental spectra, red is the calculated spectra based on the theoretical peaks of the phases, and green is the difference between the experimental and calculated spectra. Inset is the appearance of the sample pellet, (b) Calculated phase compositions of the corresponding six synthesis variations after undergoing Rietveld refinement, and (c) Ionic conductivity of NZS HybSSE at selected four synthesis variations, where ρ is the density of the pristine pellet.

temperatures, regardless of treatment period, a portion of the SiNP remain in the compound as SiO_2, albeit in coesite form, rather than being integrated into the intended NZS phase. This might have been brought about by poor mixing of SiNP into the sol due to the micro-scale of the solution made to suit the high-throughput setup.

On the other hand, pellets sintered at 800°C were physically white, as seen in the middle picture on the left of **Figure 6(a)**. Structurally, this corresponded to the smallest presence of coesite, confirmed by the results shown in **Figure 6.1(b)** where the highest composition of NZS was found in the samples sintered at 800°C, amongst the samples synthesized at stoichiometric composition. Furthermore, its Rietveld refinement exhibits the best χ^2 value amongst the three sintering temperature variations, as shown by the right side of **Figure 6.1(a)**. Since NZS is the primary phase of interest, it is therefore concluded that 800°C is the right sintering temperature for the synthesis of Clay-NZS in high-throughput.

6.1.2 Modification of SiNP Volume as Starting Reagent

Another synthesis step that was revisited in the high-throughput lab was the amount of SiNP used as starting reagent. The XRF data shown in **Table 4.1** in **Section 4.1** demonstrated the presence of impurities in the harvested SiNP after the acid treatment. Therefore, it was later inferred that perhaps SiNP has a molar weight that is more than the standard SiO_2. Thereafter, it was investigated to use SiNP in excess during synthesis, while maintaining the sintering temperature at 800°C. It was found that although the samples' phase compositions do not differ very much, the XRD spectra were found to be much better refined when the SiNP were at 20% excess, with χ^2 being consistently close to 1, as demonstrated by the right side of **Figure 6.1(a)**. This indicates a better fit to the reference patterns, compared to being previously assumed that SiNP have the same molar

weight as SiO_2. Henceforth, the synthesis of Clay-NZS in high-throughput includes using SiNP at 20% excess, while being sintered at 800°C.

When Clay-NZS was eventually synthesised using the above optimised parameters in the high-throughput set-up, **Figure 6.1(c)** shows that the density of the pellets was determined to be 2.68(6) g cm^{-3}. When the sample's phase compositions was taken into account, this value equates to ~79.5% of the compound's theoretical density, where calculation was done using **Equation 3.7** (Persson, 2014c, 2014a, 2014b). Moreover, the resultant Clay-NZS HybSSE upon infusion of IL solution has an RT ionic conductivity of 0.03(1) mS cm^{-1}. This conductivity value is a small increase from when the sample was synthesised traditionally, as discussed is **Section 5.2**.

6.1.3 The Double Sintering Method

Afterwards, the packing of particles in the ceramic pellet was enhanced to potentially boost the sample's properties further. This was achieved by grinding the sintered pellets into powder and subsequently re-pressed and re-sintered. This extra step was called the double sintering method. Although this additional step sounds simple, it was found that the resultant sample displayed superiority in all measured aspects.

Firstly, the percentage of NZS phase in the sample increased tremendously, further eliminating other secondary phases. As shown in **Figure 6.1(b)**, the sample that was double sintered has the highest concentration of the NZS phase. Secondly, the density of the sample pellets increased to 3.00(8) g cm^{-3}, equating to ~89.6% of the theoretical density. This denotes over 12% increase in packing compared to when the pellet was only sintered once. Thirdly, the pellets produced through this method were seen to be more robust and easier to handle without cracking or flaking. Finally, the double sintering method was found to elevate the ionic conductivity of Clay-NZS HybSSE to an impressive value of 0.16(6) mS cm^{-1} at RT. This is an increase of more than fivefold

compared to when the ceramic was only sintered once, as shown in **Figure 6.1(c)**. This improvement is in fact an increase of seven times when compared to the original ionic conductivity of Clay-NZS HybSSE when synthesised via the traditional sol-gel method, which gathered RT conductivity of 2.3×10^{-5} S cm^{-1}, as discussed in **Section 5.2**.

All these significant improvements were accomplished after extensive optimisation works were done solely on the ceramic compound of the HybSSE. This result presents clear evidence that the properties of the ceramic host play a pivotal role in determining the overall ionic conductivity of Clay-NZS HybSSE. All other parameters explored are included in **Appendix B-E**, however, none of these parameters had any significant impact on the material's properties. It is therefore concluded that the high-throughput optimisation of Clay-NZS samples increased the ceramic density by about 10%, the phase fraction of NZS by about 10%, and the ionic conductivity of the optimised Clay-NZS HybSSE by nearly an order of magnitude.

6.2 Microstructure of Optimised Clay-NZS HybSSE

Figure 6.2 shows FESEM images captured of the pristine Clay-NZS pellets after the synthesis methods have been optimised in high-throughput. **Figures 6.2(a-b)** showcase the surface of the pristine Clay-NZS ceramic, magnified at different area. While **Figure 4.6(a)** shown in **Section 4.2** exhibited that all the grains present in the Clay-NZS ceramic are nanosized, optimised Clay-NZS shown in **Figures 6.2(a-b)** have a mixture of nanoparticles and large micro-scaled particles. It is likely that the double sintering process encourages crystal growth, thus the variety in particle sizes. Consequently, this allows for better packing of grains, resulting in the tremendous increase in density of the pellet.

Nevertheless, the nanosized particles are still evident in the optimised Clay-NZS sample, where EDX measurements of the nanoparticulate area indicated its Zn:Si ratio to be 1.5:1. It is therefore deduced that these nanoparticles are the particles of Na_2ZnSiO_4. However, the relatively large rod-shaped particles occupying the top right image of **Figure 6.2(a)** were previously not found in **Figure 4.6(a)**. Instead, the rod-shaped particles were also nanosized. EDX measurements showed that these rods are Zn-rich, i.e., Zn:Si ratio of 2.9:1. Judging by the apparent triangular and hexagonal cross-section of these sticks, paired with its Zn-rich EDX profile, it is unmistakable that these large sticks are ZnO since it is the only phase present that has a hexagonal crystal structure. It is probable that the additional double-sintering step has caused the ZnO crystals to grow larger than usual, despite the phase fraction decreasing slightly.

Therefore, it is deduced that the enhanced ionic conductivity of the double-sintered Clay-NZS HybSSE discussed in the previous section is not only caused by the reduction

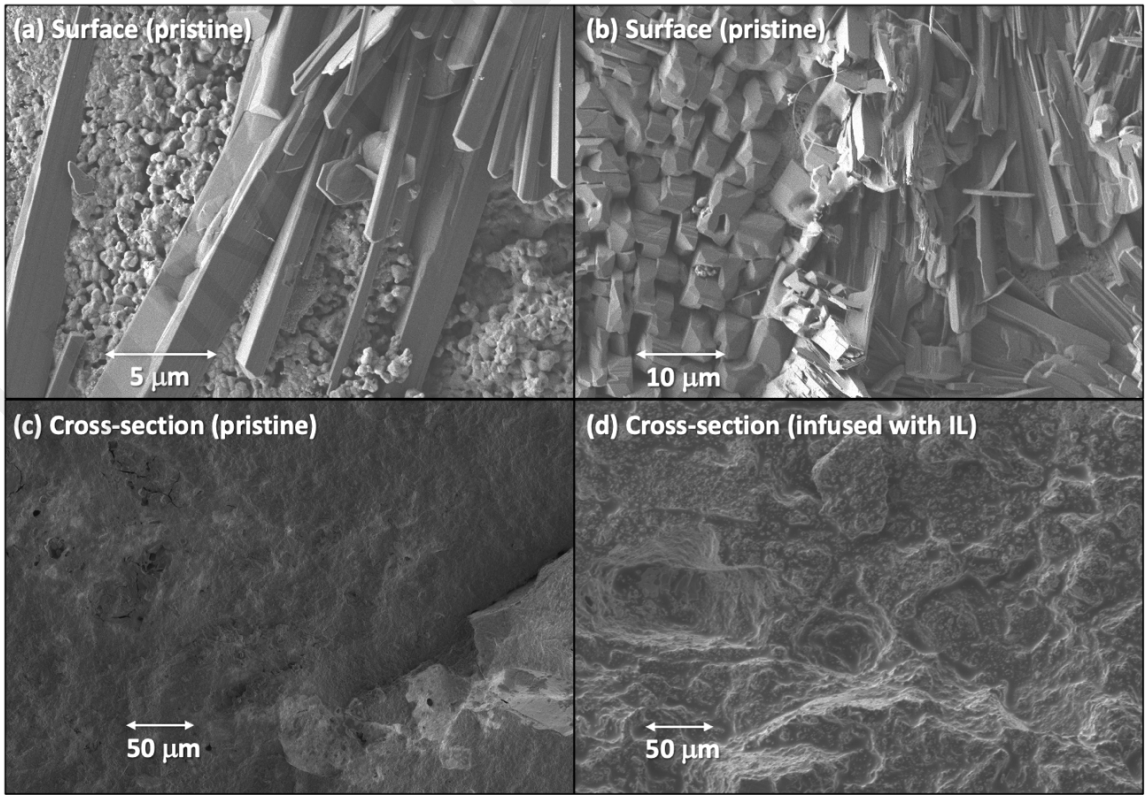

Figure 6.2: Micrographs of sample pellets at (a-b) surfaces of the pristine NZS ceramic, (c) cross-section of the pristine NZS ceramic, and (d) cross-section of NZS HybSSE infused with ionic liquid solution.

in grain-boundary resistance due to better packing and nanoionic phenomena (J. Maier, 2005; Joachim Maier, 2014; H. Wan et al., 2019), but also due to the diminished grain boundaries in the grown crystals of ZnO phase. **Figure 6.2(c)** shows how densely packed the particles are through the cross-section of the pristine sample pellet. Meanwhile, **Figure 6.2(d)** shows how the IL solution can still fill up the pores and crevices in the now-denser optimised Clay-NZS pellet, much like how it was thoroughly infused in Chapter 5. It is believed that the infusion further minimizes the resistance due to grain boundaries, giving the HybSSE a higher ionic conductivity.

6.3 Blanket Elemental Substitution of Clay-NZS HybSSE

The possibility of further increasing the ionic conductivity of the optimised Clay-NZS HybSSE was investigated by way of a blanket elemental substitutions done on the Clay-NZS ceramic. The overall general stoichiometry of the Clay-NZS ceramic was determined to be $Na_2Zn_{1-x}Si_{1-x}A_{2x}O_4$ (where A is the substituent), doped with a wide array of substituent elements. From here on, these HybSSE samples that underwent substitution in its ceramic host are denoted as A_x (e.g., $In_{0.05}$ represents the sample made of A = In and x = 0.05). High-throughput screening allowed for the study of all 22 substituents to be done at $x = 0.025, 0.05,$ and 0.1.

6.3.1 Density of Sample Pellets and Infusion of IL Solution

Table 6.1 shows the physical properties of selected sample pellets before and after the addition of the IL solution. While the double sintering method afforded the undoped Clay-NZS ceramic a significant increase in relative density, doping the ceramic (as well as double-sintering them) showed little effect to the sample's relative density. Even so, the mass loading of IL solution was found to increase as the relative density of the samples

decrease, indicating that slow soaking the sample pellet with the IL solution allow for thorough filling of the pores of the pellet, regardless of its density.

Table 6.1: Physical properties of sample pellets before and after the infusion of IL solution. Density of the pristine ceramic pellets were initially recorded; Relative density of pellets were calculated using their theoretical densities based on phase compositions from XRD; Pellet volume is the volume of pristine ceramic pellets; Mass gain is the % mass change of sample pellets after the infusion of IL solution.

Ceramic sample pellet	Density (g/cm^3)	Relative density (%)	Volume (mm^3)	Mass gain upon infusion of IL solution (%)
Undoped (single)	2.7	80	35.9	11.3
Undoped (double)	3.0	89	35.3	6.2
$Fe_{0.1}$	2.9	85	29.3	6.0
$In_{0.1}$	3.0	87	27.7	9.5

Given that the IL solution has a density of about 1.5 g/mL (1.39 g/mL without the salt), even the lowest mass gain of 6.0% in the $Fe_{0.1}$ sample corresponds to a volume fraction of 14%. This implies that the 85% dense $Fe_{0.1}$ ceramic was very nearly fully filled with IL, which is ~99% total pellet volume. The total volume of ceramic + IL solution of sample pellets were calculated to be 99 – 104%. Therefore, it is considered that the ceramic hosts were all fully filled with IL solution in the slow-soaking method employed, giving confidence that the results obtained in subsequent subsections are due to the liquid-solid dynamics in the HybSSE. **Appendix F** shows the FESEM images of selected samples after the ceramic hosts were infused with IL solution to become HybSSE.

6.3.2 Conductivity Screening

The observed Nyquist plots of the doped Clay-NZS HybSSE sample pellets and their calculated ionic conductivities at RT for $x = 0.1$ are shown in **Figure 6.3**. Results are shown following the substituent's position in the periodic table to ease visualisation. The resulting ionic conductivities of doped Clay-NZS HybSSE range from as low as 0.003 mS cm^{-1} in the Mo-substituted sample, to as high as 0.453 mS cm^{-1} in the In-substituted sample. The undoped Clay-NZS HybSSE ionic conductivity value fell on the mid-range, indicated by the yellow box labelled "Zn". From the figure, there is no apparent trend along the periodic table to signify why substituting the compound with certain elements resulted in either a higher ionic conductivity or lower. Activation energy was then calculated using the ionic conductivity values at RT and 48°C and the results are shown in **Figure 6.4(a)**. The heat maps in **Figures 6.3** and **6.4(a)** are observed to be different from one another, showing the need to extract both conductivity and activation energy.

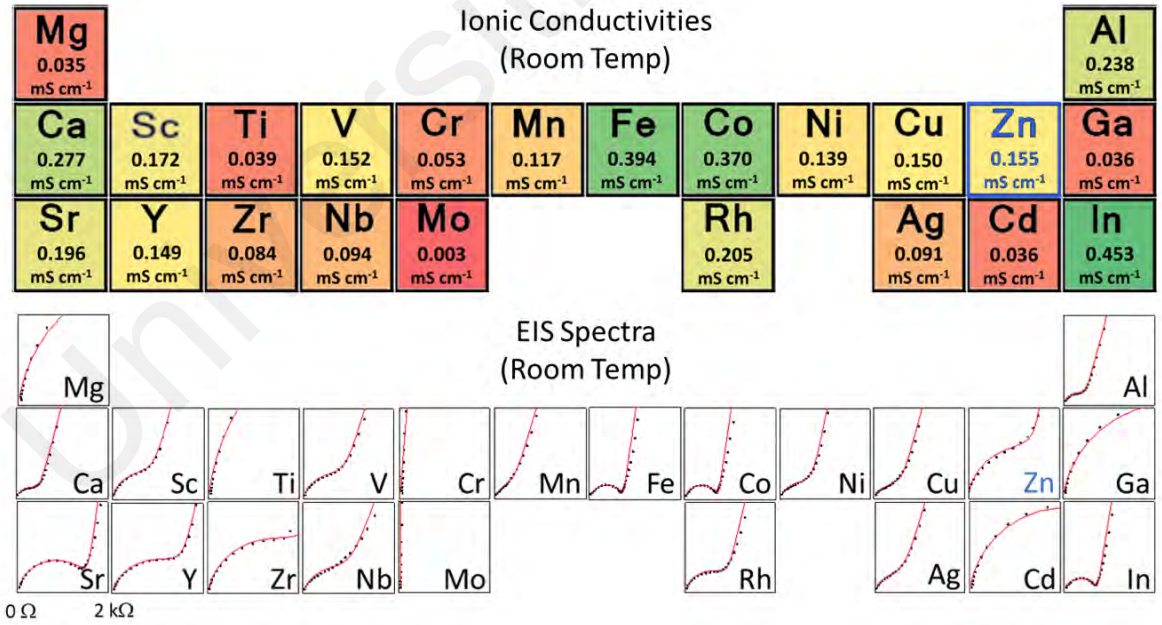

Figure 6.3: Ionic conductivities of 22 substituents of NZS when x = 0.1, recorded at room temperature (top) and the EIS spectra (Z as a function of Z') used to extract the conductivites (bottom). In both cases, plots are arranged according to the substituents' positions on the periodic table. The box colors correspond to a heat map for ionic conductivity: dark green indicates the highest conductivity value while dark red indicates the lowest. Zn is bolded in blue to show the unsubstituted value. The boxes of Nyquist plots all show Z and Z' values ranging from 0-2 kΩ.

Moreover, zero correspondence of the heat maps is also observed in the electronic conductivities of these samples, as shown in **Figure 6.4(b)**. Nevertheless, all the HybSSE samples recorded electronic conductivities of <2 nS cm^{-1}, indicating negligible electronic conductivities in all substituted and unsubstituted samples. This is well below the established threshold where dendrite formation becomes an important concern (Jonderian et al., 2021; Lou et al., 2021), which makes them all suitable for electrolytic purposes. Considering both **Figures 6.3** and **6.4**, it is clear that substituents that improve ionic conductivity with no detriment to electronic conductivity are Ca, Al, Sr, Fe, Co, and In.

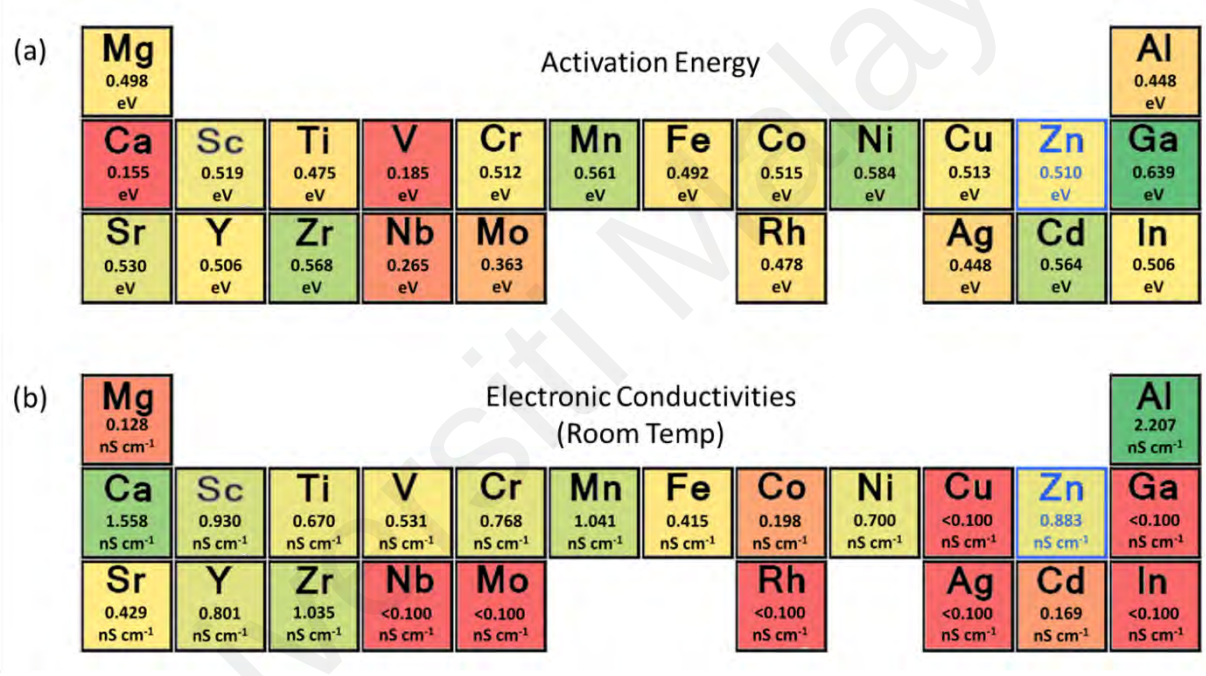

Figure 6.4: (a) Activation energy values of 22 substituents of NZS, based on ionic conductivities recorded at RT and 48°C, and (b) Electrical conductivities of the substituents, recorded at RT. All boxes are coloured as heat maps with red being low values and green being high.

6.4 Targeted Elemental Substitution of Clay-NZS HybSSE

Based on the results discussed in **Section 6.3**, additional investigations were done on the three substituents that increased the ionic conductivity values of Clay-NZS HybSSE the most, i.e., In, Fe, and Co. These substituents were studied in more detail by expanding the range of *x* in the stoichiometry up to 0.5 at regular intervals.

6.4.1 Structural Characterisation

Refinement of the XRD patterns of doped Clay-NZS show that all three substituents formed additional two secondary phases on top of the primary three (NZS, ZnO, and SiO_2), adding new components into the composite ceramic. This is extensively demonstrated in **Figure 6.5**, where all the collected XRD patterns are shown alongside their χ^2 values. The spectra lines in green show the best data for each of the three substituents. In addition to that, **Figure 6.6** shows phase composition and unit cell volumes extracted by performing Rietveld refinement on the patterns in **Figure 6.5**.

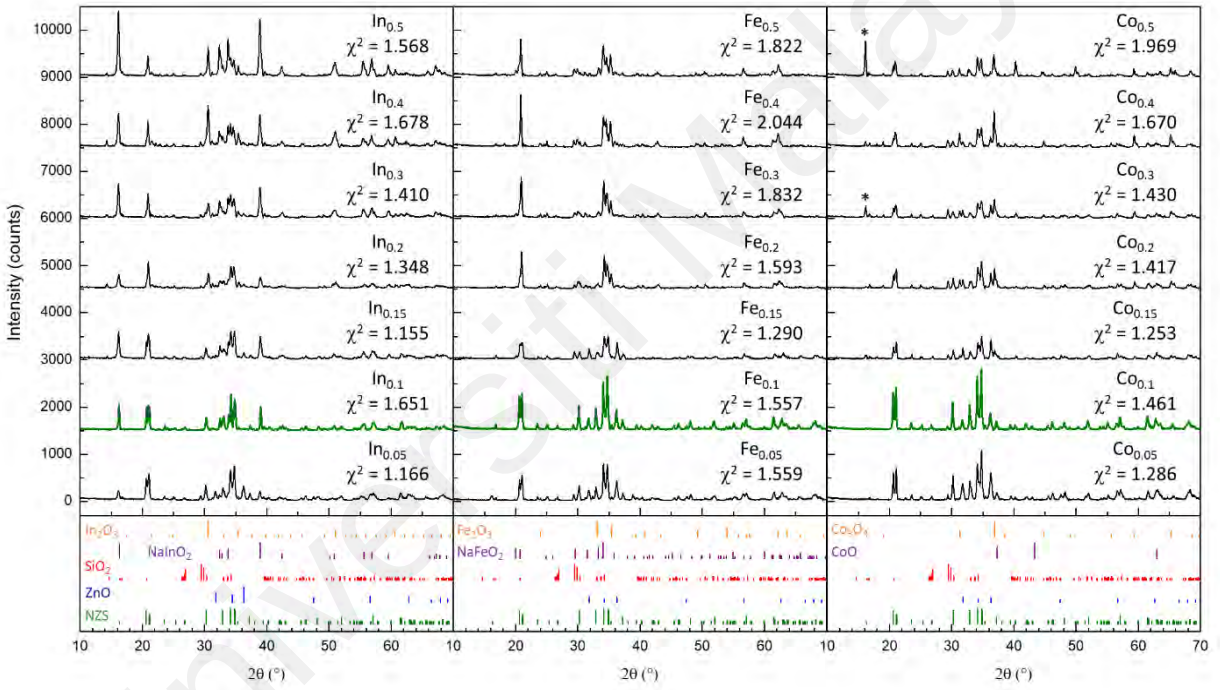

Figure 6.5: Refined XRD patterns of NZS substituted with In, Fe, and Co, at x = 0.05, 0.1, 0.15, 0.2, 0.3, 0.4, and 0.5. The multi-coloured reference patterns show the different phases in the sample, and the patterns bolded in green are the composition that has highest ionic conductivity.

All XRD patterns in **Figure 6.5** yielded small χ^2 fit values, demonstrating good agreement with the selected reference patterns, except for $Co_{0.3}$ and $Co_{0.5}$ where an unidentified peak was found at a scattering angle of 16°. Henceforth, the phase study for these compositions of Co-substituted samples is excluded from **Figure 6.6**. Meanwhile, for In-substituted and Fe-substituted samples, the most significant evolution in the XRD pattern as *x* increase is the increased intensity of the $NaInO_2$ and $NaFeO_2$ peaks,

respectively. Since the colour-scheme in **Figure 6.6** corresponds to the phases listed in **Figure 6.5**, the increase in phase fractions of $NaInO_2$ and $NaFeO_2$ can be seen in **Figure 6.6**, both represented by the purple-coloured bar.

Moreover, across *x* values for all three substituents, the unit cell volumes of all three primary phases increased from those in the original Clay-NZS, as shown in **Figure 6.6** and **Appendix G-I**. Even so, the rate of increase in the lattice volumes do not correlate to the incremental increase of the substituents, suggesting that the saturation of substitution into each of the primary phases may occur even in the $x = 0.05$ samples. It is important to recognize that these samples lie in a pseudoquaternary system and involve multiple phases such that the further addition of dopant does not necessarily lead to a linear change in lattice parameters. Instead, it is possible to simply change the fraction of phases present while co-existing to the same doped NZS composition. Nonetheless, the changes in lattice parameters do show that structurally, when new elements are introduced into the sample, it not only gave rise to new phases, but the elements are also doped into the primary phases, causing the lattices to expand. This makes further refinements impossible, i.e., we cannot constrain a fit of 4 phases when the substituent is present in all 4 phases.

It is also worthy to note that the In-substituted pellets remain white while those of Fe and Co turn quite dark, which may indicate reduced band gaps that could lead to reduced stability windows.

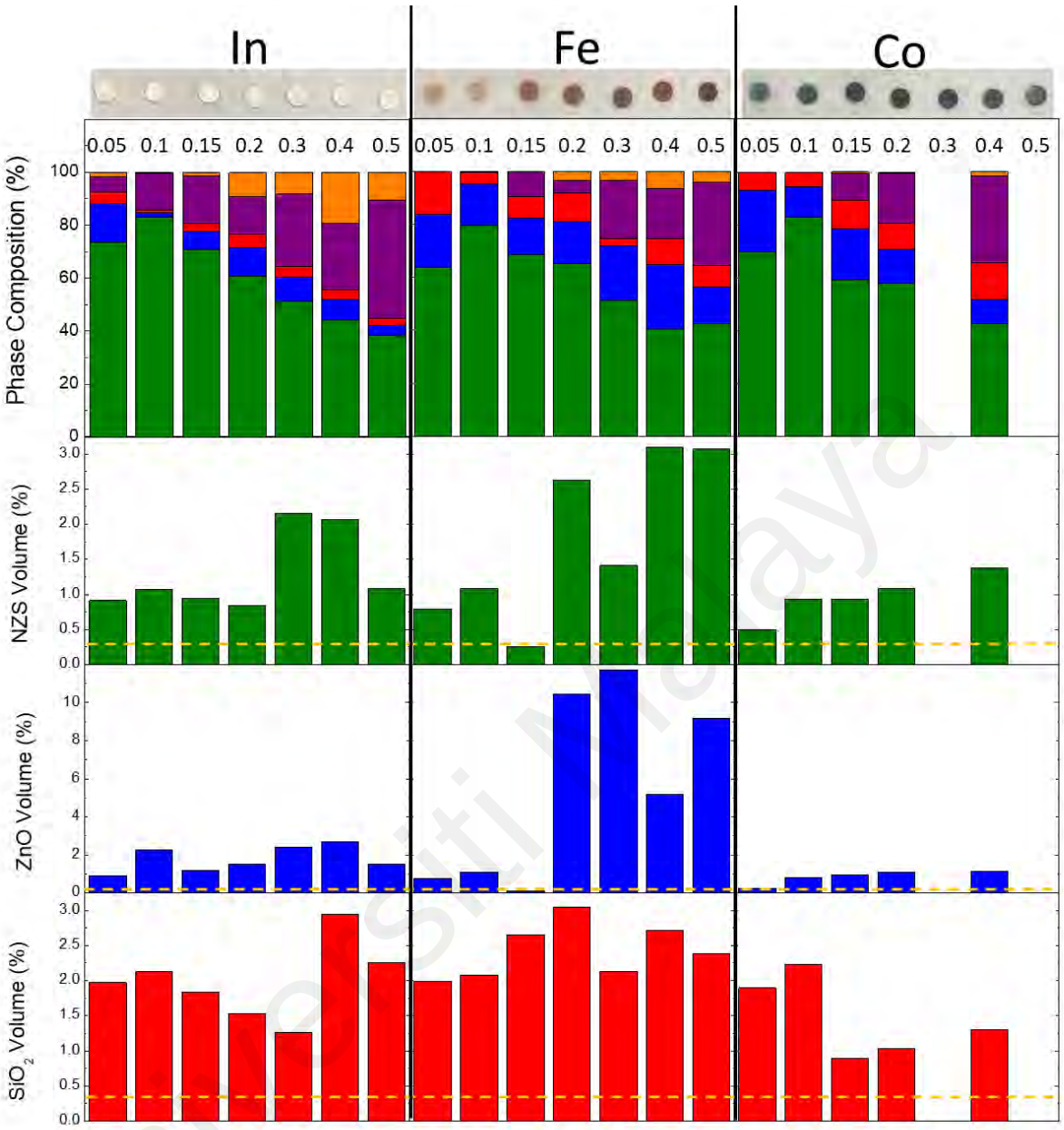

Figure 6.6: Structural changes in In-, Fe-, and Co-substituted NZS from x = 0.05 to x = 0.5. From top: appearance of the pellets; phase compositions where the color-coding follows Figure 6.5; lattice volumes of the three primary phases, where the yellow lines indicate.

6.4.2 Conductivity Studies

Figure 6.7 shows the RT ionic conductivities of the various In-, Co-, and Fe-substituted Clay-NZS HybSSE samples, with reference made to the undoped Clay-NZS HybSSE sample at $x = 0$. For all three substituents, the highest ionic conductivity was obtained at $x = 0.1$, which is also the composition where the highest NZS phase fraction was obtained for all three, as per **Figure 6.6**. It was observed that when the x-value was increased above the optimal value of 0.1, the NZS phase fraction decreases and consequently, so does the ionic conductivity. It is therefore concluded that ionic conductivity increases as the NZS phase fraction increases.

The highest RT ionic conductivity achieved is by $In_{0.1}$, at 0.453 mS cm^{-1}. Moreover, this compound showed an ionic conductivity of 2.27 mS cm^{-1} at 48°C. These values are comparable to the state-of-the-art electrolytes and therefore attractive for further investigation. As discussed in **Subsection 6.4.1**, the predominant secondary phase in In-substituted and Fe-substituted samples are $NaInO_2$ and $NaFeO_2$, respectively, and both

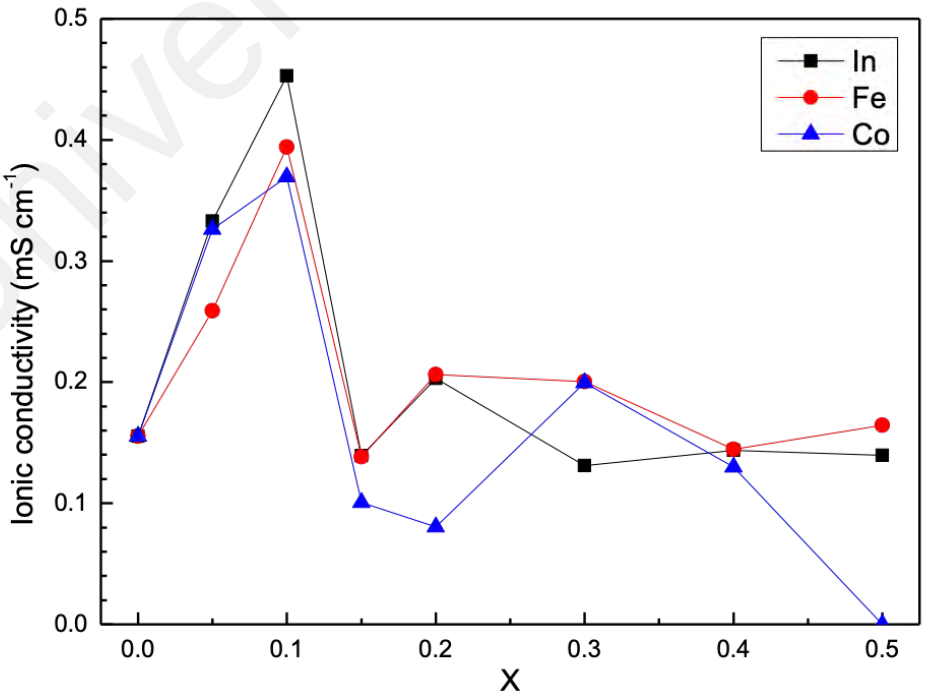

Figure 6.7: Ionic conductivity values of In-, Fe-, and Co-substituted Clay-NZS HybSSE across x value, where the conductivity value at x = 0 is the value of the original Clay-NZS HybSSE.

become more abundant above $x = 0.1$. $NaInO_2$ and $NaFeO_2$ are both layered oxides that are not uncommon in the literature.

In terms of being a solid electrolyte, $NaInO_2$ was last studied in the 1970s by Delmas et al., (1979) and was found to have ionic conductivity, $\sigma = 1.1 \times 10^{-5}$ S cm^{-1} at 700 K (426.85°C), but not ionically conductive at RT. With that, by right, its presence in In-substituted Clay-NZS should not give any significant benefit here, which is consistent with the result shown in **Figure 6.7**. When the phase fraction of $NaInO_2$ in the sample is >10%, i.e., at $x > 0.1$, the sample's σ do not deviate much from the σ of the undoped Clay-NZS HybSSE, indicated by $x = 0$. However, when the phase fraction of $NaInO_2$ in the sample is <10% and x is small yet more than 0, σ steadily increases as x increases, until it reaches its peak at $x = 0.1$, i.e., as $In_{0.1}$ HybSSE. **Appendix J** shows that even as a pristine ceramic SSE (without IL solution), $In_{0.1}$ SSE exhibits higher RT ionic conductivity ($\sigma = 2.08 \times 10^{-6}$ S cm^{-1}) than Clay-NZS SSE ($\sigma = 5.28 \times 10^{-8}$ S cm^{-1}). This means that either a small amount of $NaInO_2$ in the composite have promoted better ionic conduction in the ceramic, or the In element that is doped into the other phases results in improved conductivity. Regardless, an excess of $NaInO_2$ is undeniably detrimental.

On the other hand, literature shows that $NaFeO_2$ is mainly studied as a material in cathodes (Lee et al., 2015; Susanto et al., 2019; Xing et al., 2021). $NaFeO_2$ exists as two polymorphs: α-$NaFeO_2$ (hexagonal) and β-$NaFeO_2$ (orthorhombic). The former has been the main subject of scrutiny for many years for showcasing a more superior properties as a cathode (Kuganathan et al., 2019), but it was very recently shown that the latter gets better attention due to its easier synthesis and better stability in air (Kuganathan et al., 2019; Yanase et al., 2021). Unsurprisingly, this study resulted in the synthesis of the β-polymorph of $NaFeO_2$. Yanase et al., (2021) investigated the ionic conductivity of β-$NaFeO_2$ when heat-treated at various temperatures and it was found that their sample

obtained a conductivity of ~1×10^{-6} S cm^{-1} at RT. Meanwhile, this project's pristine $Fe_{0.1}$ ceramic SSE has a conductivity that is a magnitude lower than β-$NaFeO_2$, i.e., σ = 3.54×10^{-7} S cm^{-1}, as shown in **Appendix J**.

Even though as a pristine ceramic, $Fe_{0.1}$ SSE has σ that is a magnitude lower than the $In_{0.1}$ SSE sample, when both are infused with IL solution to become HybSSE, the σ value of $In_{0.1}$ HybSSE turned out to be 15% higher than $Fe_{0.1}$ HybSSE. Therefore, it is concluded that both components in the HybSSE (ceramic and IL solution) play important roles in reaching optimal ionic conductivities.

6.5 Electrochemical Testing of Enhanced Clay-NZS HybSSE

Although high ionic conductivity and low electronic conductivity are prerequisites for a good electrolyte, the material's stability during electrochemical testing often proves to be the downfall of promising materials. To further screen the promising Fe-, Co-, and In-substituted Clay-NZS HybSSE, a variety of stability tests were performed on $Fe_{0.1}$, $Co_{0.1}$, and $In_{0.1}$ HybSSE.

6.5.1 Stability against Na Metal

Na-Na symmetric cells of the samples were prepared in Swagelok-type cells and were subjected to a voltage hold to evaluate the samples' stability against Na metal. Results are shown in **Figure 6.8**. The first data point in the voltage hold was used to estimate the Na^+ ion conductivity (σ_{Na+}) of the HybSSE sample to ensure that the ionic conductivities extracted from blocking-electrodes EIS measurements discussed in **Subsection 6.3.2** hold up in real cells. For all four HybSSE samples (undoped Clay-NZS, $In_{0.1}$, $Fe_{0.1}$, and $Co_{0.1}$), the conductivity extracted this way was comparable to that from EIS, although they were slightly lower. For $In_{0.1}$ HybSSE, it was found that its $\sigma_{Na+} = 0.113$ mS cm^{-1}. In contrast,

its overall ionic conductivity (σ) as per **Figures 6.3** and **6.7** is 0.453 mS cm^{-1}. Similar deviations are observed in other HybSSE samples too, where the σ_{Na+} value is lower than their corresponding σ value.

In all samples, the conductivity decreases dramatically with time during the hold, demonstrating that the electrolytes are unstable against Na metal, in agreement with the result discussed in **Section 5.5**. It is therefore concluded that the small drop in conductivity between the results shown in **Figure 6.3** and the initial conductivities in **Figure 6.8** is due to this instability taking place in the Na-Na symmetric cell prior to the first measurement. Nonetheless, the fact that the values are close to each other indicates that the ionic conductivities extracted from **Section 6.3** are meaningful in real cells. For all HybSSE samples, the post-voltage-hold EIS show semicircles of bigger radius than the original Nyquist plots in **Figure 6.3**. This is in stark contrast to what is seen when the

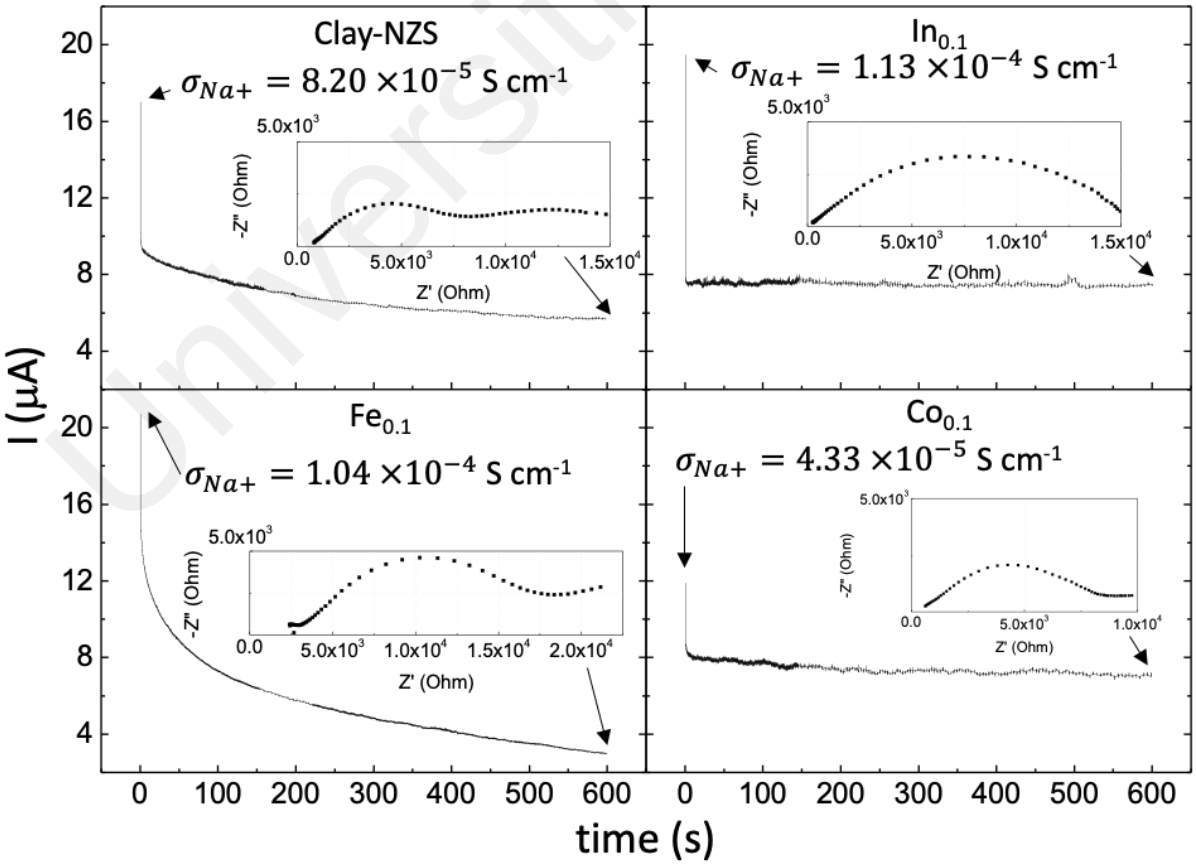

Figure 6.8: Stability of HybSSE against Na, where the initial current value corresponds to their estimated σ_{Na+}, and the inset Nyquist plots show the sample's resistance after 5 min of the DC test.

test is done on the IL solution alone, shown in **Appendix A**, where no impedance growth is seen after the Na symmetric cell test. The higher resistance seen in the hybrids is believed to be caused by the existence of passivation layer at SEI when the sample is in contact with Na metal, consistent with the trend seen as a function of time during the hold. Since the IL solution is stable against Na metal, the instability is concluded to be due to the Clay-NZS ceramic. The instability towards Na metal is a common occurrence in Na SSE (Lou et al., 2021) and is certainly a concern with these HybSSE, as previously discussed in **Section 5.5**.

6.5.2 Electrochemical Stability Window

The ESW of the HybSSE samples were investigated using high-potential and low-potential CV tests, with results shown in **Figures 6.9(a-b)**. It is important to note that in both tests, the HybSSE was used as an electrode material with conductive carbon and the electrolyte is a carbonate-based liquid, as explained in **Subsection 3.5.7**. The average of three duplicates of the control cells were used as the baseline for redox reactions of the carbonate liquid electrolyte used in the cell, indicated by the red lines in **Figures 6.9(a-b)**. Each HybSSE sample's characteristic ESW is then determined to be the first instance where the oxidation (in high potential cycling) and reduction (in low potential cycling) pattern deviates from the control. For the original undoped Clay-NZS HybSSE, it was determined in this method that its ESW is 1.28 – 3.45 V. Compared with the result obtained in **Section 5.5**, only the upper limit of the ESW was able to be determined through LSV. This was previously determined to be 4.32 V but was later found to be an overestimate. To confirm that the feature seen at 3.45 V in **Figure 6.9(a)** is not an artefact of the carbonate electrolyte degradation, the test was repeated using the IL solution as an electrolyte shown in **Appendix K**, where the stability window goes down to 3.3 V. This means that this CV test is proven to be more sensitive in identifying the limits of a sample's ESW, with which was not obtained in the LSV method.

Looking at the result of the doped samples, it was found that $Fe_{0.1}$ HybSSE is the only sample that has a higher oxidation potential as well as a wider ESW compared to the original Clay-NZS HybSSE. In fact, the $Fe_{0.1}$ HybSSE has a very promising ESW of 2.41 – 4.79 V, making it compatible with all promising cathodes. On the other hand, $In_{0.1}$ HybSSE has an ESW of 1.15 – 4.11V and therefore the lowest reduction potential amongst all. The stability of $In_{0.1}$ HybSSE at low voltages was also confirmed using the IL-solution cell and found that the stability window extends down to 0.8 V, as shown in **Appendix L**. Meanwhile, $Co_{0.1}$ HybSSE appears to have the smallest ESW (1.21 – 3.45 V at most, it may in fact be as small as 2.20 – 3.45 V given that a small feature is seen at 2.2 V, marked by the black arrow), making it the lowest performing sample amongst the four HybSSE samples. Therefore, it is deduced that Co0.1 HybSSE is not viable for SIB.

Thus, as far as ESW is concerned, $Fe_{0.1}$ HybSSE exhibits the best performance, followed by $In_{0.1}$ HybSSE that has managed to significantly bring down the reduction potential of the original sample.

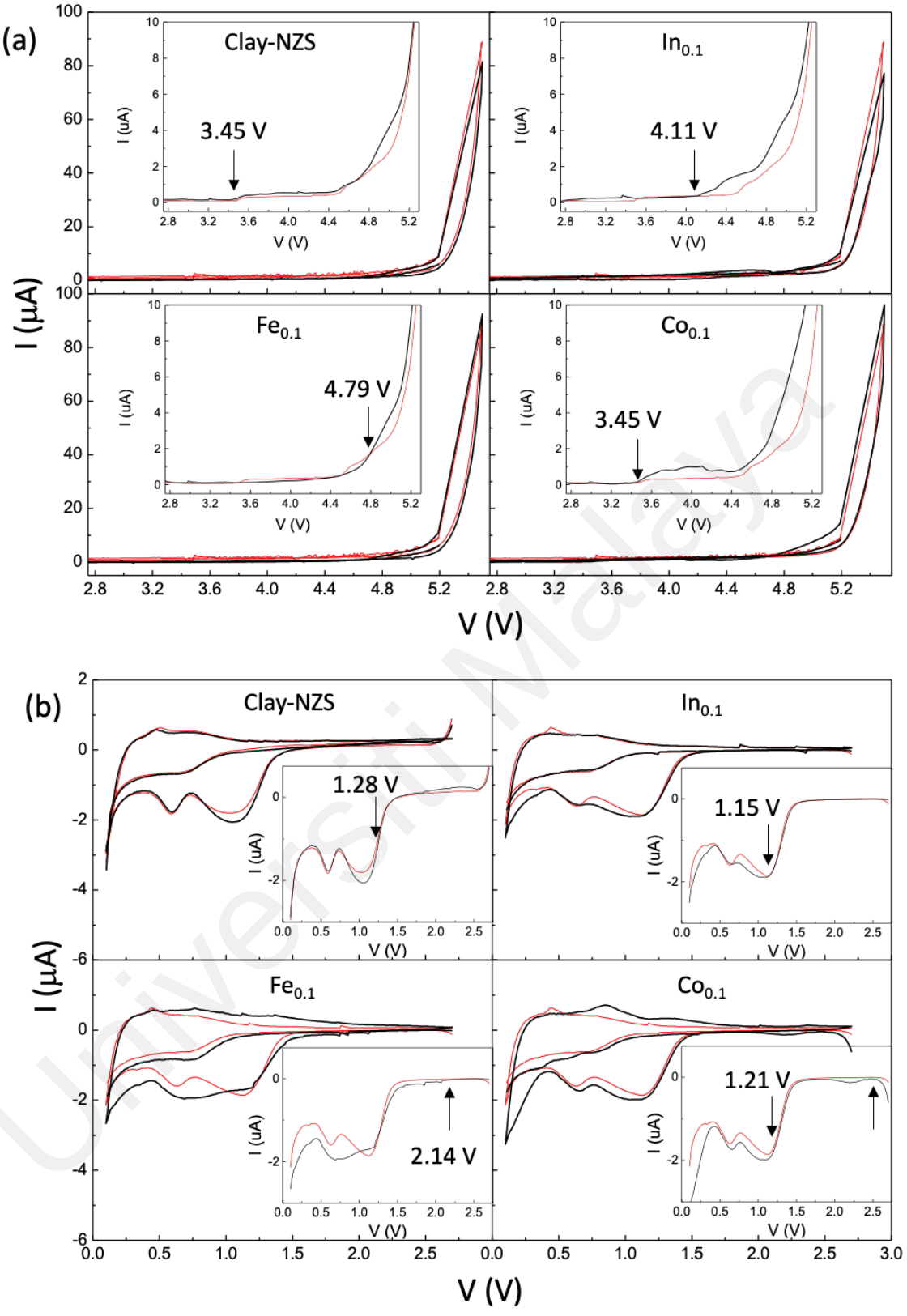

Figure 6.9: CV of HybSSE (black line) at (a) high potential, and (b) low potential, compared to the control cell (red line). Insets are the close-up of the first cycle.

CHAPTER 7: CONCLUSIONS

7.1 Summary of Findings

The aim to synthesise a nanocrystalline solid as a ceramic SSE host for this project's HybSSE was realised by way of having a nanoparticle starting reagent derived from halloysite clay. The process of acid leaching Al_2O_3 from the inner lumens of HNT using sulphuric acid has successfully yielded SiNP, with SiO_2 purity of 83.5(4)%, consisting of both the crystalline and amorphous state. Halloysite clay-derived NZS formed Clay-NZS ceramic with grains that are 5-10 times smaller than Synthetic-NZS. At ~50 nm crystallite size, this grants Clay-NZS to be a nanocrystalline. The clay-derived SiNP made a good substitute to the standard starting reagent of Si for polycrystalline synthesis because NZS was successfully synthesised. Even so, the presence of ZnO is more prominent in Clay-NZS than in Synthetic-NZS, inclusive of the reduction of NZS phase purity i.e., from 95.8% in Synthetic-NZS to 88.0% in Clay-NZS. Regardless, the presence of ZnO is key in the structural stability of NZS to obey Pauling's rule, and its minute existence does not detriment the ionic conductivity and the overall electrochemical performance, even in Clay-NZS SSE.

Impedance measurements show that while Synthetic-NZS SSE demonstrates the typical oxide-based SSE behaviour of having operable temperature at upwards of 300°C, the impedance of Clay-NZS SSE can be measured from as low as 175°C, with calculated ionic conductivity, σ, of 8.74×10^{-9} S cm^{-1} at that temperature. At the maximum measurable temperature of 500°C, Clay-NZS overwhelms Synthetic-NZS as an SSE with $\sigma = 2.95 \times 10^{-5}$ S cm^{-1}, a magnitude higher from Synthetic-NZS's $\sigma = 3.25 \times 10^{-6}$ S cm^{-1}. When their ionic conductivity values across temperatures were related to the Arrhenius equation, it was found that the activation energy, ΔE_A, of both compounds are the same,

i.e., 0.71(2) eV. This means that altering the microstructure of NZS does not alter the intrinsic ΔE_A required for the material to ionically conduct, even though Clay-NZS conducts better than Synthetic-NZS.

Frequency-dependent ionic conductivity values derived from the impedance measurements illustrates the conductivity mechanism within the SSE. Both Clay-NZS and Synthetic-NZS SSE displayed the UDR at high frequencies across all temperatures, revealing that the movement of conducting ions within both sample is through ionic hopping. The hopping frequency was then extracted into the Arrhenius relation to investigate the samples' hopping energy, ΔE_H. It was found that both samples have two different ΔE_H at two temperature regions, i.e., higher at temperatures 375°C and below, and lower at temperatures 400°C and above. This is because ions at higher temperatures have higher kinetic energy, requiring lesser energy to be supplied in order to move. Since both samples have the same ΔE_A that is constant across their operable temperatures, the lower ΔE_H at higher temperatures means that more ions are mobilised at higher temperatures.

The infusion of IL solution into the pores of Clay-NZS sample pellet to form HybSSE was demonstrated to be like a sponge soaked in water. The IL solution does not chemically react with the Clay-NZS ceramic compound and the liquid matrix freely flows within the pellet, regardless of the concentration of NaTFSI salt in the IL solution. The salt concentration only affects the viscosity of the IL solution itself, where higher concentration brings about a more viscous solution. Increased viscosity means less movement of ions, hence higher resistance as an electrolyte. When the highly-viscous IL solution is infused into the Clay-NZS ceramic, this in effect translates into decreased overall ionic conductivity of Clay-NZS HybSSE. Therefore, keeping the salt concentration at a minimum, i.e., 10 wt%, is sufficient to ensure presence of Na^+ ion in

the liquid matrix, while at the same time limiting the impact of IL viscosity in the overall ionic conductivity of Clay-NZS HybSSE. In fact, the highest ionic conductivity at RT is obtained by Clay-NZS:IL:0.1Salt HybSSE sample, which is 2.3×10^{-5} S cm^{-1}. This conductivity value is two times higher than the ionic conductivity of the standalone IL solution as an electrolyte in a practical battery setup. Even so, due to the combustion of IL at higher temperatures, the operable temperature for Clay-NZS HybSSE is limited to only 300°C, which is nevertheless a large window of operating temperatures for practical applications of SIB.

Arrhenius relation plotted from the impedance measurements of Clay-NZS HybSSE across operable temperatures show that the ΔE_A of Clay-NZS HybSSE are ~0.22 eV, regardless of salt concentration in the IL solution. Clay-NZS:IL:0.1Salt HybSSE presents ΔE_A of precisely 0.221(6) eV, which is significantly lower than the ΔE_A of Clay-NZS SSE at 0.71(2) eV. The reduced energy barrier for ionic conduction is understood to be attributed to the liquid-solid dynamics within the pellet of Clay-NZS HybSSE, which is absent in the SSE. Further derivations of the impedance measurements show that Clay-NZS HybSSE does not exhibit ionic hopping behaviour, except at temperatures lower than 100°C, demonstrated by the lack of UDR in the high-frequency region. In addition to that, the ionic conductivity at the low-frequency region showcases a high diffusion rate within the sample, across all operating temperatures. It is therefore concluded that the ionic conduction in Clay-NZS HybSSE is primarily due to ionic diffusion instead of ionic hopping as seen in Clay-NZS SSE. This therefore explains why the ΔE_A value is markedly lower in Clay-NZS HybSSE. Lower energy is required to move an ion through diffusion rather than through hopping from one site to another.

The ionic transference number of all samples of Clay-NZS HybSSE are very close to unity, validating their eligibility to become an electrolyte, with Clay-NZS:IL:0.1Salt exhibiting the highest t_{ion} value at 0.991. Clay-NZS:IL:0.1Salt also establishes itself as a better Na^+ ion conductor, boasting t_+ value of 0.506 that is markedly higher than the other HybSSE samples, as well as the t_+ value of the standalone IL solution. Furthermore, its ESW is initially determined by the LSV method to be 4.32 V. While Clay-NZS:IL:0.3Salt demonstrated a higher ESW of 4.66 V, its current flow is too low to be further considered. Therefore, Clay-NZS HybSSE sample is shown to exhibit the best performance when the IL solution has 10 wt% of NaTFSI salt. Even so, after configuring the material into a half cell, it was found that the Clay-NZS HybSSE is unstable against Na metal in spite showcasing stable cyclability against a composite electrode.

Having gone through the successful fabrication of Clay-NZS HybSSE that can potentially be applied in an SIB, further enhancements were done to maximise this potential. High-throughput techniques allowed for a comprehensive optimisation of Clay-NZS HybSSE performance in a significantly shorter period of time. In total, over 704 Clay-NZS ceramics were synthesized and characterised in high-throughput, with more than 350 of those were studied as HybSSE. This figure is more than 10x of what the earlier stage of this project has managed to investigate, in less than a third of the time spent. The optimisation of the synthesis of Clay-NZS HybSSE resulted in denser and more robust ceramic pellets, yielding a sevenfold increase from its initial ionic conductivity of 2.3×10^{-5} S cm^{-1} at RT, reaching values of 0.16(6) mS cm^{-1}. Moreover, the Clay-NZS ceramic itself as an SSE has managed to obtain an ionic conductivity of 5.28×10^{-8} S cm^{-1} at RT after the synthesis optimisation. This was previously unobtainable by the original unoptimized Clay-NZS SSE, where its lowest operable temperature was 175°C.

The performance of Clay-NZS HybSSE was further enhanced by way of substitution into its ceramic compound, with 22 different elements from the periodic table being doped into the ceramic at a stoichiometry of $Na_2Zn_{1-x}Si_{1-x}A_{2x}O_4$ (where A is the substituent, and doped samples are denoted as A_x). An initial blanket screening was done for all substituents at $x = 0.025, 0.05,$ and 0.1. There was no trend as to whether a certain element causes a rise or fall in ionic conductivity from the undoped Clay-NZS HybSSE. The undoped Clay-NZS HybSSE placed itself at the mid-range ionic conductivity amongst all doped HybSSE. Importantly, all doped HybSSE samples have negligible electronic conductivities, indicating that dendrite growth throughout the pellet will not be a concern. Substituents that were found to improve ionic conductivity with no detriment to electronic conductivity are Ca, Al, Sr, Fe, Co, and In. An optimal substitution level of $x = 0.1$ was found to yield ionic conductivities as high as 0.453 mS cm^{-1} in $In_{0.1}$ HybSSE at RT, and 2.266 mS cm^{-1} at 48°C, making it of interest for use in full SIB. Others include $Fe_{0.1}$ HybSSE with ionic conductivity of 0.394 mS cm^{-1} at RT and $Co_{0.1}$ HybSSE with ionic conductivity of 0.370 mS cm^{-1} at RT.

Systematic targeted study of the In-, Fe-, and Co-substituted materials expanded the substitution levels from the preliminary blanket screening to up to $x = 0.5$. Results showed that the substituents were both integrated into the primary phases present in the unsubstituted materials as well as formed new secondary phases. The integration into primary phases was confirmed by the expansion of the lattice parameters of all three primary phases that exist in the ceramic polycrystalline, namely NZS, ZnO, and SiO_2. Meanwhile, the new phases formed improve ionic conductivities when they are in small amount but shown to be disadvantageous when in an amount that outweighs the NZS phase. The optimal level of $x = 0.1$ was found to not only yield maximum ionic conductivities in all three substituents, but also showed the highest phase fraction of the

NZS, indicating that NZS is nevertheless the main conducting phase in the ceramic, even when a composite is formed.

All the HybSSEs were found to be unstable against Na metal, in agreement with the initial finding for the original Clay-NZS HybSSE synthesised in earlier stage of this project. In terms of ESW, it was found that the LSV method overestimated the upper limit of Clay-NZS HybSSE ESW. Extensive study using the CV method shows that Clay-NZS HybSSE actually has an ESW of 1.28 – 3.45 V, verifying that the CV method as the more sensitive method for true ESW determination. Although the upper limit of Clay-NZS HybSSE is concluded to be considerably low, the doped samples exhibit a significant leap from this baseline. $In_{0.1}$ HybSSE showed stability from 4.11 V down to 0.8 V *vs* Na, making it compatible with some anodes available in the literature. By contrast, stability at high potential is found to be good in all HybSSEs, with the $Fe_{0.1}$ HybSSE showing stability up to 4.79 V *vs*. Na, making it compatible with all cathodes currently being considered for SIBs. As a matter of fact, $Fe_{0.1}$ HybSSE has the widest ESW amongst all samples at 2.14 – 4.79 V. Meanwhile, $Co_{0.1}$ saw itself as the lowest performing sample with ESW of 1.21 – 3.45 V or 2.30 – 3.45 V, eliminating itself as being a better material than the original undoped Clay-NZS HybSSE.

Considering all metrics measured herein, it appears that In and Fe are ideal substituents into Clay-NZS HybSSE, yielding competitive ionic conductivities when substitution level is at $x = 0.1$. They both have RT ionic conductivities comparable to state-of-the-art materials in the literature, promising stability at high potentials. This class of Na quasi-solid electrolytes certainly warrants further exploration with further studies currently underway using these materials in full SIBs.

7.2 Future Works

While the developed HybSSE material holds a big potential in the Na-ion battery field, the next steps to take to really make a homerun out of this material are beyond the scope of this doctorate project.

The most immediate actionable item is to find a compatible anode for the HybSSE to operate with. A compatible anode is defined by the cyclability of the electrolytic material in a cell with the anode, accompanied by minimal or no formation of passivation layer at SEI. This project developed a material that is found to be incompatible with Na metal due to its instability with the ceramic, hence an immediate half-cell battery is not viable. Options to go about this challenge is to either create a separation layer between the Na metal with the Clay-NZS ceramic to insist on using Na metal as the anode of choice, or to alternatively test the material's compatibility with other anodes in the literature.

The next step is to investigate the right mixture of active materials in its composite cathode that can showcase the material in its best performance. While a composite cathode has been fabricated and utilised in this project, the composition mixture was a complete shot in the dark to adequately serve its function in showcasing the stability/instability of the HybSSE with Na metal in a half cell setup. To bring out the best performance out of the HybSSE, thorough investigation of the right cathode for it should also be done before placing the material in a real cell.

It is completely unknown how the HybSSE developed in this project will perform in its testing with anodic and cathodic materials, making the future works bearing the possibility to be a yet another extensive research. Nevertheless, this project has managed to bring an understudied ceramic compound come into light. Therefore, it should not be impossible to find the right combination of cathode and anode for this material to further elevate its potential to be realised into a real SIB.

REFERENCES

Abbas, Q., Mirzaeian, M., Olabi, A.-G., & Gibson, D. (2020). Solid State Electrolytes. In *Reference Module in Materials Science and Materials Engineering*. Elsevier. https://doi.org/10.1016/b978-0-12-803581-8.11740-0

Abdullayev, E., Joshi, A., Wei, W., Zhao, Y., & Lvov, Y. (2012). Enlargement of Halloysite Clay Nanotube Lumen by Selective Etching of Aluminum Oxide. *ACS Nano*, *6*(8), 7216–7226. https://doi.org/10.1021/nn302328x

Adnan, S. B. R. S., & Mohamed, N. S. (2014). Properties of novel Li4-3xCrxSiO4 ceramic electrolyte. *Ceramics International*. https://doi.org/10.1016/j.ceramint.2013.08.136

Adnan, S. B. R. S., Mohamed, N. S., Mustaffa, N. A., Zainal, N., Ibrahim, S., & Radzi, Z. I. (2019). Thermal, structural and electrical properties of Li2BaSiO4 ceramic electrolyte. *Ceramics International*, *45*(1), 1424–1429. https://doi.org/10.1016/j.ceramint.2018.09.199

Adnan, S. B. R. S., Salleh, F. M., & Mohamed, N. S. (2016). Effect of interstitial Li+ ion and vacant site Li+ ion on the properties of novel Li2.05ZnAl0.05Si0.95O4 and Li1.95Zn0.95Cr0.05SiO4 ceramic electrolytes. *Ceramics International*, *42*(15), 17941–17945. https://doi.org/10.1016/j.ceramint.2016.08.047

Agrawal, R. C. (1999). dc Polarisation: An experimental tool in the study of ionic conductors. *Indian Journal of Pure & Applied Physics*, *37*(April), 294–301. http://nopr.niscair.res.in/bitstream/123456789/27118/1/IJPAP 37(4) 294-301.pdf

Ahmad, M. M. (2015). Enhanced lithium ionic conductivity and study of the relaxation and giant dielectric properties of spark plasma sintered Li5La3Nb2O12 nanomaterials. *Ceramics International*, *41*(5), 6398–6408. https://doi.org/10.1016/j.ceramint.2015.01.077

Almond, D. P., & West, A. R. (1983). Mobile ion concentrations in solid electrolytes from an analysis of a.c. conductivity. *Solid State Ionics*, *9–10*(PART 1), 277–282. https://doi.org/10.1016/0167-2738(83)90247-3

Anantharamulu, N., Koteswara Rao, K., Rambabu, G., Vijaya Kumar, B., Radha, V., & Vithal, M. (2011). A wide-ranging review on Nasicon type materials. *Journal of Materials Science*, *46*(9), 2821–2837. https://doi.org/10.1007/s10853-011-5302-5

Appetecchi, G. B., Montanino, M., Passerini, S., Anguillarese, V., Wilhelm, W., & Muenster, U. (2012). Ionic Liquid-Based Electrolytes for High Energy, Safer Lithium Batteries. In *Ionic Liquids: Science and Applications* (Vol. 1117, pp. 67–128). American Chemical Society. https://pubs.acs.org/doi/abs/10.1021/bk-2012-1117.ch004

Ashenhurst, J. (2020). *Infrared Spectroscopy: A Quick Primer on Interpreting Spectra*. Master Organic Chemistry. https://www.masterorganicchemistry.com/2016/11/23/quick_analysis_of_ir_spectra/

Austin, I. G., & Mott, N. F. (2017). *Advances in Physics Polarons in crystalline and non-crystalline materials Polarons in Crystalline and Non-crystalline Materials*. *8732*(July). https://doi.org/10.1080/00018736900101267

Bachman, J. C., Muy, S., Grimaud, A., Chang, H.-H., Pour, N., Lux, S. F., Paschos, O., Maglia, F., Lupart, S., Lamp, P., Giordano, L., & Shao-Horn, Y. (2015). *Inorganic Solid-State Electrolytes for Lithium Batteries: Mechanisms and Properties Governing Ion Conduction*. https://doi.org/10.1021/acs.chemrev.5b00563

Bardakhanov, S., Lysenko, V., Nomoev, A., & Trufanov, D. (2011). Ceramic Preparation of Nanopowders and Experimental Investigation of Its Properties. In *Advances in Ceramics - Synthesis and Characterization, Processing and Specific Applications*. https://doi.org/10.5772/24939

Barpanda, P., Chotard, J.-N., Delacourt, C., Reynaud, M., Filinchuk, Y., Armand, M., Deschamps, M., & Tarascon, J.-M. (2011). LiZnSO4F Made in an Ionic Liquid: A Ceramic Electrolyte Composite for Solid-State Lithium Batteries. *Angewandte Chemie International Edition*, *50*(11), 2526–2531. https://doi.org/10.1002/anie.201006331

Bauluz, B. (2015). Halloysite and kaolinite: two clay minerals with geological and technological importance. *Rev. Real Academia de Ciencias. Zaragoza*, *70*, 7–38.

Bellusci, M., Simonetti, E., De Francesco, M., & Appetecchi, G. B. (2020). Ionic liquid electrolytes for safer and more reliable sodium battery systems. *Applied Sciences (Switzerland)*, *10*(18). https://doi.org/10.3390/APP10186323

Benchakar, M., Naéjus, R., Damas, C., & Santos-Peña, J. (2020). Exploring the use of EMImFSI ionic liquid as additive or co-solvent for room temperature sodium ion battery electrolytes. *Electrochimica Acta*, *330*, 135193. https://doi.org/10.1016/j.electacta.2019.135193

Bernardo, M. S., Jardiel, T., Peiteado, M., Caballero, A. C., & Villegas, M. (2011). Reaction pathways in the solid state synthesis of multiferroic BiFeO3. *Journal of the European Ceramic Society*, *31*(16), 3047–3053. https://doi.org/10.1016/j.jeurceramsoc.2011.03.018

Bohlen, S. R., & Boettcher, A. L. (1982). The Quartz-Coesite Transformation: A Precise Determination and the Effects of Other Components. *Journal of Geophysical Research*, *87*(2), 7073–7078.

Bohnke, O., Ronchetti, S., & Mazza, D. (1999). Conductivity measurements on nasicon and nasicon-modified materials. *Solid State Ionics*, *122*(1–4), 127–136. https://doi.org/10.1016/S0167-2738(99)00062-4

Bokov, D., Turki Jalil, A., Chupradit, S., Suksatan, W., Javed Ansari, M., Shewael, I. H., Valiev, G. H., & Kianfar, E. (2021). Nanomaterial by Sol-Gel Method: Synthesis and Application. *Advances in Materials Science and Engineering*, *2021*. https://doi.org/10.1155/2021/5102014

Bollmann, W., & Bollmann, W. (1970). Point Defects. In *Crystal Defects and Crystalline Interfaces* (pp. 37–40). Springer Berlin Heidelberg.

https://doi.org/10.1007/978-3-642-49173-3_4

Bonizzoni, S. (2020). *Polymer-in-Ceramic Nanocomposite Solid Electrolyte for Lithium Metal Batteries Encompassing PEO-Grafted TiO 2 Nanocrystals*. https://doi.org/10.1149/1945-7111/ab7c72

Bonnick, P., Niitani, K., Nose, M., Suto, K., Arthur, T. S., & Muldoon, J. (2019). A high performance all solid state lithium sulfur battery with lithium thiophosphate solid electrolyte. *Journal of Materials Chemistry A*, *7*(42), 24173–24179. https://doi.org/10.1039/c9ta06971b

Bontempelli, G., Dossi, N., & Toniolo, R. (2016). Linear Sweep and Cyclic. In *Reference Module in Chemistry, Molecular Sciences and Chemical Engineering* (Issue January). Elsevier Inc. https://doi.org/10.1016/b978-0-12-409547-2.12200-0

Brinker, C. J., & Scherer, G. W. (1990). *Sol-gel science : the physics and chemistry of sol-gel processing*. Academic Press.

Bron, P., Johansson, S., Zick, K., Der Günne, J. S. A., Dehnen, S., & Roling, B. (2013). Li10SnP2S12: An affordable lithium superionic conductor. *Journal of the American Chemical Society*, *135*(42), 15694–15697. https://doi.org/10.1021/ja407393y

Bruce, J. A., Ingram, M. D., MacKenzie, M. A., & Syed, R. (1986). Ionic conductivity in glass: A new look at the weak electrolyte theory. *Solid State Ionics*, *18–19*(PART 1), 410–414. https://doi.org/10.1016/0167-2738(86)90151-7

Bruce, P. G., & West, A. R. (1983). The A-C Conductivity of Polycrystalline LISICON, Li2+2xZn1-xGeO4, and a Model for Intergranular Constriction Resistances. *Journal of the Electrochemical Society*, *130*(3), 662–669. https://doi.org/10.1149/1.2119778

Bui, K. M., Dinh, V. A., Okada, S., & Ohno, T. (2016). Na-ion diffusion in a NASICON-type solid electrolyte: A density functional study. *Physical Chemistry Chemical Physics*, *18*(39), 27226–27231. https://doi.org/10.1039/c6cp05164b

Butee, S. P., Kambale, K. R., & Firodiya, M. (2016). Electrical properties of sodium beta-alumina ceramics synthesized by citrate sol-gel route using glycerine. *Processing and Application of Ceramics*, *10*(2), 67–72. https://doi.org/10.2298/PAC1602067B

Ca Dam, M., Dam, D. J., & Clyne, D. J. (1926). The electric conductivity and the activation energy of ionic migration of molten salts and their mixtures Ionic migration of molten salts and their mixtures 393. In *Proc. Am er. Soc. Test. Mater* (Vol. 31). http://rspa.royalsocietypublishing.org/Downloadedfrom

Cao, C., Li, Z. Bin, Wang, X. L., Zhao, X. B., & Han, W. Q. (2014). Recent advances in inorganic solid electrolytes for lithium batteries. In *Frontiers in Energy Research* (Vol. 2, Issue JUN). Frontiers Media S.A. https://doi.org/10.3389/fenrg.2014.00025

Carter, C. B., & Norton, M. G. (2013a). Ceramic Materials: Science and Engineering. In

Ceramic Materials: Science and Engineering. Springer. https://doi.org/10.1007/978-1-4614-3523-5

Carter, C. B., & Norton, M. G. (2013b). Point Defects, Charge, and Diffusion. In *Ceramic Materials: Science and Engineering* (pp. 187–206). Springer. https://doi.org/10.1007/978-1-4614-3523-5

Carter, C. B., & Norton, M. G. (2013c). Sintering and Grain Growth. In *Ceramic Materials: Science and Engineering* (pp. 1–766). Springer. https://doi.org/10.1007/978-1-4614-3523-5

Chadwick, A. V. (2005). Fast Ion Conductors. In *Handbook of Materials Modeling* (pp. 1901–1914). Springer Netherlands. https://doi.org/10.1007/978-1-4020-3286-8_98

Chandra Babu, B., & Buddhudu, S. (2011). Structural, Thermal and Dielectric Properties of Lithium Zinc Silicate Ceramic Powders by Sol-Gel Method. *Article in Ferroelectrics, Letters Section*, *38*, 114–127. https://doi.org/10.1080/07315171.2011.623610

Che, H., Chen, S., Xie, Y., Wang, H., Amine, K., Liao, X. Z., & Ma, Z. F. (2017). Electrolyte design strategies and research progress for room-temperature sodium-ion batteries. *Energy and Environmental Science*, *10*(5), 1075–1101. https://doi.org/10.1039/c7ee00524e

Chen, F., Howlett, P., & Forsyth, M. (2018). Na-Ion Solvation and High Transference Number in Superconcentrated Ionic Liquid Electrolytes: A Theoretical Approach. *Journal of Physical Chemistry C*, *122*(1), 105–114. https://doi.org/10.1021/acs.jpcc.7b09322

Chen, Q., Liu, S., Zhu, R., Wu, D., Fu, H., Zhu, J., & He, H. (2018). Clay minerals derived nanostructured silicon with various morphology: Controlled synthesis, structural evolution, and enhanced lithium storage properties. *Journal of Power Sources*, *405*, 61–69. https://doi.org/10.1016/J.JPOWSOUR.2018.10.031

Chen, W., Lei, T., Wu, C., Deng, M., Gong, C., Hu, K., Ma, Y., Dai, L., Lv, W., He, W., Liu, X., Xiong, J., & Yan, C. (2018). Designing Safe Electrolyte Systems for a High-Stability Lithium–Sulfur Battery. In *Advanced Energy Materials* (Vol. 8, Issue 10). Wiley-VCH Verlag. https://doi.org/10.1002/aenm.201702348

Cheng, M., Qu, T., Zi, J., Yao, Y., Liang, F., Ma, W., Yang, B., Dai, Y., & Lei, Y. (2020). A hybrid solid electrolyte for solid-state sodium ion batteries with good cycle performance. *Nanotechnology*, *31*(42), 425401. https://doi.org/10.1088/1361-6528/ABA059

Chi, C., Katsui, H., & Goto, T. (2017). Effect of Li addition on the formation of Na-β/β″-alumina film by laser chemical vapor deposition. *Ceramics International*, *43*(1), 1278–1283. https://doi.org/10.1016/J.CERAMINT.2016.10.077

Chotipanich, J., Arpornwichanop, A., Yonezawa, T., & Kheawhom, S. (2018). Electronic and ionic conductivities enhancement of zinc anode for flexible printed zinc-air battery. *Engineering Journal*, *22*(2), 47–57. https://doi.org/10.4186/ej.2018.22.2.47

Choudhary, Y. S., Jothi, L., & Nageswaran, G. (2017). Electrochemical Characterization. In *Spectroscopic Methods for Nanomaterials Characterization* (Vol. 2, pp. 19–54). Elsevier Inc. https://doi.org/10.1016/B978-0-323-46140-5.00002-9

Danks, A. E., Hall, S. R., & Schnepp, Z. (2016). The evolution of 'sol–gel' chemistry as a technique for materials synthesis. *Materials Horizons*, *3*(2), 91–112. https://doi.org/10.1039/C5MH00260E

de la Torre-Gamarra, C., Appetecchi, G. B., Ulissi, U., Varzi, A., Varez, A., & Passerini, S. (2018). Na3Si2Y0.16Zr1.84PO12-ionic liquid hybrid electrolytes: An approach for realizing solid-state sodium-ion batteries? *Journal of Power Sources*, *383*(September), 157–163. https://doi.org/10.1016/j.jpowsour.2017.12.037

Delmas, C., Maazaz, A., Fouassier, C., Réau, J. M., & Hagenmuller, P. (1979). Influence de l'environnement de l'ion alcalin sur sa mobilite dans les structures a feuillets Ax(LxM1-x)O2. *Materials Research Bulletin*, *14*(3), 329–335. https://doi.org/10.1016/0025-5408(79)90097-7

Deng, Y., Eames, C., Fleutot, B., David, R., Chotard, J. N., Suard, E., Masquelier, C., & Islam, M. S. (2017). Enhancing the Lithium Ion Conductivity in Lithium Superionic Conductor (LISICON) Solid Electrolytes through a Mixed Polyanion Effect. *ACS Applied Materials and Interfaces*, *9*(8), 7050–7058. https://doi.org/10.1021/acsami.6b14402

Despotuli, A. L., Andreeva, A. V., & Rambabu, B. (2005). Nanoionics of advanced superionic conductors. *Ionics*, *11*(3–4), 306–314. https://doi.org/10.1007/BF02430394

Dhahri, A., Dhahri, E., & Hlil, E. K. (2018). Electrical conductivity and dielectric behaviour of nanocrystalline La0.6Gd0.1Sr0.3Mn0.75Si0.25O3. *RSC Advances*, *8*(17), 9103–9111. https://doi.org/10.1039/c8ra00037a

Dieterich, W. (1981). Theory of high ionic conductivity in solids. *Solid State Ionics*, *5*(C), 21–26. https://doi.org/10.1016/0167-2738(81)90189-2

Dirican, M., Yan, C., Zhu, P., & Zhang, X. (2019). Composite solid electrolytes for all-solid-state lithium batteries. *Materials Science and Engineering: R: Reports*, *136*, 27–46. https://doi.org/10.1016/J.MSER.2018.10.004

Do, M. P., Bucher, N., Nagasubramanian, A., Markovits, I., Bingbing, T., Fischer, P. J., Loh, K. P., Kühn, F. E., & Srinivasan, M. (2019). Effect of Conducting Salts in Ionic Liquid Electrolytes for Enhanced Cyclability of Sodium-Ion Batteries. In *ACS Applied Materials and Interfaces* (Vol. 11, Issue 27, pp. 23972–23981). https://doi.org/10.1021/acsami.9b03279

Dunn, B., Kamath, H., & Tarascon, J.-M. (2011). *Electrical Energy Storage for the Grid: A Battery of Choices System power ratings, module size*. *334*(6058), 928–935. https://doi.org/10.1126/science.1212741

Egbue, O., & Long, S. (2012). Critical issues in the supply chain of lithium for electric vehicle batteries. *EMJ - Engineering Management Journal*, *24*(3), 52–62.

https://doi.org/10.1080/10429247.2012.11431947

Elgrishi, N., Rountree, K. J., McCarthy, B. D., Rountree, E. S., Eisenhart, T. T., & Dempsey, J. L. (2018). A Practical Beginner's Guide to Cyclic Voltammetry. *Journal of Chemical Education*, *95*(2), 197–206. https://doi.org/10.1021/acs.jchemed.7b00361

Eliche-Quesada, D., Pérez-Villarejo, L., & José Sánchez-Soto, P. (2019). Introductory Chapter: Ceramic Materials - Synthesis, Characterization, Applications and Recycling. In *Ceramic Materials - Synthesis, Characterization, Applications and Recycling* (pp. 1–5). IntechOpen. https://doi.org/10.5772/intechopen.84710

Eshetu, G. G., Elia, G. A., Armand, M., Forsyth, M., Komaba, S., Rojo, T., & Passerini, S. (2020). Electrolytes and Interphases in Sodium-Based Rechargeable Batteries: Recent Advances and Perspectives. *Advanced Energy Materials*, *10*(20). https://doi.org/10.1002/aenm.202000093

Esposito, S. (2019). "Traditional" sol-gel chemistry as a powerful tool for the preparation of supported metal and metal oxide catalysts. *Materials*, *12*(4), 1–25. https://doi.org/10.3390/ma12040668

Etsell, T. H., & Flengas, S. N. (1970). THE ELECTRICAL PROPERTIES OF SOLID OXIDE ELECTROLYTES. *Chemical Reviews*, *70*, 339–376. https://doi.org/10.1016/S0166-2481(10)34002-5

Evans, J., Vincent, C. A., & Bruce, P. G. (1987). Electrochemical measurement of transference numbers in polymer electrolytes. *Polymer*, *28*(13), 2324–2328. https://doi.org/10.1016/0032-3861(87)90394-6

Feifel, S. C., & Lisdat, F. (2011). Silica nanoparticles for the layer-by-layer assembly of fully electro-active cytochrome c multilayers. *Journal of Nanobiotechnology*, *9*(1), 59. https://doi.org/10.1186/1477-3155-9-59

Feng, J., Wang, L., Chen, Y., Wang, P., Zhang, H., & He, X. (2021). PEO based polymer-ceramic hybrid solid electrolytes: a review. In *Nano Convergence* (Vol. 8, Issue 1, pp. 1–12). Korea Nano Technology Research Society. https://doi.org/10.1186/s40580-020-00252-5

Ferdousi, S. A., O'Dell, L. A., Hilder, M., Barlow, A. J., Armand, M., Forsyth, M., & Howlett, P. C. (2021). SEI Formation on Sodium Metal Electrodes in Superconcentrated Ionic Liquid Electrolytes and the Effect of Additive Water. *ACS Applied Materials and Interfaces*, *13*(4), 5706–5720. https://doi.org/10.1021/ACSAMI.0C18119/SUPPL_FILE/AM0C18119_SI_001.PDF

Fergus, J. W. (2010). Ceramic and polymeric solid electrolytes for lithium-ion batteries. *Journal of Power Sources*, *195*(15), 4554–4569. https://doi.org/10.1016/j.jpowsour.2010.01.076

Fleischauer, M. D., Hatchard, T. D., & Dahn, J. R. (2005). Combinatorial investigations of advanced Li-ion rechargeable battery electrode materials You may also like Combinatorial investigations of advanced Li-ion rechargeable battery electrode

materials. *Meas. Sci. Technol*, *16*, 212–220. https://doi.org/10.1088/0957-0233/16/1/028

Fong, K. D., Self, J., Diederichsen, K. M., Wood, B. M., McCloskey, B. D., & Persson, K. A. (2019). Ion Transport and the True Transference Number in Nonaqueous Polyelectrolyte Solutions for Lithium Ion Batteries. *ACS Central Science*, *5*(7), 1250–1260. https://doi.org/10.1021/acscentsci.9b00406

Forsyth, M., Yoon, H., Chen, F., Zhu, H., MacFarlane, D. R., Armand, M., & Howlett, P. C. (2016). Novel Na+ Ion Diffusion Mechanism in Mixed Organic-Inorganic Ionic Liquid Electrolyte Leading to High Na+ Transference Number and Stable, High Rate Electrochemical Cycling of Sodium Cells. *Journal of Physical Chemistry C*, *120*(8), 4276–4286. https://doi.org/10.1021/acs.jpcc.5b11746

Franklin, A. D. (1972). Statistical Thermodynamics of Point Defects in Crystals. In *Point Defects in Solids* (pp. 1–101). Springer US. https://doi.org/10.1007/978-1-4684-2970-1_1

Fu, L., Yang, H., Tang, A., & Hu, Y. (2017). Engineering a tubular mesoporous silica nanocontainer with well-preserved clay shell from natural halloysite. *Nano Research*, *10*, 2782–2799. https://doi.org/10.1007/s12274-017-1482-x

Gaaz, T. S., Sulong, A. B., Kadhum, A. A. H., Nassir, M. H., & Al-Amiery, A. A. (2016). Impact of Sulfuric Acid Treatment of Halloysite on Physico-Chemic Property Modification. *Materials (Basel, Switzerland)*, *9*(8). https://doi.org/10.3390/ma9080620

Gao, J., Zhao, Y. S., Shi, S. Q., & Li, H. (2015). Lithium-ion transport in inorganic solid state electrolyte. In *Chinese Physics B* (Vol. 25, Issue 1, pp. 18211–018211). Institute of Physics Publishing. https://doi.org/10.1088/1674-1056/25/1/018211

Garcia-Garcia, D., Ferri, J. M., Ripoll, L., Hidalgo, M., Lopez-Martinez, J., & Balart, R. (2017). Characterization of selectively etched halloysite nanotubes by acid treatment. *Applied Surface Science*, *422*, 616–625. https://doi.org/10.1016/J.APSUSC.2017.06.104

Gebert, F., Knott, J., Gorkin, R., Chou, S. L., & Dou, S. X. (2021). Polymer electrolytes for sodium-ion batteries. *Energy Storage Materials*, *36*, 10–30. https://doi.org/10.1016/J.ENSM.2020.11.030

Gomez, E. (2021). Quasi-solid-state lithium metal batteries using the LiNi0.8Co0.1Mn0.1O2-Li1+ xAlxTi2- x(PO4)3composite positive electrode. In *Verified Market Reports* (Vol. 118122). Verified Market Research. https://doi.org/10.1021/ACSAMI.1C14487/SUPPL_FILE/AM1C14487_SI_001.PDF

Gonzalo-Juan, I., & Riedel, R. (2016). Ceramic synthesis from condensed phases. *ChemTexts*, *2*(2), 1–21. https://doi.org/10.1007/S40828-016-0024-6/FIGURES/25

Goodenough, J B, Hong, H. Y., & Kafalas, J. A. (1976). Fast Na+ ion Transport in Skeleton Structures. *Materials Research Bulletin*, *11*, 203–220.

Goodenough, John B, & Park, K.-S. (2013). The Li-Ion Rechargeable Battery: A Perspective. *J. Am. Chem. Soc*, *135*, 1167–1176. https://doi.org/10.1021/ja3091438

Gorrasi, G., & Sorrentino, A. (2015). Mechanical milling as a technology to produce structural and functional bio-nanocomposites. *Green Chemistry*, *17*(5), 2610–2625. https://doi.org/10.1039/C5GC00029G

Grins, J. (1982). Ionic Conductivity of Sodium Zinc Silicates in the Compositional Region Na2ZnSiO4-Na2ZnSi2O6. *Solid State Ionics*, *7*, 157–164.

Grosjean, C., Herrera Miranda, P., Perrin, M., & Poggi, P. (2012). Assessment of world lithium resources and consequences of their geographic distribution on the expected development of the electric vehicle industry. *Renewable and Sustainable Energy Reviews*, *16*(3), 1735–1744. https://doi.org/10.1016/j.rser.2011.11.023

Guerra, O. J., Eichman, J., & Denholm, P. (2021). Optimal energy storage portfolio for high and ultrahigh carbon-free and renewable power systems. *Energy & Environmental Science*, *14*(10), 5132–5146. https://doi.org/10.1039/D1EE01835C

Hayashi, A., Masuzawa, N., Yubuchi, S., Tsuji, F., Hotehama, C., Sakuda, A., & Tatsumisago, M. (2019). A sodium-ion sulfide solid electrolyte with unprecedented conductivity at room temperature. *Nature Communications*, *10*(1), 1–6. https://doi.org/10.1038/s41467-019-13178-2

Hayes, W. (1978). Superionic conductors. *Contemporary Physics*, *19*(5), 469–486. https://doi.org/10.1080/00107517808210895

Herczog, A. (1985). Sodium Ion Conducting Glasses for the Sodium-Sulfur Battery. *Journal of The Electrochemical Society*, *132*(7), 1539–1545. https://doi.org/10.1149/1.2114161

Hirsh, H. S., Li, Y., S Tan, D. H., Zhang, M., Zhao, E., Shirley Meng, Y., Hirsh, H. S., Li, Y., S Tan, D. H., Zhang, M., Zhao, E., & Meng, Y. S. (2020). Sodium-Ion Batteries Paving the Way for Grid Energy Storage. *Advanced Energy Materials*, *10*(32), 2001274. https://doi.org/10.1002/AENM.202001274

Hong, H. Y. P. (1978). Crystal structure and ionic conductivity of Li14Zn(GeO4)4 and other new Li+ superionic conductors. *Materials Research Bulletin*, *13*(2), 117–124. https://doi.org/10.1016/0025-5408(78)90075-2

Horowitz, Y., Moran Lifshitz, =, Greenbaum, A., Feldman, Y., Greenbaum, S., Sokolov, A. P., & Golodnitsky, D. (2020). *Review-Polymer/Ceramic Interface Barriers: The Fundamental Challenge for Advancing Composite Solid Electrolytes for Li-Ion Batteries*. https://doi.org/10.1149/1945-7111/abcd12

Hou, M., Liang, F., Chen, K., Dai, Y., & Xue, D. (2020). Challenges and perspectives of NASICON-type solid electrolytes for all-solid-state lithium batteries. In *Nanotechnology* (Vol. 31, Issue 13, p. 132003). Institute of Physics Publishing. https://doi.org/10.1088/1361-6528/ab5be7

Hou, W., Guo, X., Shen, X., Amine, K., Yu, H., & Lu, J. (2018). Solid electrolytes and interfaces in all-solid-state sodium batteries: Progress and perspective. *Nano*

Energy, *52*(June), 279–291. https://doi.org/10.1016/j.nanoen.2018.07.036

Hu, Y.-W., Raistruck, I. D., & Huggins, R. A. (1977). Ionic Conductivity of Lithium Orthosilicate—Lithium Phosphate Solid Solutions. *Journal of The Electrochemical Society*, *124*(8), 1240. https://doi.org/10.1149/1.2133537

Huang, M., Liu, T., Deng, Y., Geng, H., Shen, Y., Lin, Y., & Nan, C. W. (2011). Effect of sintering temperature on structure and ionic conductivity of Li 7 - XLa 3Zr 2O 12 - 0.5x (x = 0.5 ~ 0.7) ceramics. *Solid State Ionics*, *204–205*(1), 41–45. https://doi.org/10.1016/j.ssi.2011.10.003

Huggins, R. A. (2009). Potentials. In *Advanced Batteries Materials Science Aspects* (p. 263). https://doi.org/10.1007/978-0-387-76424-5

Hussain, F., Rahman, M. Z., Sivasengaran, A. N., & Hasanuzzaman, M. (2020). Energy storage technologies. In *Energy for Sustainable Development: Demand, Supply, Conversion and Management* (pp. 125–165). Academic Press. https://doi.org/10.1016/B978-0-12-814645-3.00006-7

International Union of Pure and Applied Chemistry. (n.d.). *IUPAC Compendium of Chemical Terminology*. Retrieved November 19, 2019, from https://goldbook.iupac.org/

IR Spectrum Table & Chart. (n.d.). Sigma-Aldrich. Retrieved May 2, 2020, from https://www.sigmaaldrich.com/technical-documents/articles/biology/ir-spectrum-table.html

Isa, K. B. M., Othman, L., Hambali, D., & Osman, Z. (2017). Electrical and electrochemical studies on sodium ion-based gel polymer electrolytes. *AIP Conference Proceedings*, *1877*(September). https://doi.org/10.1063/1.4999867

Islam, M. S., & Fisher, C. A. J. (2014). Lithium and sodium battery cathode materials: computational insights into voltage, diffusion and nanostructural properties. *Chem. Soc. Rev.*, *43*(1), 185–204. https://doi.org/10.1039/C3CS60199D

Ivanov, S. (2012). Multiferroic complex metal oxides: Main features of preparation, structure, and properties. *Science and Technology of Atomic, Molecular, Condensed Matter and Biological Systems*, *2*(1), 163–238. https://doi.org/10.1016/B978-0-44-453681-5.00007-8

Jalalian-Khakshour, A., Phillips, C. O., Jackson, L., Dunlop, T. O., Margadonna, S., & Deganello, D. (2020). Solid-state synthesis of NASICON (Na3Zr2Si2PO12) using nanoparticle precursors for optimisation of ionic conductivity. *Journal of Materials Science*, *55*(6), 2291–2302. https://doi.org/10.1007/s10853-019-04162-8

Jock Churchman, G., Pasbakhsh, P., & Hillier, S. (2016). The rise and rise of halloysite. *Clay Minerals*, *51*(3), 303–308. https://doi.org/10.1180/claymin.2016.051.3.00

Jonderian, A., Anderson, E., Peng, R., Xu, P., Jia, S., & Cozea, V. (2022). Suite of High-Throughput Experiments for Screening Solid Electrolytes for Li Batteries Suite of High-Throughput Experiments for Screening Solid Electrolytes for Li Batteries. *Journal of The Electrochemical Society*, *169*, 050504.

https://doi.org/10.1149/1945-7111/ac6a15

Jonderian, A., & McCalla, E. (2021). The role of metal substitutions in the development of Li batteries, part II: Solid electrolytes. *Materials Advances*, *2*(9), 2846–2875. https://doi.org/10.1039/d1ma00082a

Jonderian, A., Ting, M., & McCalla, E. (2021). Metastability in Li-La-Ti-O Perovskite Materials and Its Impact on Ionic Conductivity. *Chemistry of Materials*, *33*(12), 4792–4804. https://doi.org/10.1021/acs.chemmater.1c01490

Jonscher, A. K. (1972). Frequency-dependence of conductivity in hopping systems. *Journal of Non-Crystalline Solids*, *10*, 293–315.

Joussein, E. (2016). Geology and Mineralogy of Nanosized Tubular Halloysite. In *Developments in Clay Science* (Vol. 7, pp. 12–48). Elsevier B.V. https://doi.org/10.1016/B978-0-08-100293-3.00002-9

Kamat, A., Huth, A., Klein, O., & Scholl, S. (2010). Chronoamperometric Investigations of the Electrode-Electrolyte Interface of a Commercial High Temperature PEM Fuel Cell. *Fuel Cells*, *10*(6), 983.

Kang, J., Chung, H., Doh, C., Kang, B., & Han, B. (2015). Integrated study of first principles calculations and experimental measurements for Li-ionic conductivity in Al-doped solid-state LiGe2(PO4)3 electrolyte. *Journal of Power Sources*, *293*, 11–16. https://doi.org/10.1016/j.jpowsour.2015.05.060

Kang, S.-J. L. (2005). GRAIN BOUNDARY ENERGY AND SINTERING. *Sintering*, 139–143. https://doi.org/10.1016/B978-075066385-4/50010-8

Kanno, R., Hata, T., Kawamoto, Y., & Irie, M. (2000). Synthesis of a new lithium ionic conductor, thio-LISICON-lithium germanium sulfide system. *Solid State Ionics*, *130*(1), 97–104. https://doi.org/10.1016/S0167-2738(00)00277-0

Kavanagh, L., Keohane, J., Cabellos, G. G., Lloyd, A., & Cleary, J. (2018). Global lithium sources-industrial use and future in the electric vehicle industry: A review. *Resources*, *7*(3). https://doi.org/10.3390/resources7030057

Keller, M., Varzi, A., & Passerini, S. (2018). Hybrid electrolytes for lithium metal batteries. *Journal of Power Sources*, *392*(February), 206–225. https://doi.org/10.1016/j.jpowsour.2018.04.099

Kim, B. G., Jang, W., Park, Y. J., Kang, H., Seo, J. H., & Wang, D. H. (2020). Chelating Agent Mediated Sol−Gel Synthesis for Efficient Hole Extracted Perovskite Photovoltaics. *J. Phys. Chem. C*, *124*. https://doi.org/10.1021/acs.jpcc.0c05804

Kim, H. W., Manikandan, P., Lim, Y. J., Kim, J. H., Nam, S., & Kim, Y. (2016). Hybrid solid electrolyte with the combination of $Li_7La_3Zr_2O_{12}$ ceramic and ionic liquid for high voltage pseudo-solid-state Li-ion batteries. *Journal of Materials Chemistry A*, *4*(43), 17025–17032. https://doi.org/10.1039/C6TA07268B

Kim, Jin Il, Chung, K. Y., & Park, J. H. (2018). Design of a porous gel polymer

electrolyte for sodium ion batteries. *Journal of Membrane Science*, *566*, 122–128. https://doi.org/10.1016/j.memsci.2018.08.066

Kim, J.-K., Lim, Y. J., Kim, H., Cho, G.-B., & Kim, Y. (2015). A hybrid solid electrolyte for flexible solid-state sodium batteries. *Energy Environ. Sci*, *8*, 3589. https://doi.org/10.1039/c5ee01941a

Kim, Jung-joon, Yoon, K., Park, I., & Kang, K. (2017). Progress in the Development of Sodium-Ion Solid Electrolytes. *Small Methods*, *1*(10), 1700219. https://doi.org/10.1002/smtd.201700219

Kong, L. B., Zhang, T. S., Ma, J., & Boey, F. (2008). Progress in synthesis of ferroelectric ceramic materials via high-energy mechanochemical technique. *Progress in Materials Science*, *53*(2), 207–322. https://doi.org/10.1016/J.PMATSCI.2007.05.001

Kotobuki, M., Munakata, H., & Kanamura, K. (2013). All-Solid-State Li Battery for Future Energy Technology. In *Handbook of Advanced Ceramics: Materials, Applications, Processing, and Properties: Second Edition* (pp. 343–351). Elsevier Inc. https://doi.org/10.1016/B978-0-12-385469-8.00019-8

Kriaa, A., Hajji, M., Jamoussi, F., & Hamzaoui, A. H. (2014). Electrical conductivity of 1: 1 and 2: 1 clay minerals. *Surface Engineering and Applied Electrochemistry*, *50*(1), 84–94. https://doi.org/10.3103/S1068375514010104

Kudo, T., & Kawamura, J. (2005). Fast ionic conductors. In *Materials for Energy Conversion Devices: A Volume in Woodhead Publishing Series in Electronic and Optical Materials* (pp. 174–211). Elsevier Inc. https://doi.org/10.1533/9781845690915.2.174

Kuganathan, N., Kelaidis, N., & Chroneos, A. (2019). Defect chemistry, sodium diffusion and doping behaviour in NaFeO2 polymorphs as cathode materials for Na-ion batteries: A computational study. In *Materials* (Vol. 12, Issue 19). https://doi.org/10.3390/ma12193243

Kurajica, S. (2019). A Brief Review on the Use of Chelation Agents in Sol-gel Synthesis…. *Chem. Biochem. Eng. Q*, *33*(3), 295–301. https://doi.org/10.15255/CABEQ.2018.1566

Kuray, P., Mei, W., Sheffield, S. E., Sengeh, J., Pulido, C. R. F., Capparelli, C., Hickey, R. J., & Hickner, M. A. (2020). Ion Transport in Solvated Sodium-Ion Conducting Gel Polymer Electrolytes. *Frontiers in Earth Science*, *8*(October), 1–15. https://doi.org/10.3389/fenrg.2020.569387

Lazzara, G., Cavallaro, G., Panchal, A., Fakhrullin, R., Stavitskaya, A., Vinokurov, V., & Lvov, Y. (2018). An assembly of organic-inorganic composites using halloysite clay nanotubes. *Current Opinion in Colloid & Interface Science*, *35*, 42–50. https://doi.org/10.1016/j.cocis.2018.01.002

Lee, E., Brown, D. E., Alp, E. E., Ren, Y., Lu, J., Woo, J. J., & Johnson, C. S. (2015). New Insights into the Performance Degradation of Fe-Based Layered Oxides in Sodium-Ion Batteries: Instability of Fe3+/Fe4+ Redox in α-NaFeO2. *Chemistry of*

Materials, *27*(19), 6755–6764. https://doi.org/10.1021/ACS.CHEMMATER.5B02918

Li, J., Li, F., Zhang, L., Zhang, H., Lassi, U., & Ji, X. (2021). Recent applications of ionic liquids in quasi-solid-state lithium metal batteries. *Green Chemical Engineering*, *2*(3), 253–265. https://doi.org/10.1016/J.GCE.2021.03.001

Li, M., Frerichs, J. E., Kolek, M., Sun, W., Zhou, D., Huang, C. J., Hwang, B. J., Hansen, M. R., Winter, M., & Bieker, P. (2020). Solid-State Lithium–Sulfur Battery Enabled by Thio-LiSICON/Polymer Composite Electrolyte and Sulfurized Polyacrylonitrile Cathode. *Advanced Functional Materials*, *30*(14), 1910123. https://doi.org/10.1002/adfm.201910123

Li, M. M., Lu, X., Zhan, X., Engelhard, M. H., Bonnett, J. F., Polikarpov, E., Jung, K., Reed, D. M., Sprenkle, V. L., & Li, G. (2021). High performance sodium-sulfur batteries at low temperature enabled by superior molten Na wettability. *Chemical Communications*, *57*(1), 45–48. https://doi.org/10.1039/d0cc06987f

Liang, J., Luo, J., Sun, Q., Yang, X., Li, R., & Sun, X. (2019). Recent progress on solid-state hybrid electrolytes for solid-state lithium batteries. *Energy Storage Materials*. https://doi.org/10.1016/J.ENSM.2019.06.021

Lin, Y., Wang, X., Liu, J., & Miller, J. D. (2017). Natural halloysite nano-clay electrolyte for advanced all-solid-state lithium-sulfur batteries. *Nano Energy*, *31*, 478–485. https://doi.org/10.1016/J.NANOEN.2016.11.045

Ling, M., Zhu, X., Jiang, Y., & Zhu, J. (2016). Comparative study of solid-state reaction and sol-gel process for synthesis of Zr-doped Li0.5La0.5TiO3 solid electrolytes. *Ionics*, *22*(11), 2151–2156. https://doi.org/10.1007/s11581-016-1744-8

Liu, J., Luo, W., Zhao, Y., Yang, Y., Han, L., Saito, T., C-t, H., Lehmann, M. L., Zhu, J., Liu, T., Zhou, Z., Tang, X., Heish, C.-T., Sokolov, A. P., Cao, P., & Chelsea Chen, X. (2020). *Recent Developments and Challenges in Hybrid Solid Electrolytes for Lithium-Ion Batteries*. https://doi.org/10.3389/fenrg.2020.00202

Liu, P., Guo, B., An, T., Fang, H., Zhu, G., Jiang, C., & Jiang, X. (2017). High throughput materials research and development for lithium ion batteries. *Journal of Materiomics*, *3*(3), 202–208. https://doi.org/10.1016/J.JMAT.2017.07.004

Liu, Z., Chen, J., Wang, X., Wang, Y., Wang, D., & Mao, Z. (2020). Synthesis and characterization of high ionic-conductive sodium beta-alumina solid electrolyte derived from boehmite. *Journal of Materials Science: Materials in Electronics 2020 31:20*, *31*(20), 17670–17678. https://doi.org/10.1007/S10854-020-04321-7

Liu, Z., Wang, X., Chen, J., Tang, Y., Mao, Z., & Wang, D. (2021). *Gel Polymer Electrolyte Membranes Boosted with Sodium-Conductive β-Alumina Nanoparticles: Application for Na-Ion Batteries*. https://doi.org/10.1021/acsaem.0c02513

Lou, S., Zhang, F., Fu, C., Chen, M., Ma, Y., Yin, G., & Wang, J. (2021). Interface Issues and Challenges in All-Solid-State Batteries: Lithium, Sodium, and Beyond. *Advanced Materials*, *33*(6), 1–29. https://doi.org/10.1002/adma.202000721

Lu, J., Li, Y., Kong, Y., & Zhang, N. (2018). Study of structure and conductivity of Li3/8Sr7/16-3x/2LaxZr1/4Nb3/4O3 solid electrolytes. *Ceramics International*, *44*(5), 4744–4750. https://doi.org/10.1016/j.ceramint.2017.12.058

Lu, Xia, Wang, S., Xiao, R., Shi, S., Li, H., & Chen, L. (2017). First-principles insight into the structural fundamental of super ionic conducting in NASICON MTi2(PO4)3 (M = Li, Na) materials for rechargeable batteries. *Nano Energy*, *41*(July), 626–633. https://doi.org/10.1016/j.nanoen.2017.09.044

Lu, Xiaochuan, Lemmon, J. P., Sprenkle, V., & Yang, Z. (2010). Sodium-beta alumina batteries: Status and challenges. *The Journal of Materials*, *62*(9), 31–36. https://doi.org/10.1007/S11837-010-0132-5

Lun, H., Ouyang, J., & Yang, H. (2014). Natural halloysite nanotubes modified as an aspirin carrier. *RSC Advances*, *4*(83), 44197–44202. https://doi.org/10.1039/c4ra09006c

Lun, P., Chen, Z., Zhang, Z., Tan, S., & Chen, D. (2018). Enhanced ionic conductivity in halloysite nanotube-poly(vinylidene fluoride) electrolytes for solid-state lithium-ion batteries. *RSC Advances*, *8*(60), 34232–34240. https://doi.org/10.1039/C8RA06856A

Maier, J. (2005). Nanoionics: ion transport and electrochemical storage in confined systems. *Nature Materials*, *4*(November), 805–815.

Maier, Joachim. (1995). Ionic conduction in space charge regions. *Progress in Solid State Chemistry*, *23*(3), 171–263. https://doi.org/10.1016/0079-6786(95)00004-E

Maier, Joachim. (2009). Nanoionics: ionic charge carriers in small systems. *Physical Chemistry Chemical Physics*, *11*(17), 3010. https://doi.org/10.1039/b905911n

Maier, Joachim. (2014). Pushing nanoionics to the limits: Charge carrier chemistry in extremely small systems. *Chemistry of Materials*, *26*(1), 348–360. https://doi.org/10.1021/cm4021657

Makhlooghiazad, F., Yunis, R., Mecerreyes, D., Armand, M., Howlett, P. C., & Forsyth, M. (2017). Comparison of the physicochemical and electrochemical behaviour of mixed anion phosphonium based OIPCs electrolytes for sodium batteries. *Solid State Ionics*, *312*(December), 44–52. https://doi.org/10.1016/j.ssi.2017.10.014

Marom, T., Goldfarb, A., Russo, E., & Roth, Y. (2010). Battery ingestion in children. *International Journal of Pediatric Otorhinolaryngology*, *74*(8), 849–854. https://doi.org/10.1016/j.ijporl.2010.05.019

Martínez-Juárez, A., Pecharromán, C., Iglesias, J. E., & Rojo, J. M. (1998). Relationship between activation energy and bottleneck size for Li+ ion conduction in NASICON materials of composition LiMM′(PO4)3; M, M′ = Ge, Ti, Sn, Hf. *Journal of Physical Chemistry B*, *102*(2), 372–375. https://doi.org/10.1021/jp973296c

Mayr, L. M., & Fuerst, P. (2008). The future of high-throughput screening. *Journal of Biomolecular Screening*, *13*(6), 443–448.

https://doi.org/10.1177/1087057108319644

Mazumdar, D., Bose, D. N., & Mukherjee, M. L. (1984). TRANSPORT AND DIELECTRIC PROPERTIES OF LISICON. *Solid State Ionics*, *14*, 143–147. https://doi.org/10.1016/0167-2738(84)90089-4

McCalla, E., Parmaklis, M., Rehman, S., Anderson, E., Jia, S., Hebert, A., Potts, K., Jonderian, A., Adhikari, T., & Adamič, M. (2021). Combinatorial methods in advanced battery materials design. *Canadian Journal of Chemistry*, *514*, 1–37. https://doi.org/10.1139/cjc-2021-0111

Meng, F., Long, T., Xu, B., Zhao, Y., Hu, Z., Zhang, L., & Liu, J. (2020). Electrolyte Technologies for High Performance Sodium-Ion Capacitors. *Frontiers in Chemistry*, *8*, 652. https://doi.org/10.3389/FCHEM.2020.00652

Meshram, P., Pandey, B. D., & Mankhand, T. R. (2014). Extraction of lithium from primary and secondary sources by pre-treatment, leaching and separation: A comprehensive review. *Hydrometallurgy*, *150*, 192–208. https://doi.org/10.1016/j.hydromet.2014.10.012

Miller, F. A., & Wilkins, C. H. (1952). Infrared Spectra and Characteristic Frequencies of Inorganic Ions Their Use in Qualitative Analysis. *Journal of Analytical Chemistry*, *24*(8), 1253–1294. https://pubs.acs.org/sharingguidelines

Mitoff, S. P., Will, F. G., & Scotia, N. (1972). Primary sodium-water battery (Patent No. 3,703,415). In *United States Patent Office* (3,703,415). https://doi.org/10.1145/178951.178972

Monti, D., Jónsson, E., Palacín, M. R., & Johansson, P. (2014). Ionic liquid based electrolytes for sodium-ion batteries: Na+ solvation and ionic conductivity. *Journal of Power Sources*, *245*, 630–636. https://doi.org/10.1016/J.JPOWSOUR.2013.06.153

Mortimer, R. J. (2016). Spectroelectrochemistry, methods and instrumentation. In *Encyclopedia of Spectroscopy and Spectrometry* (3rd ed., Vol. 13). Elsevier Ltd. https://doi.org/10.1016/B978-0-12-803224-4.00289-2

Naqash, S., Tietz, F., & Guillon, O. (2018). Synthesis and characterization of equimolar Al/Y-substituted NASICON solid solution Na1+2x+yAlxYxZr2−2xSiyP3−yO12. *Solid State Ionics*, *319*, 13–21. https://doi.org/10.1016/J.SSI.2018.01.048

Nernst-Gottingen. (1899). Uber die elektrolytische leitung fester korper bei sehr hohen temperaturen. *Zeitschrift Fur Elektrochemie*, *6*, 41–43.

Nitta, N., Wu, F., Lee, J. T., & Yushin, G. (2015). Li-ion battery materials: present and future. *Materials Today*, *18*(5), 252–264. https://doi.org/10.1016/J.MATTOD.2014.10.040

Oh, J. A. S., He, L., Plewa, A., Morita, M., Zhao, Y., Sakamoto, T., Song, X., Zhai, W., Zeng, K., & Lu, L. (2019). Composite NASICON (Na3Zr2Si2PO12) Solid-State Electrolyte with Enhanced Na+ Ionic Conductivity: Effect of Liquid Phase Sintering. *ACS Applied Materials and Interfaces*, *11*(43), 40125–40133.

https://doi.org/10.1021/acsami.9b14986

Ohno, H. (2011). *Electrochemical aspects of ionic liquids*. Wiley. https://www.wiley.com/en-us/Electrochemical+Aspects+of+Ionic+Liquids%2C+2nd+Edition-p-9780470647813

Olabi, A. G., Onumaegbu, C., Wilberforce, T., Ramadan, M., Abdelkareem, M. A., & Al – Alami, A. H. (2021). Critical review of energy storage systems. *Energy*, *214*, 118987. https://doi.org/10.1016/J.ENERGY.2020.118987

Olivetti, E. A., Ceder, G., Gaustad, G. G., & Fu, X. (2017). Lithium-Ion Battery Supply Chain Considerations: Analysis of Potential Bottlenecks in Critical Metals. In *Joule* (Vol. 1, Issue 2, pp. 229–243). Cell Press. https://doi.org/10.1016/j.joule.2017.08.019

Onstad, E. (2021). CATL's new sodium ion battery to help ease lithium shortages. *Reuters Energy*. https://www.reuters.com/business/energy/catls-new-sodium-ion-battery-help-ease-lithium-shortages-2021-08-03/

Ortiz-landeros, J., Comez-Yanez, C., Palacios-romero, L. M., Lima, E., & Pfeiffer, H. (2012). *Structural and Thermochemical Chemisorption of CO2 on Li4+x(Si1−xAlx)O4 and Li4−x(Si1−xVx)O4 Solid Solutions*. https://doi.org/10.1021/jp3006298

Padma Kumar, P., & Yashonath, S. (2006). Ionic Conduction in the Solid State. *Journal of Chemical Sciences*, *118*(1), 135–154. https://doi.org/10.1007/BF02708775

Pal, S. K., Saha, R., Vijay Kumar, G., & Omar, S. (2020). Designing High Ionic Conducting NASICON-type Na Solid-Electrolytes for Na-Ion Batteries. *J. Phys. Chem. C*, *124*, 2021. https://doi.org/10.1021/acs.jpcc.0c00543

Palomares, V., Serras, P., Villaluenga, I., Hueso, K. B., Carretero-González, J., & Rojo, T. (2012). Na-ion batteries, recent advances and present challenges to become low cost energy storage systems. *Energy and Environmental Science*, *5*(3), 5884–5901. https://doi.org/10.1039/c2ee02781j

Persson, K. (2014a). *Materials Data on Na2ZnSiO4 (Pc[7]) by Materials Project (ID: mp-6391)*. Materials Project. https://doi.org/10.17188/1279813

Persson, K. (2014b). *Materials Data on SiO2 (C2/c[15]) by Materials Project (ID: mp-11684)*. https://doi.org/10.17188/1188146

Persson, K. (2014c). *Materials Data on ZnO (P63mc[186]) by Materials Project (ID: mp-2133)*. https://doi.org/10.17188/1196748

Pfeiffer, H., Bosch, P., & Bulbulian, S. (1999). Synthesis of lithium silicates. *Adv. Sci. Technol. (Faenza, Italy)*, *14*(Ceramics: Getting into the 2000's, Pt. B), 57–63.

Piras, C. C., Fernández, S., Fernández-Prieto, F., & De Borggraeve, W. M. (2019). Ball milling: a green technology for the preparation and functionalisation of nanocellulose derivatives. *Nanoscale Advances*, *1*, 937–947.

https://doi.org/10.1039/c8na00238j

Plashnitsa, L. S., Kobayashi, E., Noguchi, Y., Okada, S., & Yamaki, J. (2010). Performance of NASICON Symmetric Cell with Ionic Liquid Electrolyte. *Journal of The Electrochemical Society*, *157*(4), A536–A543. https://doi.org/10.1149/1.3298903

Potts, K. P., Grignon, E., & McCalla, E. (2019). Accelerated Screening of High-Energy Lithium-Ion Battery Cathodes. *ACS Applied Energy Materials*, *2*(12), 8388–8393. https://doi.org/10.1021/acsaem.9b01887

Praseptiangga, D., Lail Zahara, H., Ismu Widjanarko, P., Made Joni, I., & Panatarani, C. (2020). *Preparation and FTIR spectroscopic studies of SiO2-ZnO nanoparticles suspension for the development of carrageenan-based bio- nanocomposite film*. *2219*, 100005. https://doi.org/10.1063/5.0003434

Rahal, A., Borchani, S. M., Guidara, K., & Megdiche, M. (2018). Electrical, dielectric properties and study of ac electrical conduction mechanism of li0.9 □0.1 niv0.5 p0.5 o4. *Royal Society Open Science*, *5*(2). https://doi.org/10.1098/rsos.171472

Ran, L., Tao, S., Gentle, I., Luo, B., Li, M., Rana, M., Wang, L., & Knibbe, R. (2021). Stable Interfaces in a Sodium Metal-Free, Solid-State Sodium-Ion Battery with Gradient Composite Electrolyte. *ACS Applied Materials and Interfaces*, *13*(33), 39355–39362. https://doi.org/10.1021/ACSAMI.1C09792/ASSET/IMAGES/MEDIUM/AM1C09792_M003.GIF

Rao, C. N. R., & Gopalakrishnan, J. (1997). New Directions in Solid State Chemistry. *New Directions in Solid State Chemistry*. https://doi.org/10.1017/CBO9780511623141

Ratti, R. (2014). *Ionic Liquids : Synthesis and Applications in Catalysis*. *2014*(3).

Rawtani, D., Agrawal, Y. K., & Rawtani, D. (2012). Multifarious Applications of Halloysite Nanotubes: A Review. *Rev. Adv. Mater. Sci*, *30*, 282–295.

Rizwana, Mahboob, S., & Sarah, P. (2018). AC and DC conductivity due to hopping mechanism in double ion doped ceramics. *AIP Conference Proceedings*, *1952*. https://doi.org/10.1063/1.5032042

Rodríguez-Ramírez, R., Romero-Ibarra, I., & Vazquez-Arenas, J. (2020). Synthesis of sodium zincsilicate (Na2ZnSiO4) and heterogeneous catalysis towards biodiesel production via Box-Behnken design. *Fuel*, *280*. https://doi.org/10.1016/J.FUEL.2020.118668

Roth, E. P., & Orendorff, C. J. (2012). How electrolytes influence battery safety. *Electrochemical Society Interface*, *21*(2), 45–49. https://doi.org/10.1149/2.F04122if

Rüther, T., Bhatt, A. I., Best, A. S., Harris, K. R., & Hollenkamp, A. F. (2020). Electrolytes for Lithium (Sodium) Batteries Based on Ionic Liquids: Highlighting the Key Role Played by the Anion. *Batteries & Supercaps*, *3*(9), 793–827.

https://doi.org/10.1002/batt.202000022

Sahu, G., Lin, Z., Li, J., Liu, Z., Dudney, N., & Liang, C. (2014). Air-stable, high-conduction solid electrolytes of arsenic-substituted Li4SnS4. *Energy and Environmental Science*, *7*(3), 1053–1058. https://doi.org/10.1039/c3ee43357a

Saklar, S., & Yorukoglu, A. (2015). Effects of Acid Leaching on Halloysite. *Physicochem. Probl. Miner. Process*, *51*(1), 83–94. https://doi.org/10.5277/ppmp150108

Sawicki, M., & Shaw, L. (2015). Advances and Challenges of Sodium Ion Batteries as Post Lithium Ion Batteries. *RSC Advances*, *5*, 53129–53154. https://doi.org/10.1039/C5RA08321D

Schlem, R., Till, P., Weiss, M., Krauskopf, T., Culver, S. P., & Zeier, W. G. (2019a). Ionic Conductivity of the NASICON-Related Thiophosphate Na1+xTi2−xGax(PS4)3. *Chemistry - A European Journal*, *25*(16), 4143–4148. https://doi.org/10.1002/chem.201805569

Schlem, R., Till, P., Weiss, M., Krauskopf, T., Culver, S. P., & Zeier, W. G. (2019b). Ionic Conductivity of the NASICON-Related Thiophosphate $Na_{1+x}Ti_{2-x}Ga_{x}(PS_4)_3$. *Chemistry – A European Journal*, *25*(16), 4143–4148. https://doi.org/10.1002/chem.201805569

Schoonman, J. (2000). Nanostructured materials in solid state ionics. *Solid State Ionics*, *135*(1–4), 5–19. https://doi.org/10.1016/S0167-2738(00)00324-6

Selvamani, R., Singh, G., & Tiwari, V. S. (2016). Grain size effect on impedance and modulus properties of (Na 0.5 Bi 0.5 TiO 3) (1−x) (BaZrO 3) x ceramics. *Materials Research Express*, *3*(5), 056301. https://doi.org/10.1088/2053-1591/3/5/056301

Serra Moreno, J., Maresca, G., Panero, S., Scrosati, B., & Appetecchi, G. B. (2014). Sodium-conducting ionic liquid-based electrolytes. *Electrochemistry Communications*, *43*, 1–4. https://doi.org/10.1016/j.elecom.2014.02.010

Shen, L., Yang, J., Liu, G., Avdeev, M., & Yao, X. (2021). High ionic conductivity and dendrite-resistant NASICON solid electrolyte for all-solid-state sodium batteries. *Materials Today Energy*, *20*, 100691. https://doi.org/10.1016/J.MTENER.2021.100691

Shen, Y., Han, X., Cai, T., Hu, H., Li, Y., Zhao, L., Hu, H., Xue, Q., Zhao, Y., Zhou, J., Gao, X., Xing, W., & Wang, X. (2020). High-performance aqueous sodium-ion battery using a hybrid electrolyte with a wide electrochemical stability window. *RSC Advances*, *10*, 25496. https://doi.org/10.1039/d0ra04640j

Shin, J.-H., Henderson, W. A., & Passerini, S. (2005). PEO-Based Polymer Electrolytes with Ionic Liquids and Their Use in Lithium Metal-Polymer Electrolyte Batteries. *Journal of The Electrochemical Society*, *152*(5), A978. https://doi.org/10.1149/1.1890701

Sigma-Aldrich. (2005). Ionic Liquids for Electrochemical Applications. In *ChemFiles*

(Vol. 5, Issue 6, p. 10). https://www.sigmaaldrich.com/technical-documents/articles/chemfiles/ionic-liquids-electrochemical.html

Singh, A. K., & Singh, A. K. (2016). Structure, Synthesis, and Application of Nanoparticles. *Engineered Nanoparticles*, 19–76. https://doi.org/10.1016/B978-0-12-801406-6.00002-9

Singh, M. D., & Dalvi, A. (2019). Novel hybrid composites NaCF3SO3–PEO–NASICON for sodium ion battery applications. *AIP Conference Proceedings*, *2115*(1), 030565. https://doi.org/10.1063/1.5113404

Siraj, K. (2012). Past, Present and Future of Superionic Conductors. *Int. J. Nano & Matl. Sci.*, *1*(1), 1–20.

Sodium-ion Battery Market Size, Scope, Forecast to 2029. (2021). https://www.verifiedmarketresearch.com/product/sodium-ion-battery-market/

Solvionic. (2021). *1-Butyl-1-methylpyrrolidinium bis(trifluoromethanesulfonyl)imide Safety Data Sheet* (Issue 6). https://msds.orica.com/pdf/shess-en-mtr-ughs-000022017701.pdf

Song, S., Lu, J., Zheng, F., Duong, H. M., & Lu, L. (2015). A facile strategy to achieve high conduction and excellent chemical stability of lithium solid electrolytes. *RSC Advances*, *5*(9), 6588–6594. https://doi.org/10.1039/c4ra11287c

Susanto, D., Cho, M. K., Ali, G., Kim, J. Y., Chang, H. J., Kim, H. S., Nam, K. W., & Chung, K. Y. (2019). Anionic Redox Activity as a Key Factor in the Performance Degradation of NaFeO2 Cathodes for Sodium Ion Batteries. *Chemistry of Materials*, *31*(10), 3644–3651. https://doi.org/10.1021/ACS.CHEMMATER.9B00149

Susman, S., Delbecq, C. J., McMillan, J. A., & Roche, M. F. (1983). NASIGLAS: A new vitreous electrolyte. *Solid State Ionics*, *9–10*(PART 1), 667–673. https://doi.org/10.1016/0167-2738(83)90312-0

Takada, K. (2016). Solid electrolytes and solid-state batteries. *AIP Conference Proceedings*, *1765*, 020008. https://doi.org/10.1063/1.4961900

Takada, K., & Ohno, T. (2016). Experimental and computational approaches to interfacial resistance in solid-state batteries. *Frontiers in Energy Research*, *4*(MAR), 1–7. https://doi.org/10.3389/fenrg.2016.00010

Tang, B., Zhao, Y., Wang, Z., Chen, S., Wu, Y., Tseng, Y., Li, L., Guo, Y., Zhou, Z., & Bo, S.-H. (2021). Ultrathin salt-free polymer-in-ceramic electrolyte for solid-state sodium batteries. *EScience*, *1*(2), 194–202. https://doi.org/10.1016/J.ESCI.2021.12.001

Tanwar, M., Bezabh, H. K., Basu, S., Su, W. N., & Hwang, B. J. (2019). Investigation of Sodium Plating and Stripping on a Bare Current Collector with Different Electrolytes and Cycling Protocols [Research-article]. *ACS Applied Materials and Interfaces*, *11*(43), 39746–39756. https://doi.org/10.1021/acsami.9b10097

Tegally, H., San, J. E., Giandhari, J., & de Oliveira, T. (2020). Unlocking the efficiency of genomics laboratories with robotic liquid-handling. *BMC Genomics*, *21*(1). https://doi.org/10.1186/S12864-020-07137-1

Tel'Nova, G. B., & Solntsev, K. A. (2015). Structure and ionic conductivity of a beta-alumina-based solid electrolyte prepared from sodium polyaluminate nanopowders. *Inorganic Materials*, *51*(3), 257–266. https://doi.org/10.1134/S0020168515030176

Thiagarajan, S., Sanmugam, A., & Vikraman, D. (2017). Facile Methodology of Sol-Gel Synthesis for Metal Oxide Nanostructures. *Recent Applications in Sol-Gel Synthesis*. https://doi.org/10.5772/INTECHOPEN.68708

Tong, J., Wu, S., von Solms, N., Liang, X., Huo, F., Zhou, Q., He, H., & Zhang, S. (2020). The Effect of Concentration of Lithium Salt on the Structural and Transport Properties of Ionic Liquid-Based Electrolytes. *Frontiers in Chemistry*, *7*(February), 1–10. https://doi.org/10.3389/fchem.2019.00945

Treacher, J. C., Wood, S. M., Saiful Islam, M., & Kendrick, E. (2016). Na2CoSiO4 as a cathode material for sodium-ion batteries: structure, electrochemistry and diffusion pathways. *Phys. Chem. Chem. Phys*, *18*, 32744. https://doi.org/10.1039/c6cp06777h

Tuller, H. (2017). Ionic Conduction and Applications. In *Springer Handbook of Electronic and Photonic Materials* (pp. 1–1). Springer International Publishing. https://doi.org/10.1007/978-3-319-48933-9_11

Ummartyotin, S., Bunnak, N., & Manuspiya, H. (2016). A comprehensive review on modified clay based composite for energy based materials. *Renewable and Sustainable Energy Reviews*, *61*, 466–472. https://doi.org/10.1016/j.rser.2016.04.022

Vaalma, C., Buchholz, D., Weil, M., & Passerini, S. (2018). A cost and resource analysis of sodium-ion batteries. *Nature Reviews Materials 2018 3:4*, *3*(4), 1–11. https://doi.org/10.1038/natrevmats.2018.13

Valderrama, J. O., Forero, L. A., & Rojas, R. E. (2012). Critical Properties and Normal Boiling Temperature of Ionic Liquids. Update and a New Consistency Test. *Industrial & Engineering Chemistry Research*, *51*(22), 7838–7844. https://doi.org/10.1021/ie202934g

Van Gog, H., & Van Huis, M. A. (2019). Structural and Electronic Properties of Frenkel and Schottky Defects at the MgO{100} Surface: Spin Polarization, Mid-Band Gap States, and Charge Trapping at Vacancy Sites. *Journal of Physical Chemistry C*, *123*(23), 14408–14420. https://doi.org/10.1021/acs.jpcc.9b01908

Vartanian, A. (2021). Breaking down ceramic synthesis. *Nature Reviews Materials*, *6*(6), 464. https://doi.org/10.1038/s41578-021-00335-7

Vignarooban, K., Kushagra, R., Elango, A., Badami, P., Mellander, B.-E., Xu, X., Tucker, T. G., Nam, C., & Kannan, A. M. (2016). Current trends and future challenges of electrolytes for sodium-ion batteries. *International Journal of*

Hydrogen Energy, *41*(4), 2829–2846. https://doi.org/10.1016/J.IJHYDENE.2015.12.090

Wagner, J. B., & Wagner, C. (1957). Electrical Conductivity Measurements on Cuprous Halides. *The Journal of Chemical Physics*, *26*(6), 1597–1601. https://doi.org/10.1063/1.1743590

Wan, H., Mwizerwa, J. P., Han, F., Weng, W., Yang, J., Wang, C., & Yao, X. (2019). Grain-boundary-resistance-less Na3SbS4-xSex solid electrolytes for all-solid-state sodium batteries. *Nano Energy*, *66*, 104109. https://doi.org/10.1016/j.nanoen.2019.104109

Wan, T. H., Lu, Z., & Ciucci, F. (2018). A first principle study of the phase stability, ion transport and substitution strategy for highly ionic conductive sodium antipervoskite as solid electrolyte for sodium ion batteries. *Journal of Power Sources*, *390*(December 2017), 61–70. https://doi.org/10.1016/j.jpowsour.2018.03.073

Wang, J. C., Gaffari, M., & Choi, S. Il. (1975). On the ionic conduction in β-alumina: Potential energy curves and conduction mechanism. *The Journal of Chemical Physics*, *63*(2), 772–778. https://doi.org/10.1063/1.431356

Wang, K., Yin, Z., & Zhao, P. (2016). Synthesis of macroporous Li4SiO4 via a citric acid-based sol–gel route coupled with carbon coating and its CO2 chemisorption properties. *Ceramics International*, *42*(2), 2990–2999. https://doi.org/10.1016/j.ceramint.2015.10.083

Wang, L., Shang, J., Huang, Q., Hu, H., Zhang, Y., Xie, C., Luo, Y., Gao, Y., Wang, H., & Zheng, Z. (2021). Smoothing the Sodium-Metal Anode with a Self-Regulating Alloy Interface for High-Energy and Sustainable Sodium-Metal Batteries. *Advanced Materials*, *33*(41), 2102802. https://doi.org/10.1002/ADMA.202102802

Wang, Y., Song, S., Xu, C., Hu, N., Molenda, J., & Lu, L. (2019). Development of solid-state electrolytes for sodium-ion battery–A short review. *Nano Materials Science*, *1*(2), 91–100. https://doi.org/10.1016/j.nanoms.2019.02.007

Wang, Y., Song, S., Xu, C., Hu, N., Molenda, J., & Lu, L. (2021). Development of solid-state electrolytes for sodium-ion battery-A short review. *Elements*, *1*(2), 91–100. https://doi.org/10.1016/j.nanoms.2019.02.007

Whittingham, M. S., & Huggins, R. A. (1971). Measurement of Sodium Ion Transport in Beta Alumina Using Reversible Solid Electrodes. *The Journal of Chemical Physics*, *54*(1), 414. https://doi.org/10.1063/1.1674623

Winslow, K. M., Laux, S. J., & Townsend, T. G. (2018). A review on the growing concern and potential management strategies of waste lithium-ion batteries. In *Resources, Conservation and Recycling* (Vol. 129, pp. 263–277). Elsevier B.V. https://doi.org/10.1016/j.resconrec.2017.11.001

Wu, F., Zhu, N., Bai, Y., Liu, L., Zhou, H., & Wu, C. (2016). Highly Safe Ionic Liquid Electrolytes for Sodium-Ion Battery: Wide Electrochemical Window and Good

Thermal Stability. *ACS Applied Materials and Interfaces*, *8*(33), 21381–21386. https://doi.org/10.1021/ACSAMI.6B07054

Xiang, W., Liang, S., Zhou, Z., Qin, W., & Fei, W. (2016). Extraction of lithium from salt lake brine containing borate anion and high concentration of magnesium. *Hydrometallurgy*, *166*, 9–15. https://doi.org/10.1016/j.hydromet.2016.08.005

Xing, Y., Akbar, M., Yousaf, M., Shah, M. Y., Xia, C., Gao, J., & Wang, X. (2021). CeO2 coated NaFeO2 proton-conducting electrolyte for solid oxide fuel cell. *International Journal of Hydrogen Energy*, *46*(15), 9855–9860. https://doi.org/10.1016/J.IJHYDENE.2020.05.219

Xu, P., Tan, D. H. S., & Chen, Z. (2021). Emerging trends in sustainable battery chemistries. *Trends in Chemistry*, *3*(8), 620–630. https://doi.org/10.1016/J.TRECHM.2021.04.007

Xue, W., Yang, Y., Yang, Q., Liu, Y., Wang, L., Chen, C., & Cheng, R. (2018). The effect of sintering process on lithium ionic conductivity of Li6.4Al0.2La3Zr2O12 garnet produced by solid-state synthesis. *RSC Advances*, *8*(24), 13083–13088. https://doi.org/10.1039/c8ra01329b

Yabuuchi, N., Kubota, K., Dahbi, M., & Komaba, S. (2014). *Research Development on Sodium-Ion Batteries*. *114*, 11636–11682. https://doi.org/10.1021/cr500192f

Yanase, I., Kuwada, N., Kuribara, K., Kodama, S., & Takeda, H. (2021). Na-ion conductivity of β-NaFeO2 synthesized from an EDTA chelate complex. *Inorganic Chemistry Communications*, *134*, 108913. https://doi.org/10.1016/J.INOCHE.2021.108913

Yanase, I., Ohtaki, T., & Watanabe, M. (2002). Application of combinatorial process to LiCo1−XMnXO2 (0≦X≦0.2) powder synthesis. *Solid State Ionics*, *151*(1–4), 189–196. https://doi.org/10.1016/S0167-2738(02)00709-9

Yang, C., Xin, S., Mai, L., & You, Y. (2021). Materials Design for High-Safety Sodium-Ion Battery. *Advanced Energy Materials*, *11*(2), 2000974. https://doi.org/10.1002/AENM.202000974

Yoshino, A. (2006). Development of Lithium Ion Battery. *Http://Dx.Doi.Org/10.1080/10587250008025504*, *340*, 425–429. https://doi.org/10.1080/10587250008025504

Yu, H., Han, J. S., Hwang, G. C., Cho, J. S., Kang, D. W., & Kim, J. K. (2021). Optimization of high potential cathode materials and lithium conducting hybrid solid electrolyte for high-voltage all-solid-state batteries. *Electrochimica Acta*, *365*, 137349. https://doi.org/10.1016/J.ELECTACTA.2020.137349

Yu, K., Tian, Y., Gu, R., Jin, L., Ma, R., Sun, H., Xu, Y., Xu, Z., & Wei, X. (2018). Ionic conduction, colossal permittivity and dielectric relaxation behavior of solid electrolyte Li3xLa2/3-xTiO3 ceramics. *Journal of the European Ceramic Society*, *38*(13), 4483–4487. https://doi.org/10.1016/j.jeurceramsoc.2018.05.023

Yu, S., & Siegel, D. J. (2017). Grain Boundary Contributions to Li-Ion Transport in the

Solid Electrolyte Li7La3Zr2O12 (LLZO). *Chemistry of Materials*, *29*(22), 9639–9647. https://doi.org/10.1021/acs.chemmater.7b02805

Yu, Z., Shang, S. L., Gao, Y., Wang, D., Li, X., Liu, Z. K., & Wang, D. (2018). A quaternary sodium superionic conductor - Na10.8Sn1.9PS11.8. *Nano Energy*, *47*(December 2017), 325–330. https://doi.org/10.1016/j.nanoen.2018.01.046

Yuan, P., Tan, D., & Annabi-Bergaya, F. (2015). Properties and applications of halloysite nanotubes: Recent research advances and future prospects. *Applied Clay Science*, *112–113*, 75–93. https://doi.org/10.1016/j.clay.2015.05.001

Yuan, W.-X., & Li, Z. J. (2012). Effects of PVA organic binder on electric properties of CaCu3Ti4O12 ceramics. *Journal of Physics and Chemistry of Solids*, *73*(4), 599–603. https://doi.org/10.1016/J.JPCS.2011.12.024

Yuan, Y., Zhan, C., He, K., Chen, H., Yao, W., Sharifi-Asl, S., Song, B., Yang, Z., Nie, A., Luo, X., Wang, H., Wood, S. M., Amine, K., Islam, M. S., Lu, J., & Shahbazian-Yassar, R. (2016). The influence of large cations on the electrochemical properties of tunnel-structured metal oxides. *Nature Communications*, *7*(1), 13374. https://doi.org/10.1038/ncomms13374

Yung-Fang Yu Yao, & Kummer, J. T. (1967). Ion exchange properties of and rates of ionic diffusion in beta-alumina. *Journal of Inorganic and Nuclear Chemistry*, *29*(9). https://doi.org/10.1016/0022-1902(67)80301-4

Zhang, B., Tan, R., Yang, L., Zheng, J., Zhang, K., Mo, S., Lin, Z., & Pan, F. (2018). Mechanisms and properties of ion-transport in inorganic solid electrolytes. *Energy Storage Materials*, *10*, 139–159. https://doi.org/10.1016/J.ENSM.2017.08.015

Zhang, B., Yang, L., Wang, L. W., & Pan, F. (2019). Cooperative transport enabling fast Li-ion diffusion in Thio-LISICON Li10SiP2S12 solid electrolyte. In *Nano Energy* (Vol. 62, pp. 844–852). Elsevier Ltd. https://doi.org/10.1016/j.nanoen.2019.05.085

Zhang, L., Zhang, D., Yang, K., Yan, X., Wang, L., Mi, J., Xu, B., Li Zhang, Y. L., Zhang, D., Yang, K., Wang, L., Xu, B., Li, Y., Yan, X., & Mi, J. (2016). Vacancy-Contained Tetragonal Na3SbS4 Superionic Conductor. *Advanced Science*, *3*(10), 1600089. https://doi.org/10.1002/ADVS.201600089

Zhang, Q., Zhou, Q., Lu, Y., Shao, Y., Qi, Y., Qi, X., Zhong, G., Yang, Y., Chen, L., & Hu, Y.-S. (2021). Modification of NASICON Electrolyte and Its Application in Real Na-Ion Cells. *Engineering*. https://doi.org/10.1016/J.ENG.2021.04.028

Zhang, Y., Fu, L., & Yang, H. (2012). Insights into the physicochemical aspects from natural halloysite to silica nanotubes. *Colloids and Surfaces A: Physicochemical and Engineering Aspects*, *414*, 115–119. https://doi.org/10.1016/J.COLSURFA.2012.08.003

Zhang, Y., Tang, A., Yang, H., & Ouyang, J. (2015). Applications and interfaces of halloysite nanocomposites. *Applied Clay Science*. https://doi.org/10.1016/j.clay.2015.06.034

Zhao, C., Liu, L., Qi, X., Lu, Y., Wu, F., Zhao, J., Yu, Y., Hu, Y., & Chen, L. (2018). *Solid-State Sodium Batteries*. *1703012*, 14–16. https://doi.org/10.1002/aenm.201703012

Zhao, J., Wang, L., He, X., Wan, C., & Jiang, C. (2008). Determination of Lithium-Ion Transference Numbers in LiPF 6-PC Solutions Based on Electrochemical Polarization and NMR Measurements. *Journal of The Electrochemical Society*, *155*, 292–296. https://doi.org/10.1149/1.2837832

Zhao, N., Liu, Y., Zhao, X., & Song, H. (2016). Liquid crystal self-assembly of halloysite nanotubes in ionic liquids: A novel soft nanocomposite ionogel electrolyte with high anisotropic ionic conductivity and thermal stability. *Nanoscale*, *8*(3), 1545–1554. https://doi.org/10.1039/c5nr06888f

Zheng, F., Kotobuki, M., Song, S., Lai, M. O., & Lu, L. (2018). Review on solid electrolytes for all-solid-state lithium-ion batteries. *Journal of Power Sources*, *389*(February), 198–213. https://doi.org/10.1016/j.jpowsour.2018.04.022

Zhou, W., Li, Y., Xin, S., & Goodenough, J. B. (2017a). Rechargeable Sodium All-Solid-State Battery. *ACS Central Science*, *3*(1), 52–57. https://doi.org/10.1021/acscentsci.6b00321

Zhou, W., Li, Y., Xin, S., & Goodenough, J. B. (2017b). Rechargeable Sodium All-Solid-State Battery. *ACS Central Science*, *3*(1), 52–57. https://doi.org/10.1021/acscentsci.6b00321

Zhou, X., Wu, L., Yang, J., Tang, J., Xi, L., & Wang, B. (2016). Synthesis of nano-sized silicon from natural halloysite clay and its high performance as anode for lithium-ion batteries. *Journal of Power Sources*, *324*, 33–40. https://doi.org/10.1016/j.jpowsour.2016.05.058

Zhu, M., Wu, J., Wang, Y., Song, M., Long, L., Siyal, S. H., Yang, X., & Sui, G. (2019). Recent advances in gel polymer electrolyte for high-performance lithium batteries. *Journal of Energy Chemistry*, *37*, 126–142. https://doi.org/10.1016/J.JECHEM.2018.12.013

Zhu, Y., & Mo, Y. (2020). Materials Design Principles for Air-Stable Lithium/Sodium Solid Electrolytes. *Angew. Chem. Int. Ed*, *59*, 17472–17476. https://doi.org/10.1002/anie.202007621